Optical Force Measurements In Concentrated Colloidal Suspensions

Laurence Wilson

A thesis submitted in fulfilment of the requirements
for the degree of Doctor of Philosophy
to the
University of Edinburgh
2007

Abstract

This work concerns the construction and testing of an optical tweezers-based force transducer, and its application to a hard-sphere colloidal system. A particle in an optical trap forward-scatters a fraction of the trapping light, which is collected in order to give high-resolution information on the trapped particle's position relative to the trap centre. The system is then calibrated to convert particle displacements to forces. The colloid used in this study is a density- and refractive index-matched suspension of PMMA particles, radius 860 ± 70nm, with volume fractions in the range $\phi = 40 \rightarrow 62\%$. Passive microrheological measurements have yielded information about rearrangements in a tracer's cage of nearest neighbours, as well as highly localised measurements of the high-frequency viscosity, where the presence of the colloidal host causes around a tenfold increase compared to the bare solvent case. Measurements have also demonstrated the effect of sample history on local short-time self-diffusion coefficient, with perturbations caused by translating a particle within the sample taking up to an hour to relax in a $\phi = 58\%$ sample. The high resolution particle tracking offered by this technique has also allowed for the first measurement of structure at a shorter lengthscale than the 'dynamic cage size' observed using other experimental techniques. In addition, active measurements have shown the emergence of a yield stress on the order of 5Pa as the volume fraction approaches the glass transition at $\phi \approx 58\%$.

Declaration

This thesis has been composed by me and has not been submitted in any previous application for a degree. The work reported within was executed by me, unless otherwise stated.

Laurence Wilson
April 2007

Acknowledgements

There are a number of people to whom I owe a great debt of gratitude for their help and support during the preparation of this thesis. Firstly, I would like to thank my supervisors Wilson Poon and Jochen Arlt; without their scientific expertise, patience and enthusiasm, this project would have been impossible.

Special thanks are due to Rut Besseling and Andy Schofield for their help with the provision and preparation of colloidal samples, as well as their willingness to answer all manner of questions related to colloids. I would also like to acknowledge fruitful discussions with Mike Cates, Richard Blythe and Gennady Chuev during the analysis of results. Thanks also to Andrew Garrie and Hugh Vass for their technical assistance, and to Bill van Megen for providing me with the results of his light scattering experiments. The contributions of Lucio Isa and Andrew Harrison in the proofreading of this thesis were also gratefully received.

On a less academic level, I'd like to acknowledge the other members of the condensed matter and applied optics groups, as well as the other Usual Suspects, for making JCMB such an enjoyable place to work. Outside the department, I owe many thanks (and pints) to Adrian, Dave et al. from A.V. for protecting my sanity through excessive volume. Above all, particular thanks are due to Alice, Don and Kata who have an unnerving ability to sense when I need cheering up. More generally, I should thank my family for the moral (and, on occasion, financial) support during the preparation of this work. Finally, many, many thanks to Emma for all her patience and understanding while I have been writing this thesis.

Contents

Abstract **i**

Declaration **iii**

Acknowledgements **v**

Contents **vii**

List of figures **xi**

1 Introduction **1**
1.1 Optical tweezers 1
1.2 Colloids 3
1.3 Optical tweezers in colloids 4
1.4 Thesis Summary 8
1.5 Thesis layout 9

2 Optical Tweezers Theory **11**
2.1 Optical forces 11
2.1.1 Radiation pressure 11
2.1.2 Optical gradient force 12
2.2 Analysis of data 15
2.2.1 Frequency domain analysis - theory 15
2.2.2 Frequency domain analysis - practice 17
2.2.3 Time domain analysis 19

3 Optical Setup and Characterisation **21**
3.1 Optical tweezers basics 22
3.2 Apparatus 23
3.3 Position detection 27
3.3.1 Small displacements (<400nm) 28
3.3.2 Larger displacements (>400nm) 29
3.4 Optical characterisation 30
3.4.1 Verification of force calibration 30
3.4.2 Calibrating lengthscales 34

3.4.3 Aside - power spectra of normalised data 35
3.4.4 Verification of length scale calibration 37
3.5 Calibration summary 41

4 Colloids Background and Methods 43
4.1 Observation tools 43
4.1.1 Light scattering 44
4.1.2 Confocal microscopy 47
4.2 Hard-sphere colloidal systems 48
4.2.1 Nature and properties 48
4.2.2 Phase behaviour and metastability 48
4.3 Rheology 51
4.3.1 Macrorheology 53
4.3.2 Microrheology 55
4.4 Colloidal sample preparation and characterisation 57
4.4.1 Stock sample preparation 57
4.5 Characterisation of stock 59
4.5.1 Light scattering 59
4.5.2 Characterisation of suspension medium 60
4.6 Preparation of individual samples 60
4.6.1 Sample cells 61

5 Static Measurements in Dense Colloidal Suspensions 65
5.1 Power spectrum analysis in dense colloidal samples 66
5.1.1 D_s^s on approach to the glass transition, $\phi = 54 \rightarrow 57\%$ . . 66
5.1.2 D_s^s at and above the glass transition, $\phi = 58\%, 62\%$ 71
5.2 Time-series data 75
5.2.1 Volume fractions below the glass transition 75
5.2.2 Volume fractions above the glass transition 82

6 Dragging measurements - Active Microrheology 85
6.1 Average forces 85
6.1.1 First approximation - effective viscosity 85
6.2 Displacement histograms 91
6.2.1 Dragging experiments in samples with $\phi < \phi_g$ 91
6.2.2 Dragging experiments in samples with $\phi \geq \phi_g$ 97
6.3 Size of Rearrangement events 101
6.3.1 The peak extraction routine 103
6.3.2 Peak size distribution 103
6.3.3 Variation with ϕ and drag speed 105

7 Conclusion and Outlook **107**
7.1 Optical characterisation 107
7.2 Static measurements 108
7.3 Dynamic measurements 108
7.4 Future work 109

A Timeline for experimental work **113**

Bibliography **115**

List of Figures

2.1 An ideal Lorenztian spectrum. 18
2.2 The effects of antialiasing on high-frequency data. 19
2.3 An ideal mean-squared-displacement graph. 20

3.1 The numerical aperture of a lens is obtained from the geometry of the focused beam, and the refractive index of the sample medium. The immersion oil (which lies between the lens and the sample slide) has been omitted for clarity. 22
3.2 Schematics for the two main optical tweezers configurations. In the standard configuration, the particle's weight (denoted $\mathbf{g}$) and the scattering force (denoted $\mathbf{F}_s$, see section 2.1.1) are parallel, whereas they are antiparallel in the inverted layout. 23
3.3 Schematic of the optical tweezers force-measurement system. . . . 24
3.4 Schematic of the effects of NA on trapping strength. 25
3.5 Schematic of the quadrant photodiode (QPD) signal processing. The factor of V^{-1} in the expressions for R_x and R_y is related to the normalisation of the signal, discussed in more detail in section 3.4.3. 27
3.6 Images recorded using a CCD camera attached to a computer with a frame-grabbing card. 31
3.7 Displacements from equilibrium as a function of stage speed, as recorded by the CCD camera. 32
3.8 Optical trap stiffness as a function of laser power, with both data (red crosses) and theoretical prediction (green line). 33
3.9 Sensitivity of the detection system as a function of laser power. x and y sensitivities are plotted on the left-hand vertical axis, and z sensitivities on the right. 35
3.10 One-dimensional mean-squared displacements for particles in a bare solvent, with different laser powers (and hence trap stiffness). The amplitudes of the long-time plateaux *increase* with *decreasing* laser power; the curves are stacked in the same order as the figure key. The thick line in the upper plot represents the mean-squared displacement of a freely diffusing tracer in this solvent, calculated using the solvent viscosity measured in section 4.5.2. 36

3.11 Normalised x-axis power spectra for a selection of the experiments in figure 3.10. Note that the high-frequency portions of the graphs overlap. 37
3.12 QPD response to a known bead displacement. The inset shows the deviation from a straight line fit to the portion of data between -0.35μm and 0.35μm. 38
3.13 Histograms of particle position from Stokes drag measurements. The peaks in the negative and positive halves of the graph are different heights in the case of the slower drag speed because the recording does not cover a whole number of cycles of positive and negative velocity. 40
3.14 Actual displacements against displacements according to QPD. . . 40
3.15 2D histogram of tracer position in bare solvent, at a sampling rate of 2kHz, bin size 2.5nm. The colour bar indicates the number of scans falling in each bin. 42
3.16 Histograms of X- and Y-coordinates. The curved lines are Gaussian fits to the data. 42

4.1 Schematic of the light-scattering process. 45
4.2 Theoretical form factor for a spherical particle. 47
4.3 Hard-sphere system phase diagram. 49
4.4 Schematic of the α and β timescales. 50
4.5 The responses of an ideal liquid and an ideal solid to a step stress and a step strain. 52
4.6 Light scattering results. 60
4.7 Rheological measurements of solvent viscosity as a function of temperature. 61
4.8 Sample holder for high volume fractions. 63
4.9 Sample holder for low volume fractions. 64

5.1 Power spectra for tracer motion in a $\phi = 54\%$ suspension, mean $D_s^s/D_0 = 0.119$, compared to the literature value mean 0.12. . . . 67
5.2 Power spectra for tracer motion in a $\phi = 56\%$ suspension, mean $D_s^s/D_0 = 0.112$, compared to the literature value mean 0.106. . . 67
5.3 Power spectra for tracer motion in a $\phi = 57\%$ suspension, mean $D_s^s/D_0 = 0.081$ compared with the literature value mean 0.09. . . 68
5.4 Power spectra for tracer motion in a $\phi = 40\%$ suspension compared to a power spectrum from a bare solvent measurement. $D_s^s/D_0 =$ 0.290 in the sample with colloidal host, compared to the literature value 0.30. 68

5.5 Comparison of a power spectrum obtained from a 40% suspension with one from a 57% sample. The 40% sample shows a larger amplitude at high frequencies (hence lower viscosity), and flatter low-frequency behaviour. 69

5.6 A reproduction of figure 7 from reference [53]. This graph shows the evolution of particle mean-squared displacements in samples with 13 volume fractions ranging from $\phi = 46.6\% \rightarrow 58.3\%$ from left-most to right-most data. The thick line at the left hand side describes the motion of a freely diffusing particle in bare solvent. The horizontal axis is measured in units of Brownian time (the time taken for a particle to diffuse its own radius in bare solvent) and the vertical axis shows distance (normalised by particle radius) squared. 70

5.7 A summary of the measurements from this section. Red crosses represent light-scattering measurements performed by van Megen et al., and green crosses reflect values obtained by fitting straight lines to the high-frequency data in figures 5.1 - 5.4. 71

5.8 Power spectra for tracer motion in a $\phi = 58\%$ suspension, mean $D_s^s/D_0 = 0.0952$ for runs 1 and 5, compared with the literature value mean 0.094. 73

5.9 Power spectra for tracer motion in a $\phi = 62\%$ suspension, mean $D_s^s/D_0 = 0.0597$ from an average of the values obtained in runs 4-7, compared with 0.026 extrapolated from literature values. . . . 73

5.10 Comparison of D_s^s/D_0 measured by this optical tweezers study with previous light scattering studies. The red crosses are light scattering data from reference [117], the green crosses are power spectrum measurements from samples with volume fractions below the glass transition, and blue stars are data from above the glass transition. The order in which the measurements were made in the glassy samples has been labelled; the cage relaxation time in the $\phi = 58\%$ sample has been found to lie somewhere between 15 and 60 minutes. Relaxation times in the $\phi = 62\%$ sample are much longer, although measurements here have put a lower bound of 1 hour on the relaxation time. 74

5.11 Position-time displays of a static measurement in a $\phi = 57\%$ suspension. The axis at the right-hand side shows the optical potential as a function of position. The data from which the short-time histograms in figure 5.12 were drawn are indicated. 76

5.12 1D histograms showing particle x-position at three different times during the course of a static-trap experiment in a $\phi = 57\%$ suspension. Histograms were made of subsections of the total data, as indicated in the key, to illustrate the short-time behaviour of the probe. The raw data corresponding to all these histograms is presented in the time series figure 5.11. The trap stiffness was $\kappa = 4.11 \times 10^{-3}$pN/nm. 77
5.13 A schematic diagram showing a cage of particles (numbered 1-6) rearranging from state (a) to state (b). When the particles numbered 4 and 5 relax into positions lower down the diagram, the rest of the cage relaxes, shifting the position of the tracer relative to the optical trap (denoted by the red circle). The size of the rearrangement is exaggerated here; the actual probe displacements observed are about 15% of that pictured. 77
5.14 Position-time series for a probe particle in a $\phi = 57\%$ sample, note the temporary jump at around 500-600 seconds. The right-hand axis shows the optical potential energy ($U = \frac{1}{2}\kappa x^2$) due to the trap - the trap stiffness is $\kappa = 2.89 \times 10^{-3}$. 78
5.15 (*Left*) A 2D histogram the measurement in figure 5.14 (tracer position in a $\phi = 57\%$ suspension), resampled at 2.5Hz; again, the colour bar indicates the number of scans falling into each bin. The total length of the measurement was 15 minutes. 79
5.16 (*Right*) A subsection of the run in upper figure from 500-600 seconds, showing short-time behaviour in a cage structure. 79
5.17 2D histogram of tracer position over 800 seconds in a $\phi = 57\%$ suspension. The bin size here is 2.8nm, and the colour bar indicates frequency. 80
5.18 These graphs are subsections of the measurement in figure 5.17. Figures (a)-(d) are successive 200 second portions (with timeframes as labelled) showing relatively stable average position over their duration. 81
5.19 Time series of the data in figure 5.20. The data has been resampled from the original rate of 10kHz down to 3.3Hz. 83
5.20 2D histogram of displacements in a $\phi = 62\%$ glassy sample. At the average particle position, the potential energy due to the optical trap is $\sim 32 k_B T$. 83
5.21 A time series of a measurement in a $\phi = 62\%$ sample, where a cage rearrangement occurs at around 1000 seconds. The horizontal black lines show the range of data used to make the histograms in figures 5.22 and 5.23, and the mean values for these ranges. The cage rearrangement accompanies a decrease in optical potential from $14.8 k_B T$ to $13.2 k_B T$. 84

5.22 2D histogram of data from the first 1000 seconds of the recording in figure 5.21. 84
5.23 2D histogram of data from 1200 seconds to the end of figure 5.21. 84

6.1 Force-time series for dragging experiments in two different volume fractions, $\phi = 54$ and 58%, at a speed of 0.4μm/s. The slight negative detour at around 34 seconds in the lower volume fraction measurement is due to mechanical backlash in the stage motor; this region is excluded from the analysis of results. 86
6.2 Average force as a function of stage speed and volume fraction. At volume fractions below the glass transition ($\phi \approx 58\%$), the suspension appears fluid, with force measured tending to zero at zero stage speed. Least-squares fits are included for volume fractions below the glass transition, and the dotted horizontal line is a guide to the eye, illustrating the qualitative change in behaviour in the glassy sample. The $\phi = 0\%$ is a schematic showing the forces on a tracer in bare solvent, based on the viscosity measured previously. 87
6.3 A comparison of active rheology data with that obtained from light scattering measurements. The effective diffusion coefficients from dragging experiments are significantly smaller than those obtained from passive techniques. 89
6.4 Effective radius - the distance within which host particles will directly collide with the probe. The green particles' centres are within one particle radius of the probe centre's path; the red particles' centres lie just outside this, but within the effective radius. The light grey particles' centres lie outside the effective radius. 90
6.5 Drag histograms in $\phi = 54\%$. 91
6.6 Distribution of forces in a $\phi = 56\%$ colloidal suspension during dragging experiments. 93
6.7 Distribution of forces in a $\phi = 57\%$ colloidal suspension during dragging experiments. 94
6.8 Standard Deviation of the histograms in figures 6.5 to 6.7. The standard deviation in drag measurements is always greater than that in the static case, and generally increases with faster drag speeds; in the highest volume fraction, this is not as apparent, although the mean of the histograms (see figure 6.2) does show a general increase. 95
6.9 Third moment (skewness) of the histograms in figures 6.5 to 6.7. The overall trend is a decrease in skewness with increasing drag speed. 96

6.10 Force histograms for a $\phi = 58\%$ suspension. The average displacement is essentially constant, and only increases at the highest velocities. 97
6.11 At a volume fraction of $\phi = 62\%$, the shape of the force distribution function is irregular, with a high mean value and large standard deviation. The trapping laser was turned up to its maximum value to perform these measurements, as the yield stress is large (around 1.2 Pa). 99
6.12 Time-force series for a dragging measurement in a $\phi = 62\%$ colloidal glass. The data have been down-sampled to 2Hz. 100
6.13 Position-time series for the lowest and highest volume fractions, at the same drag speed. The crosses mark out the corners of the histogram bar for the higher volume fraction. One histogram bin is equivalent to half a particle radius; although the average speed in both is the same, the scatter of data points is much larger in the case of the glassy sample. This is because the particle motion in the non-ergodic sample is impeded by successive, relatively stiff particle cages, which allow only erratic progress through the sample. 100
6.14 Time-force series for a dragging measurement at 0.2μm/s in a $\phi =$ 62% colloidal glass. The data have been down-sampled to 2Hz. . . 102
6.15 A two second subsection of the measurement in figure 6.14. The data have been down-sampled to 200Hz, so there is the same number of data points in both the longer and shorter graphs. . . . 102
6.16 Example of peak detection routine, on a section of a measurement in $\phi = 58\%$, drag speed 0.4μm/s. The red line represents the original data, while the points are the peaks detected using different time windows. The peaks have been translated vertically for the sake of clarity. 104
6.17 Size distribution of rearrangement events in a $\phi = 56\%$ colloidal suspension. The thick black lines show the highest and lowest values of Υ (1.56 and 2.14 respectively). 105
6.18 Variation of Υ with drag speed. 106

Chapter 1

Introduction

1.1 Optical tweezers

Optical tweezers, first realised by Arthur Ashkin in the mid eighties [1] are most concisely described as a tool which uses the momentum of photons to manipulate objects. They have allowed researchers to gain an unprecedented level of control over their subjects; in the past, scientists have been passive observers of microscopic events, or have only been able to influence samples intrusively (for example, with micropipettes) or in the bulk (by washing an entire sample with a chemical). Optical tweezers allow delicate and precise positioning of microscopic bodies, such as fungal spores [2], so their interactions may be studied.

The simplest way to visualise the physical mechanism of optical tweezers is to consider refraction. This phenomenon is well-known; light appears to 'bend' on passing from one medium into another with a dissimilar refractive index. The incident beam of photons arrives with a certain momentum, which is changed upon interaction with a medium - by Newton's second law this constitutes a force acting on the photons. Elementary mechanics also dictates that if a force is acting on the beam of photons, an equal and opposite force must be felt by the body responsible for the refraction. Whilst the physical magnitude of a change in momentum of a photon is small when considered on a macroscopic scale, microscopic dielectric bodies have masses low enough to be measurably perturbed, and even picked up by only a few milliwatts of laser radiation.

The actual design of an optical tweezers system has remained largely the same since its inception around twenty years ago[1]. A collimated laser beam directed into the back of a microscope objective lens forms a tightly focused spot in the lens' front focal plane. This focal spot attracts dielectric particles nearby to its centre, where they are confined, but still buffeted by Brownian forces - a phenomenon upon which the work in this thesis relies. Since the first realisation of a single beam trap, various modifications have been suggested to increase the flexibility of the apparatus. Some of the major improvements include the use of galvanometer-mounted mirrors [3] to scan the laser across several locations in the focal plane, allowing the creation of multiple traps or extended line traps. The use of holographic systems [4, 5, 6] has allowed an extension of this concept, in order to create user defined 'optical potential landscapes' in almost any configuration.

---

[1] Although examples of optical trapping (in a more general sense) were present before this date, reference [1] is widely considered seminal for optical tweezers.

Making microscopic measurements of force is something that is of great interest to researchers in many fields, from condensed matter physics [7, 8] to fungal biology [9] and haematology (the study of blood) [10]. As an inherently microscopic technique, optical tweezers are well suited to such a task. One of the first papers to measure force and torque quantitatively using optical tweezers examined bacteria 'tethered' to a surface [11], where torques of the order of 1×10^{-15}Nm were measured. Most optical tweezers-based force measurements are fundamentally linked to measurements of position; in a typical experiment, one calibrates force measurements by applying a known force to a probe particle, and measuring the response. This information may be used in later experiments, where a probe's displacement is measured and converted back to force. The force calibration therefore has a critical dependence on the accuracy and resolution of the position detection system.

In the late 1990s, the use of back focal plane interferometry to measure position [12, 13] proved a major advance in optical tweezers-based force measurement. Interferometric techniques are not subject to the diffraction limit, and offer up to a hundred-fold increase in precision compared to standard video techniques; systems based on this method have been used fairly recently to make measurements of position down to Ångström level [14]. Position measurements with a high enough resolution can also simplify the force calibration procedure, by appealing to thermodynamic principles [15, 16]. This type of procedure (described in detail in chapters 2 and 3) and techniques developed from it make up the bulk of this thesis.

1.2 Colloids

The term 'colloidal system' covers a wide range of substances, from airborne smokes and mists to stained glass. These all come under the definition of a colloid: "*a dispersion of finely divided particles in a chemically distinct dispersion medium*". The typical size of the finely divided particles is between ten nanometres and ten micrometres (10^{-8}-10^{-5}m), which is small enough to be affected by Brownian motion, but too large for quantum mechanics. Colloidal suspensions have been studied by scientists for more than one hundred years, stretching back at least as far as Faraday, who studied colloidal gold particles in the 1850s [17]. The modern view of colloidal physics really takes shape with the work of Perrin in the early 20th century; his efforts won him the 1926 Nobel prize for physics, "for his work on the discontinuous structure of matter, and especially for his discovery of sedimentation equilibrium". At that time, the existence of atoms as more than a conceptual device was in doubt; Perrin provided strong evidence for their physical reality in a set of experiments on spherical colloidal particles [18]. When observed through a microscope, the spherical particles moved randomly due to thermal motions in their solvent suspension medium, and from this Perrin was able to show that the particles obey the equipartition of energy. He also showed that if left to settle under gravity, the concentration of particles in a dilute suspension drops off exponentially with height. This last phenomenon hints at the reason why scientists today are interested in colloidal systems — the behaviour of Perrin's dilute suspension was the same as that of gas molecules under gravity in our atmosphere [19].

Colloidal systems exist in which transitions analogous to the more familiar phase transitions such as freezing and boiling may be observed directly by microscopy. The usefulness of colloidal systems as an analogy for atomic and molecular thermodynamic systems becomes clear when the timescales of phase changes are taken into account; colloidal systems typically relax from an unstable state to their equilibrium phase states on timescales of seconds, minutes and hours. Systems made of real atoms and molecules typically change phase over much smaller intervals, of order 10^{-9}s or shorter. The slow dynamics of colloidal systems has allowed the systematic study of curious metastable physical states such as glasses, which have a structure like a liquid, but mechanical properties like a solid. It is also possible to 'tune' inter-particle forces, for example, by the addition of polymers or charged molecules to the solvent medium. These forces are central in determining the behaviour of suspensions, and experiments with varied inter-particle attraction have already led to the discovery of new phase transitions [20].

As well as fundamental research, colloid science is of great interest to industry. Many commercial products are colloidal in nature, from foodstuffs like mayonnaise and milk to beauty products and petrochemicals. The production of such materials could be simplified, and their shelf-life extended, if we had a better understanding of the microscopic processes that govern their behaviour. Colloidal systems are interesting not only due to their ubiquity, but also for their mechanical properties — 'rheology' is the study of their deformation and flow under an external force. Dense cornflour-water mixtures are an example of a relatively commonplace colloidal substance that exhibits peculiar rheological behaviour. When stirred slowly, the material acts like a liquid and the 'wake' of the stirring device closes up quickly as adjacent material flows into the void behind it. When stirred faster, the material suddenly takes on the appearance of a solid, and will fracture and form crumbs, returning to its fluid state some time later; this is just one particular example of the counter-intuitive behaviour of colloidal substances.

1.3 Optical tweezers in colloids

Optical tweezers are ideally suited to the study of colloidal systems. The samples used in the first papers on optical tweezers – suspensions of micrometre-sized dielectric particles [1] and bacteria [21] (which can be considered a 'living' colloid) – were chosen because their size made them ideal subjects. The techniques used to study colloids vary in sophistication from the simplest versions, where tweezers are used to position particles prior to an experiment, through to complicated force measurement systems, such as the one documented in this thesis. Some of the more prominent experimental work in this field over the last fifteen years is reviewed below.

Manipulation of particles

One of the most straightforward uses for optical tweezers is as a positioning aid in microscopy. Crocker et al. [22] examined the interaction energy of two isolated, charged colloidal particles in a bath of electrolyte; this interaction is of profound significance to colloid physics as it is central to predicting the phase behaviour of large numbers of such particles. Two particles were positioned using tweezers and then the trapping laser beam was switched off. The subsequent motion of the particles is observed, and by this method Crocker et al. were able to show that the interaction between the particles is in accordance with the long established DLVO theory[2]. Extensions to this work in confined geometries yielded other interesting results; experiments on pairs of particles, 0.5μm radius, held between two charged glass surfaces (the separation of which is around 5μm) showed a long-range attraction that is not predicted by the DLVO theory [24]. Other geometrical effects are examined in reference [25], where the hydrodynamic coupling between particles and the sample cell wall is examined — special effort is made here to eliminate the effects of charge, by the addition of HCl to the solvent medium. An increase in solvent viscosity is observed close to the wall (there is a decrease in the rate at which particles diffuse), and this was found to be in agreement with theoretical predictions [26]. Faucheux et al. [27] have demonstrated directed colloidal diffusion using an optical trap scanned in a ring. A neutral density filter wheel was used to vary the laser intensity around the ring's circumference, producing an asymmetric, periodic sawtooth pattern. The movement observed shows that this is an example of a 'Brownian ratchet' whereby a modulated potential is used to extract directed motion from random noise. Further investigations into diffusion have sought to elucidate the details of how microscopic mechanical processes (molecular collisions which are time-reversible) translate to irreversible macroscopic thermodynamic effects, testing the 'transient fluctuation theorem' of Searle and Evans [28].

Other experiments on colloidal systems include the investigations of Dinsmore et al. [29], who examined the entropic forces in a colloid made up of particles of two different radii, 42nm and 230nm, in different environments. The small particles' entropy is maximised when the volume per particle is maximised; this results in the larger particles diffusing preferentially into corners and more restricted spaces. Optical tweezers were used to position the larger particles at the start of the experiments before being switched off so the freely diffusive motion could be observed. As well as positioning particles and then releasing them, other researchers have used tweezers to transport particles to particular locations where they are immobilised, serving as templates for colloidal crystal growth [30].

---

[2] The DLVO potential – DLVO is an acronym for "Derjaguin-Landau-Verwey-Overbeek" – describes the interaction energy of two charged particles, each surrounded by a cloud of ions with the opposite charge to their own. See reference [23] for a review of interparticle interactions and phase behaviour in colloids.

Typically, colloidal particles for use with optical tweezers will be transparent and have a refractive index higher than that of the suspensions medium; if they do not, then stable trapping is impossible in a static Gaussian beam. By using either a scanning laser beam [31, 32], or ring-shaped traps created by Laguerre-Gaussian mode patterns [33], metal particles and particles with a lower refractive index than the solvent have been trapped. This use of more exotic trap shapes with non-Gaussian intensity distributions also provides other advantages; as well as forming 'hollow' or ring-shaped traps, Laguerre-Gaussian beams have been shown to have orbital angular momentum [34] which can be used to provide a constant rotation speed for small arrays of particles [35]. Bessel beams [36] have also been used to hold arrays of colloidal particles, even in two different sample cells simultaneously (the cells were separated by a distance of around 100μm). This was possible due to the Bessel beam's curious property of 'self-reconstruction' whereby the perturbations to the optical field caused by trapped particles are highly localised along the propagation direction.

The creation of non-Gaussian intensity patterns in the visual field of a microscope has been facilitated by the use of diffractive optics placed in a plane conjugate to the back focal plane of the objective lens. Either static patterns [4] or computer-addressed spatial light modulators [37] may be used to generate the trap arrays in the objective's front focal plane. This kind of diffractively produced array is capable of sorting colloidal particles in a liquid flow [38], by providing an 'optical potential landscape' with a filtering effect that depends on the size of the particles.

Microrheology with Optical Tweezers

Microrheology is an extension of conventional rheology to the level of individual particles. Optical tweezers are an ideal tool for the investigation of the microrheology of hard-sphere colloids, as existing experimental techniques developed for rheological measurements in other complex fluids such as polymer or biopolymer solutions [39, 40, 41], viral suspensions [42] and worm-like micelles [43, 44] may be used — see reference [45] for an overview. Studies usually take the form of either passive or active measurements. In the passive measurement case, the optical trap is used to hold a particle still and measure fluctuations in its position, and how they are affected by the surrounding medium. If the diffusive motion of a single particle in the absence of host colloid (the 'bare solvent' case) is known, the effect of the host colloid can be obtained. In the case of active measurements the optical trap is weakened, or moved relative to the surrounding suspension, and the forces that the trapped particle experiences are measured.

Passive studies in this field includes the studies by Meiners et al. [46] and by Henderson et al. [7, 47] where the interactions between two neighbouring colloidal particles in a very dilute suspension are measured with high precision, using the same quadrant photodiode method for particle tracking that is used in this thesis. The first authors found that although the suspension medium is typically taken to show no long-time 'memory' effects in a colloid, the particles are in fact hydrodynamically coupled; the second group of authors went on to show that this interaction propagates at the speed of sound in the solvent. Greinert et al. [48] studied the behaviour of a passive tracer particle (radius 550nm) in a suspension of laponite clay, which is composed of disc-like particles 15nm in radius, in water. The authors define an effective temperature for the tracer particle, and monitor how it changes with time after the sample preparation, measuring a marked increase as the sample becomes glassy. Experiments on a similar system were conducted by Mizuno et al. [49], where the researchers observe the mechanical response function of an ageing colloid, finding good agreement with the fluctuation-dissipation theorem, apparently contradicting the previous study.

Active measurements have also been performed on colloids. For example, Yada et al. [50] investigated the interparticle forces between two colloidal particles in a suspension of nematic liquid crystals, and how it is affected by defects in the local structure. Smalyukh et al. [51] also conducted experiments on liquid crystals, looking at the tension in line defects within a liquid crystal matrix. The study that is most similar to this thesis is the one by Meyer et al., [8] where a large probe particle is dragged through a dilute host. Samples of refractive-index-matched, irregularly shaped fluorinated ethylene propylene (FEP) particles, as well as fluorescently tagged poly-methyl methacrylate (PMMA) spheres were used. It was found that the viscosity of the suspensions increased with volume fraction in the case of the FEP, as predicted theoretically. Analysis of the fluorescence images acquired during dragging in the PMMA suspension show the formation of a dense boundary layer of particles ahead of the probe, as well as a distinctive 'wake' forming behind the dragged particle.

1.4 Thesis Summary

In preparation for the experiments documented in this thesis, I have constructed (in collaboration with postdoctoral researcher Dr. Jochen Arlt — a description of the division of labour is presented in the appendix) an optical tweezers system capable of highly accurate position and force measurement from open-bench optical components, in contrast to most other optical tweezers systems that are constructed around a commercially available microscope. Our type of system has two main advantages; firstly that all conjugate focal planes are immediately accessible, which helped with equipment positioning and beam alignment, and secondly that we were able to choose specialised components to construct the system, with a view to reducing experimental noise due to mechanical vibrations.

Colloidal samples of PMMA were prepared and characterised, with particular attention paid to the density and refractive index matching of the suspension. The radius of the particles was measured using static light scattering, which also determined the sample polydispersity (the standard deviation of particle size divided by the mean); an upper bound on this quantity had already been established by observing that the samples crystallize. Sample cells were developed and optimised for optical tweezers studies, with particular care taken when dealing with high volume fractions, where self-filtration phenomena have been documented [52].

Volume fractions above and below the glass transition were studied with both passive and active techniques. The high position resolution and recording bandwidth of this method have allowed measurements of the short-time self-diffusion coefficient within a single cage, as well as providing a first sight of structure within the ‘dynamic cage’ observed by photon correlation spectroscopy (dynamic light scattering) and confocal microscopy. The large-displacement calibration has allowed the first non-linear microrheological measurements in a hard-sphere glass, as well as the observation of a qualitative change from liquid-like behaviour to that of a solid on approach to the glass transition. Finally, an advanced peak-detection routine based on wavelet techniques has shown that particle rearrangement events during drag measurements have no characteristic time scale. The size distribution of stress relaxation events is governed by a critical exponent, which varies as a function of drag speed. For drag speeds below 1μm/s, the same general trend is apparent at all volume fractions: faster drag speeds lead to more small relaxations, whereas slow drags have an event distribution more biased towards large events.

1.5 Thesis layout

This thesis is composed of two parts: the theory, construction and characterisation of a force-calibrated optical tweezers system in chapters 2 and 3; and the preparation of, and experiments on, a hard-sphere colloidal system in chapters 4 - 6.

Chapter 2 contains the theoretical background to the optical tweezers technique, including a model of the optical trapping mechanism based on electromagnetic theory. This chapter also introduces some of the mathematical techniques used in the data analysis; their subtleties are explored in greater detail in later chapters. Chapter 3 describes the main design principles behind optical tweezers, and a description of the apparatus. Details of the careful calibration procedure, as well as the cross-checks between calibration methods can also be found here. Chapter 4 contains a brief background to the colloidal experiments, including an introduction to rheology and other experimental techniques. Sample characterisation data is also in this chapter, as are light-scattering measurements to determine the particle core size, and bulk rheology measurements of the solvent viscosity. Finally, this chapter gives details of sample cell construction and loading procedures.

Chapters 5 and 6, give the main experimental results. Comparison is made with other experiments in the literature, with particular reference to the light scattering measurements of van Megen et al. [53], and the bulk rheological measurements on colloidal systems by Petekidis et al. [54]. Finally, chapter 7 summarizes the information obtained, along with suggestions for future experiments based on this study.

Chapter 2

Optical Tweezers Theory

The theoretical basis for this study of optical tweezers is broken down here into two sections. Firstly, a description of the trapping force is presented, based on an electromagnetic approach adopted in reference [55], including a method for quantitative predictions of trap stiffness. Secondly, specific methods of data analysis are presented, particularly power spectrum techniques, and their use for extracting trap stiffness and the diffusion coefficient for a trapped particle.

2.1 Optical forces

There are two competing processes central to optical trapping, both are functions of electric field strength: radiation pressure (which is a function of $\mathbf{E}^2$) and the optical gradient force (a function of $\nabla\mathbf{E}^2$).

2.1.1 Radiation pressure

Optical trapping, like many other scientific phenomena, was first discovered by accident. In the nineteen-seventies, Steven Chu and co-workers noticed that stray dust inside a laser tube was being confined within a laser beam, as opposed to diffusing in and out in a more random fashion [56]; this was later the subject of an experiment by Ashkin [57] at the same laboratories. Once in a laser beam, the dust was propelled in the direction of laser propagation by radiation pressure (explained in this section). This propulsive effect was initially used to support the weight of small droplets of water in an upward-pointing laser beam [58], in the guise of 'optical levitation'.

Although radiation pressure effects are small in magnitude, they are responsible for some macroscopic phenomena. An example would be the tails seen following comets, due to the icy nucleus moving under gravity against a solar 'headwind' of photons. Radiation pressure can be approximately quantified using a basic photon momentum picture. If a photon has momentum $\mathbf{p} = \hbar\mathbf{k}$, upon being reflected through 180° from an object it exerts a force $\mathbf{F}$ on the object

$$\mathbf{F} = \frac{\Delta\mathbf{p}_{total}}{\Delta t} = \frac{2\mathbf{p}}{\Delta t} \tag{2.1}$$

The force exerted by one photon is exceedingly small, of order 10^{-27}N, but the force exerted by many photons in a laser beam can become significant under some circumstances. For a beam with a total power P, resulting from a flux of N_p photons per unit time, a simple calculation of the force due to radiation pressure would be:

$$P = \frac{N_p c\hbar k}{\Delta t}$$

$$F = 2N_p \frac{p}{\Delta t}$$

$$F = 2\frac{P}{c} \tag{2.2}$$

For example, the force exerted by a laser beam of power 50mW is 300pN; this force is very significant at microscopic length scales. To put it into perspective, common protein-protein interactions occur with forces on the order of 20pN, and unwinding a strand of DNA requires about 50pN [35].

2.1.2 Optical gradient force

The first experimental realisation of the optical gradient force in the manner of optical tweezers was again by Ashkin, in the mid eighties [1], following on from experiments into the confinement of particles in collimated laser beams. When examining exactly how the gradient force in optical tweezers works, it is important to recognise the length scales being considered. Other authors have analysed optical trapping both in the $\lambda \ll r$ (ray optics regime) [59], or $\lambda \gg r$ (Rayleigh regime, implying a dipole approximation for the trapped particle), where r is the approximate scale of the subject [12]. Both of these approximations have only limited validity in this study, where $\lambda \approx r$. The tight focusing of the laser beam, effectively down to the diffraction limit, means that the scalar diffraction approximations of the Rayleigh and ray optics descriptions are insufficient for a rigorous analysis of the process. The authors in reference [60] have reported that even higher order corrections to either Rayleigh or ray optics theories are insufficient to accurately predict the trapping force on spheres with radii in the range $0.5 \leq r \leq 5\mu$m.

In the general case, to compute the forces acting on a dielectric due to electromagnetic radiation, it is necessary to integrate the Maxwell stress tensor across the surface of the dielectric [61];

$$F_i = \oint \sigma_{ik} dS_k \tag{2.3}$$

Where the stress tensor σ_{ik} has elements that are functions of the electric and magnetic field strengths at the dielectric's surface:

$$\sigma_{ik} = \frac{1}{4\pi}[\varepsilon E_i E_k + B_i B_k - \frac{1}{2}(\varepsilon E_i E_i + B_i B_i)] \tag{2.4}$$

A full mathematical treatment of the interaction of a dielectric sphere with an ideal focused Gaussian laser beam is presented in reference [62], where reasonable qualitative agreement with experiment is found. The discrepancies found are attributed to spherical aberrations in the experimental system, whose inclusion in the mathematics complicates the problem significantly.

A version of the argument using two key simplifying assumptions, as suggested in reference [55], has proved useful in providing accurate quantitative predictions of the force on a dielectric due to a focused laser beam. One assumes firstly that the electric field terms in the stress tensor dominate, and secondly that the main contribution to the interaction between laser and particle arises from the gradient in electric field strength squared. This approach neglects interference effects, and the force can be deduced from the change in dipole interaction energy as a function of particle position. The dipole interaction energy of a dielectric with polarisation $\mathbf{P}$ in an external field $\mathbf{E}_0$ is given by [63]:

$$U(r) = -\frac{1}{2}\int_V \mathbf{E}_0 \cdot \mathbf{P}\; dV \tag{2.5}$$

Where the polarisation, given by

$$\mathbf{P} = \varepsilon_0 \chi \mathbf{E} \tag{2.6}$$

becomes

$$\mathbf{P} = \varepsilon_0 \chi \mathbf{E}_0 \tag{2.7}$$

if the dielectric susceptibility $\chi = \frac{\varepsilon_r - 1}{4\pi}$ is assumed to be much less than one. This allows a simplification of equation 2.5 to

$$U(r) = -\frac{\chi}{2} \int_V \varepsilon_0 E_0^2 dV \tag{2.8}$$

$$U(r) = -\alpha \int_V I dV \tag{2.9}$$

Giving an expression for $U(r)$ in terms of the energy density of the focused beam $I = \frac{\varepsilon_0 E_0^2}{8\pi}$ integrated over the volume of the particle inside the beam. The term α represents the difference in permittivity between particle and the surrounding medium, $\alpha = \frac{\varepsilon_p}{\varepsilon_0} - 1$. Both the particles in this study and the suspension medium have a permeability close to 1, so the approximation $n \approx \sqrt{\varepsilon}$ for refractive index is a good one. This term therefore shows that the trapping force is directly proportional to the square of the difference in refractive index between a particle and its environment; the force approaches zero for particles close to the index-matched limit.

In order to compare results with theory directly, the approach of reference [64] to the work in reference [55] has been adopted. In order to simplify the integration, the particle in the optical trap is approximated as a cube, and the stiffness of the optical trap is found to be

$$\kappa/P = k_R a_c \operatorname{erf}\left(\frac{a_c}{\sqrt{2}}\right) \operatorname{erf}\left(\frac{a_c}{\epsilon\sqrt{2}}\right) e^{-(1/2)a_c^2}, \tag{2.10}$$

where κ is the trap stiffness, P the laser power, a_c the position coordinate within the beam, normalised by the beam waist size, and the eccentricity ϵ (the ratio of length to width of the putative ‘trapping volume’, where the optical potential well is deeper than $\sim 3k_BT$). The constant $k_R = 4(n_p - n_m)\epsilon/c\omega_0$ is used to verify that the equation yields correct values for stiffness in the limit of small particle size (the Rayleigh regime where $a \ll \lambda$). A comparison of theory with experiment is presented in the optical setup chapter.

2.2 Analysis of data

The data acquired is analysed using two different viewpoints: Frequency domain and time-domain. The two methods for analysis are equivalent, but highlight different aspects of colloidal behaviour. The initial work was performed using a frequency-domain analysis which allows easy comparison with existing light-scattering data (see chapters 4), where a comparison of high-frequency viscosity has been particularly fruitful.

The time-series analysis is perhaps more intuitive, and is used to illustrate concepts such as different caging lengths in dense suspensions, and other dynamic effects. The time series analysis adopts much of the language developed in dynamic light-scattering (DLS) studies [17, 65], although the data obtained here is intrinsically noisier as this technique does not share the many-particle averaging of DLS. The arguments below are developed for the case of a probe particle in a Newtonian fluid, that is, it is assumed that the optically trapped particle is suspended in a fluid whose viscosity is a constant at all frequencies. This holds true for experiments performed on a particle in a bare solvent where perturbations in the arrangement of liquid molecules relax on a timescale far shorter than our experimental timescale. Deviations from this ideal behaviour demonstrated by a particle suspended in a colloid will shed some light on the properties of such systems.

2.2.1 Frequency domain analysis - theory

The motion of a trapped particle in one dimension may be modelled as a damped, driven harmonic oscillator, that is to say that the restoring force is a linear function of displacement[1]. As motion in the other two spatial dimensions is expected to be uncorrelated, a similar description (most likely with slightly different parameters) may be provided for these axes. One caveat to this statement is that the shape of the optical potential in the z-axis is not symmetrical about the origin; as well as the effect of radiation pressure along the optical axis, the presence of the particle in the optical trap perturbs the light distribution further downstream. This effect is most significant at larger probe displacements, where the deviation of the scattered field from the unscattered field is greatest. Nevertheless, a high degree of success has been achieved by modelling the motion of a probe particle of radius a in a viscous solvent using a Langevin equation with a harmonic potential [66]. The particle motion is driven by random, uncorrelated Brownian forces $F(t)$ which have an average value of zero, and a power spectrum which is constant for all values of f (i.e. a true 'white' noise). The fluid in which the particle is suspended has a Stokes drag coefficient $\xi_0 = 6\pi\eta a$ which opposes motion; the particle is also confined within an optical potential, assumed to be harmonic in form, with stiffness κ:

---

[1] Physically, this is true only for small displacements from the equilibrium position - see chapter 3.

$$m\ddot{x}(t) + \xi_0\dot{x}(t) + \kappa x(t) = F(t) \tag{2.11}$$

When exploring solutions to this equation it is worth noting that during all of these experiments, the inertial timescale of the fluid molecules (given by $t_{inert} \equiv m/\xi_0$) is several orders of magnitude shorter than the timescales on which our colloidal system operates [16]. This allows us to drop the inertial term $m\ddot{x}(t)$. Following the method of Gittes et al. [15], the resulting equation may be solved by means of Fourier transformation from time-domain to frequency-domain:

$$x(t) = \mathscr{F}^{-1}[X(f)] = \int_{-\infty}^{\infty} X(f)e^{-2\pi fit}df$$

The Langevin equation (without the inertial term) then assumes the following form in the frequency domain:

$$(f_c - if)X(f) = \frac{F(f)}{2\pi\xi_0} \tag{2.12}$$

Where we have introduced the term $f_c = \kappa/2\pi\xi_0$, the characteristic 'corner frequency' of the trap [67]. This complex function can be made more accessible by squaring its modulus, thus expressing the particle's movements in terms of a power spectrum

$$4\pi^2\xi_0^2(f_c^2 + f^2)S_x(f) = S_F(f) \tag{2.13}$$

As previously remarked, the power spectrum of the transformed Brownian force

$F(f)$ has a constant value across all frequencies, $F(f) = 4\xi_0 k_B T$. Solutions to equation (2.13) take the form of a Lorentzian distribution,

$$S_x(f) = \frac{k_B T}{\xi_0 \pi^2 (f_c^2 + f^2)} \tag{2.14}$$

Conceptually, the particle in the trap experiences free diffusion over short timescales (i.e. high frequency, $f \gg f_c$) but is bound by the optical potential at low frequencies - the corner frequency delineates the two regimes. As an aside, there are different conventions on how to assign an amplitude to the theoretical power spectrum; for example, the amplitude at zero frequency in reference [16] is only half of that in references [15, 68]. This difference stems from whether negative frequencies are taken into account when producing power spectra. Parseval's theorem states that the total power in an observed signal is the same in both frequency and time domains, so if $|P(f)|^2$ is an even function (which it is in our case), both conventions are shown to be equivalent

$$\int_{-\infty}^{\infty} |P(t)|^2 dt = \int_{-\infty}^{\infty} |P(f)|^2 df = 2 \int_{0}^{\infty} |P(f)|^2 df. \tag{2.15}$$

2.2.2 Frequency domain analysis - practice

The time-series data acquired in this experiment is discrete and purely real-valued. The Fourier transform of such a data set is generally complex; typically, part of the information extracted (the phase information) is discarded, leaving a power spectrum as a function of frequency, as detailed above. Data obtained using this method is quite noisy when initially transformed; the standard deviation of each frequency point is approximately the same as the mean [15]. To improve the accuracy of the fit parameters obtained, a single data set is divided into sections of equal length whose power spectra are then averaged.

When analysing the power spectrum obtained in a typical experimental run, a Lorentzian function (shown in a log-log plot in figure 2.1) is fitted to the data in order to determine both the trap stiffness and sensitivity — the latter allows a conversion between the raw particle position in volts, and its physical position in metres. The 'knee' of the graph (at $x = 1$ in the figure) is the corner frequency which is directly proportional to the trap stiffness, as described in the previous section. In order to obtain the sensitivity of the apparatus, a ratio is

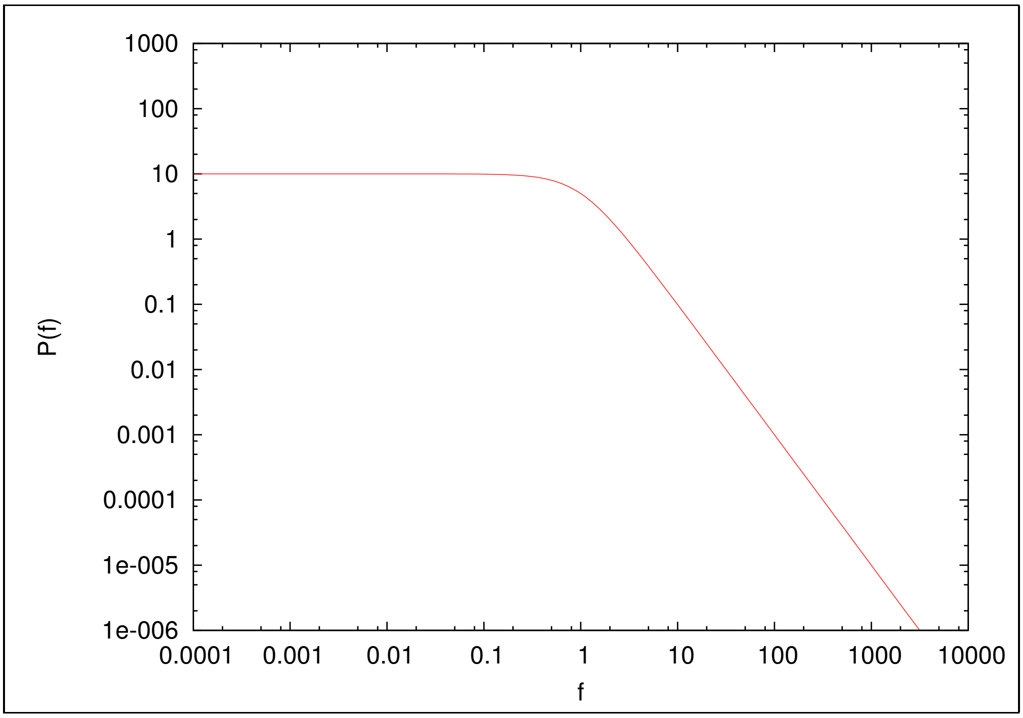

Figure 2.1: An ideal Lorenztian spectrum.

taken between the high frequency behaviour obtained in the experiment and that predicted using equipartition theory, essentially the ratio between measured and calculated diffusion coefficients (in V^2/s and m^2/s respectively - this process is described in more detail in chapter 3).

One difficulty in using frequency-domain analysis is the finite bandwidth of the recording apparatus. Although precautions have been taken in the analogue circuitry upstream of the acquisition card (namely an 80kHz low-pass filter), there is still the risk of aliasing, that is, signals at frequencies above the Nyquist critical sampling frequency f_N (5 or 10kHz in this case) are 'folded back' on to lower frequencies (see figure 2.2, especially data lying above 5kHz)[2]. However, our system is designed with the idea of examining the behaviour of colloidal suspensions at frequencies that are relatively low for this type of technique[3]; for calibration purposes there is sufficient data for an accurate fit below 4kHz on the frequency scale. At these frequencies, the contribution to the power spectrum from erroneous data that has 'folded back' from frequencies above f_N is small compared to that from the true data.

---

[2] The Nyquist frequency represents a theoretical limit on the information content that can be recorded by discrete sampling at a finite sampling rate. For example, a sine wave may only be accurately recorded if it is sampled at twice its own frequency.

[3] Several authors have performed studies at in the high frequency regime, particularly in references [69, 49].

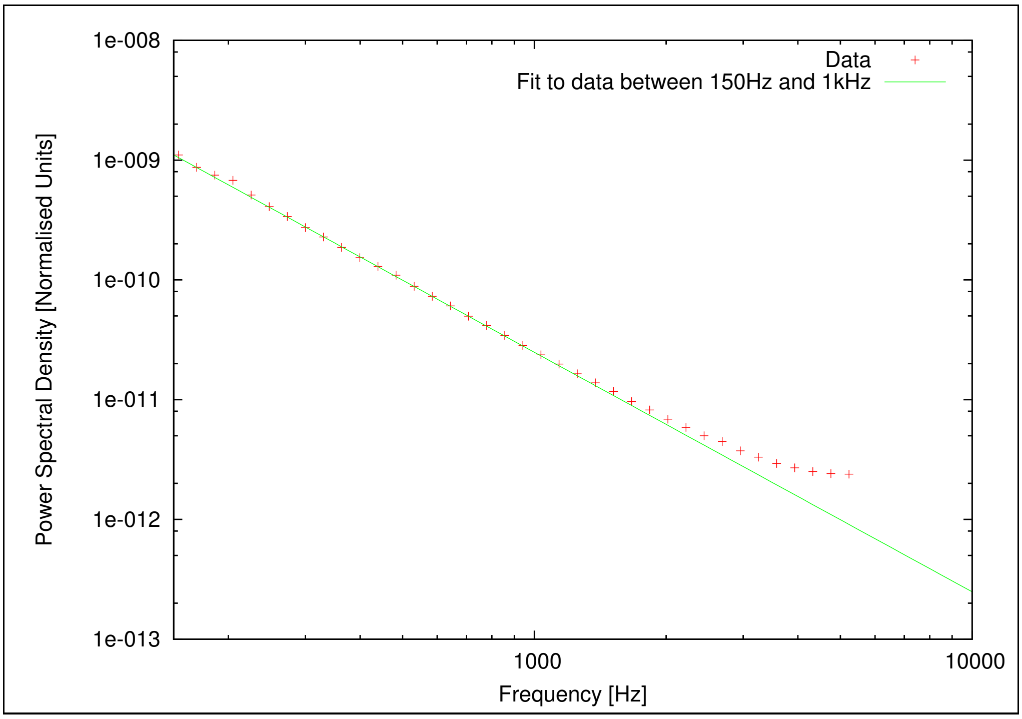

Figure 2.2: The effects of antialiasing on high-frequency data.

2.2.3 Time domain analysis

Position-time data is often a more intuitive way of visualising information than using the Fourier transform method. The concept of mean-squared displacement is a concise way of visualising the extent of a particle's freedom to move within an optical potential well, and the data produced lends itself well to the extraction of physically relevant quantities such as the diffusion coefficient. For a finite position variance (such as that exhibited by a particle in an optical trap in the long-time limit), the particle's mean-squared displacement can be estimated from the position autocorrelation function [7]:

$$\langle \Delta x^2(\tau) \rangle = 2\sigma^2 - 2\langle x(t)x(t+\tau) \rangle \tag{2.16}$$

With σ^2 being the variance of the (position) data set; the angle brackets indicate averages over all values of t. At timescales much longer than the inertial timescale, an idealised mean squared displacement takes the form

$$\langle \Delta x^2(\tau) \rangle = \frac{2k_BT}{\kappa}[1 - e^{-\kappa\tau/\xi_0}], \tag{2.17}$$

which is sketched in figure 2.3 below. The long-time limit of this function is proportional to the variance of the signal, as is the area under the power spectrum.

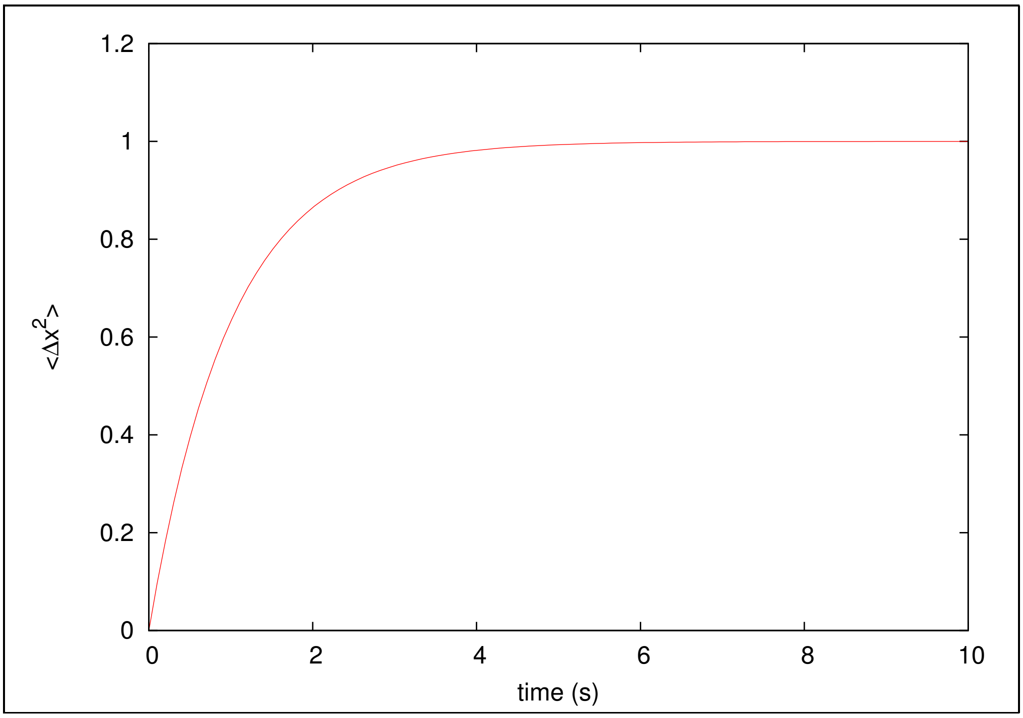

Figure 2.3: An ideal mean-squared-displacement graph.

Figure 2.3 shows free diffusion at very short times (the diffusion constant is found from the initial slope of the graph), followed by the confinement by the optical trap at longer times (the plateau level). In systems with slower dynamics (i.e. Colloidal glasses) we may expect to see more features in the long-time regime, up to tens of seconds, as the caging lengthscale approaches that of the optical trap confinement.

Chapter 3

Optical Setup and Characterisation

This chapter concerns the design, construction and calibration of an optical tweezers system. In the first section, basic design principles are given, including the importance of numerical aperture and the practical considerations relating to radiation pressure. The second section contains information about the particular setup used for this study[1], which relates directly to the third section, where the technique for detecting the position of a trapped particle in three dimensions is outlined. The final section of this chapter gives information about the calibration of the system, which is composed of two parts - force calibration and position calibration. The force calibration is achieved by applying a known force to the trapped particle, and measuring its displacement using a CCD camera attached to the system. For a truly harmonic potential, the displacement should be proportional to force. This is true here for small displacements, beyond which the force is mapped to displacement empirically.

The position detection system used for the main body of this work relies on a technique, described in detail in section 3.3, which involves the collection of scattered light to produce a voltage signal from a photodiode. As with the force-displacement relationship, this signal is linear for small displacements from the trap centre. In this regime, a volts-to-nanometres calibration may be obtained from power spectra of bead motion; this was outlined in chapter 2 and the practical details are explained in this chapter. For distances larger than about 250nm from the equilibrium trap position, the photodiode response shows significant nonlinearity. To correct for this, the CCD camera is used to record particle displacements (again, imposed by fluid flow), which are used to map the photodiode signal to actual distances.

---

[1] The apparatus was originally built by Dr. Jochen Arlt and myself; the division of labour has been detailed in the appendix of this thesis.

3.1 Optical tweezers basics

Fundamentally, optical tweezers are formed by tightly focusing a laser beam, and using the focal spot to pick up and move small dielectric particles, whose radius is typically of the order of 0.25–1μm. A key consideration is the numerical aperture of the objective lens (see figure 3.1); this is defined as n_m sin(θ/2), where n_m is the refractive index of the surrounding medium and θ is the beam cone angle. Typically, a water- or oil-immersion lens is used for tweezing. This is because the numerical aperture of the system is ultimately limited by the lowest refractive index through which the laser light passes. Thus by eliminating air from the beam path between objective and sample, numerical apertures greater than 1.0

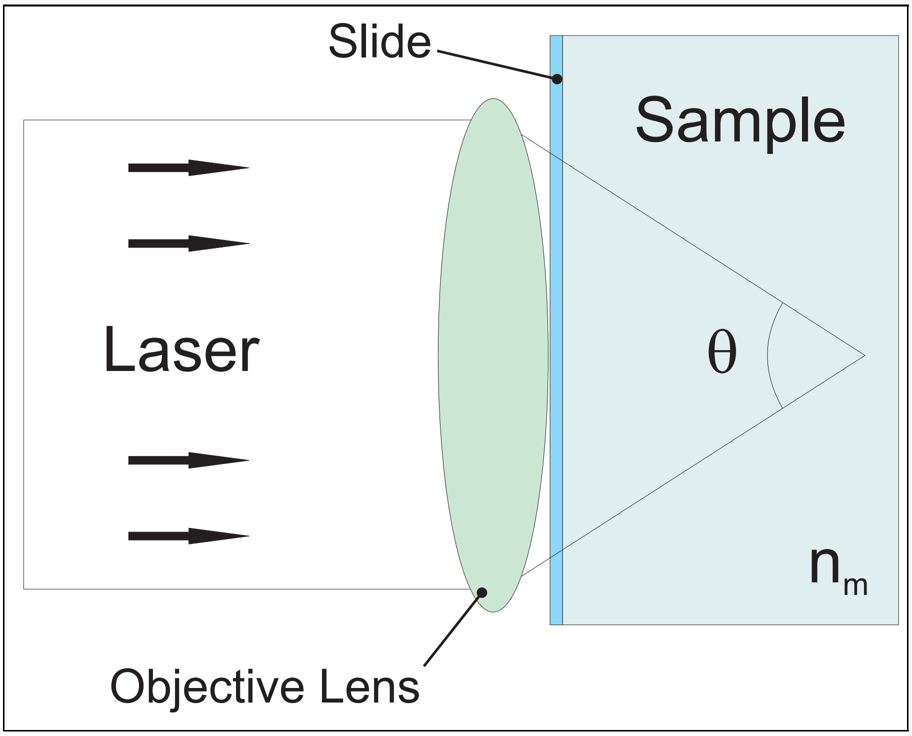

Figure 3.1: The numerical aperture of a lens is obtained from the geometry of the focused beam, and the refractive index of the sample medium. The immersion oil (which lies between the lens and the sample slide) has been omitted for clarity.

are possible. The most common method for implementing optical tweezers is to incorporate them into an optical microscope. Although they can be used with standard microscopes, an inverted configuration is usually employed (see figure 3.2), to offset the particle's weight with the laser radiation pressure.

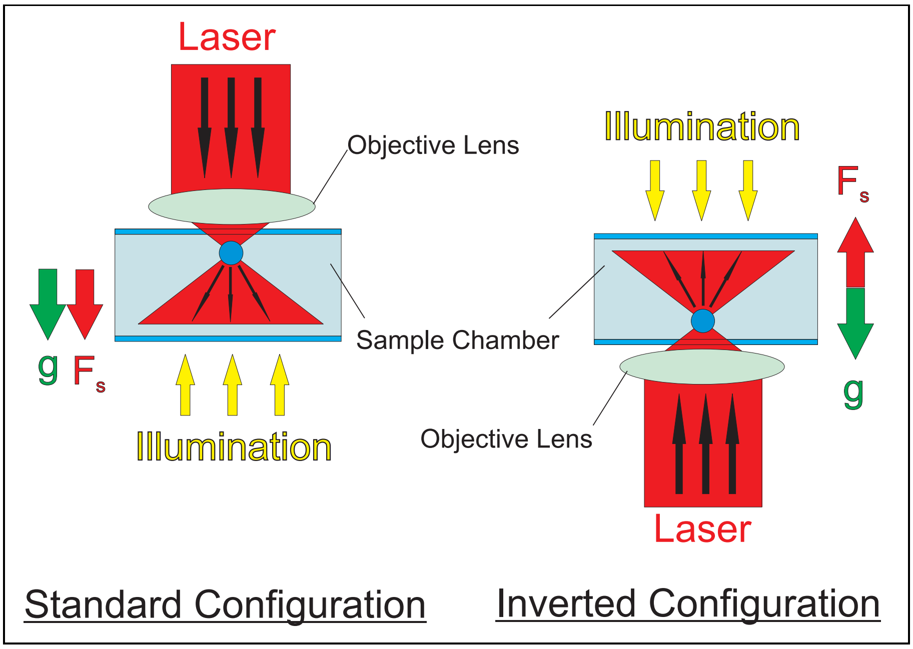
Laser
Objective Lens
g
F_s
Illumination
Sample Chamber
Illumination
F_s
g
Objective Lens
Laser
Standard Configuration
Inverted Configuration

Figure 3.2: Schematics for the two main optical tweezers configurations. In the standard configuration, the particle's weight (denoted $\mathbf{g}$) and the scattering force (denoted $\mathbf{F}_s$, see section 2.1.1) are parallel, whereas they are antiparallel in the inverted layout.

3.2 Apparatus

The setup [fig 3.3] used is built around an Nd:YAG solid state laser operating at λ =1064nm, focused into a custom-built microscope. A $\lambda/2$ retarder and polarizing beamsplitter are used to regulate the amount of power delivered to the sample; when this scheme is used, the laser may be operated well above the lasing threshold (total output power is of order 200mW) to take advantage of the better intensity stability. The actual amount of power at the sample is smoothly variable from a few microwatts to almost 200mW (allowing for losses in the rest of the optical system). The power delivered to the sample is monitored by a 10% pick-off mirror just before the final set of optics leading to the objective. In

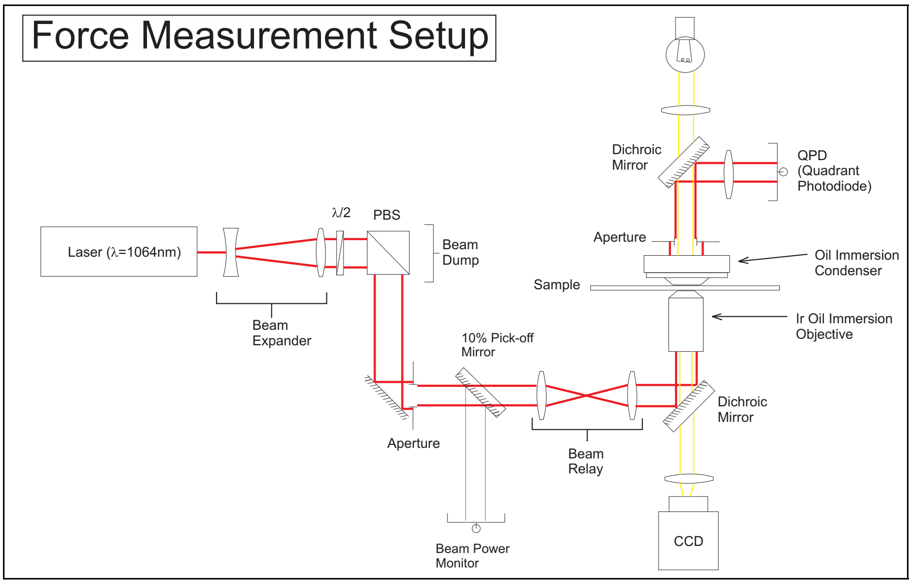
Force Measurement Setup
Dichroic Mirror
QPD (Quadrant Photodiode)
λ/2
PBS
Laser (λ=1064nm)
Beam Dump
Aperture
Oil Immersion Condenser
Sample
Beam Expander
Ir Oil Immersion Objective
10% Pick-off Mirror
Dichroic Mirror
Aperture
Beam Relay
Beam Power Monitor
CCD

Figure 3.3: Schematic of the optical tweezers force-measurement system.

order to move the optical trap within the microscope's field of view, an imaging system with a magnification of one (denoted 'Beam Relay' in figure 3.3) is used to image the surface of a mirror onto the back focal plane (BFP) of the microscope objective [70]. The surface of the mirror is therefore conjugate with the BFP of the objective, so as it is tilted, the angle between the beam axis and the objective's optical axis (which intersect at the BFP) is varied, without moving the point of intersection; this angular displacement in the BFP of the objective corresponds to a lateral displacement in the front focal plane. This arrangement ensures that the amount of laser power passed into the objective, and hence the strength of the trap, is unchanged as it is translated across the field of view. The aperture placed close to the mirror on the left-hand side of the beam relay is a useful addition. In our setup, the laser beam is wider than the mirror here, and this causes stray reflections from the optical component's edge. The aperture can be used to block these unwanted reflections which are detrimental to the microscope image quality and the trap strength.

A Nikon 100× oil immersion lens, with a numerical aperture (NA) of 1.4 is used both to focus the beam and to image the sample. The large numerical aperture of the objective lens is important because it has direct relevance to the relative trapping strengths in directions perpendicular and parallel to the laser axis - the trapping force is greatest in regions of strongest intensity gradient (as outlined in section 2.1.2).

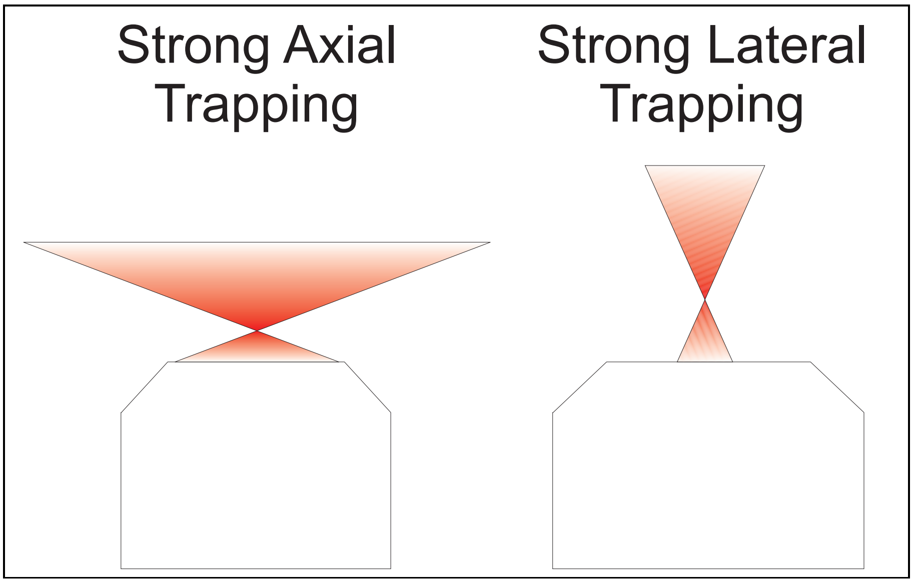

Figure 3.4: Schematic of the effects of NA on trapping strength.

Figure 3.4 shows schematically the effects of numerical aperture on trap strength. The beam with the largest numerical aperture has the strongest axial intensity gradient, leading to the strongest axial trapping [71, 72]. The opposite is true for the case with the strongest lateral trapping, where the variation in beam intensity along the beam axis on either side of the waist changes slowly, giving a dominant lateral trapping force [73]. A diaphragm may be used to decrease the beam width in the BFP (either at the physical location, or a conjugate plane), so a compromise between longitudinal and lateral trapping strength can be achieved.

The samples used in this work have a refractive index of around 1.49, which is close to that of both glass and the immersion oil used; optical aberrations inherent in water-based samples [74] are thus expected to be minimal and trapping remains strong even deep into the sample. The condenser lens plays a critical role in the force measurement setup because it collects the laser light downstream of the particle; both scattered and unscattered light are needed, as it is the interference pattern of these which gives information used for particle tracking [12]. The condenser used in this study was a 1.4NA oil-immersion condenser made by Nikon; this relatively specialist lens allows for a large range of numerical aperture values in the collection system, which is essential for high-resolution particle tracking [75]. An aperture in the BFP of the condenser controls the effective numerical aperture of the detection system.

The light passing out of the condenser is reflected from a dichroic mirror (which passes the microscope illumination) and through a lens which demagnifies the BFP image on to a quadrant photodiode (QPD) under strong reverse bias. The effect of the reverse bias is to increase the bandwidth of the photodiode, and reduce noise. The photodiode used here (a Hamamatsu S7479 model) is a pin-type device made from silicon. Other groups studying optical tweezers, with an interest in high-frequency behaviour [76, 77], have noted that silicon is increasingly transparent at wavelengths greater than 850nm, which limits the detection bandwidth in the infra-red — these groups have turned to specially engineered pn-type Si photodiodes, or those made from other semiconductors, such as InGaAs devices. However, as mentioned in chapter 2, all of the information we are interested in is obtained at frequencies below 5kHz, our system would not benefit greatly from such a modification.

The photocurrent generated by the laser light incident on each quadrant of the photodiode was converted to a voltage using analogue circuitry. The resulting voltages were recorded using a bandwidth of up to 20kHz using a 12-bit National Instruments data acquisition system (National Instruments PCI-MIO-16E-4), via a Labview frontend[2]. The voltages recorded can be converted to a record of particle position in the suspension when the instrument is correctly calibrated (see below).

The image in the BFP is a result of the interference between the light scattered by the trapped particle and the unscattered part of the beam. In essence, it is the projection of the Fourier transform of the particle's profile; as the particle is buffeted by Brownian motion in the suspension medium, the scattering pattern shifts in the BFP, and hence in the image on the QPD. The axial (z-) position of the particle is given by the total intensity of laser light incident on the detector. The Gouy phase shift [13, 75] acquired as the laser radiation passes through its geometrical focus gives rise to a phase shift between the scattered and unscattered light (the scattered light does not experience the phase shift) which is position-dependent. By measuring the changes in total intensity at the detector, the particle's axial position can be recovered. A lateral displacement of the trapped particle gives rise to a change in the angle between the unscattered light and the scattered light, corresponding to a lateral shift in the scattering pattern in the BFP of the condenser. The shift in the scattering pattern registers as a difference in voltage between the left and right halves of the detector for one in-plane axis, and the top and bottom halves for the other (denoted R_x and R_y in figure 3.5).

---

[2] The data acquisition routine was written by Dr. Jochen Arlt.

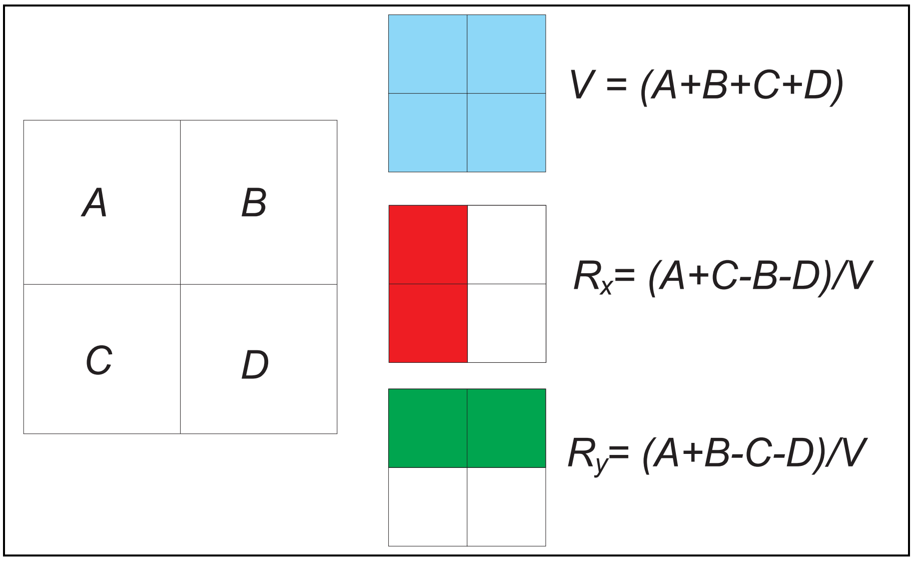

Figure 3.5: Schematic of the quadrant photodiode (QPD) signal processing. The factor of V^{-1} in the expressions for R_x and R_y is related to the normalisation of the signal, discussed in more detail in section 3.4.3.

Data was recorded as a byte stream of digitisation levels, which range from 0 to 4095. The voltage corresponding to one digitisation level can be chosen so as to ensure that the whole range of the signal is recorded, whilst optimising the resolution of the recorded signal. Typical scales used were a sum (z-axis) signal recorded over the range 0V to 10V, and lateral (x- and y-axes) scale from -1V to +1V. The exact ranges used depend on the trap strength being used; a stronger trap requires a more powerful laser beam, so optical neutral density filters to stop the QPD from saturating become necessary at the highest trap strengths.

3.3 Position detection

A description of the optical trapping mechanism, complementary to that put forward in chapter 2, is to say that optical tweezers operate by manipulating dielectric particles[3] using the momentum of the photons in a laser beam [35].

---

[3] Metal particles may also be trapped [31, 78], although the mechanism is slightly different.

The tracer (trapped) particles used in this study are all transparent at the laser wavelength used, and are distinct from their environment in having a different dielectric constant (and therefore refractive index). The tracers' negligible absorption at $\lambda_0 = 1064$nm is important in this experiment; particle heating can give rise to detrimental side-effects such as reductions in local viscosity and violent (on a micron-scale) convection currents[4]. Although the particles do not absorb the laser light, they do scatter it, and it is this phenomenon that allows the high resolution particle tracking at the heart of the force-measurement technique.

3.3.1 Small displacements (<400nm)

Lateral position detection

The pattern in the back focal plane of the condenser is essentially the Fourier transform of the tracer particle's refractive index profile; this takes the form of an Airy disk-like pattern of concentric light and dark circular fringes. A mathematically rigorous description of the distribution of radiation in this plane is quite intricate and beyond the scope of this research [75], but a simplified expression along the lines of reference [12] gives some insight into the mechanism responsible. As the trapped particle moves relative to its equilibrium position in the laser focus, the cone of light it scatters is deflected through an angle proportional to this displacement. As we are using a quadrant detector for these experiments, the most convenient expression is one that describes the fraction of the luminous intensity scattered into each half of the detector plane, $\Delta I/I_{total}$ as a function of displacement x along that same axis. For a particle of relative refractive index n_r in a solvent of refractive index n_s, near the focus of a beam of waist w:

$$\frac{\Delta I}{I_{total}} = \frac{32\sqrt{\pi} n_s a^3}{\lambda_0 w} \frac{n_r^2 - 1}{n_r^2 + 2}\, e^{-2(x^2/w^2)} \int_0^{x/w} e^{y^2}\, dy \tag{3.1}$$

It is quite surprising in some ways that this approximation is successful in describing results of trapping experiments using a 1μm polystyrene bead, as the equation is strictly only valid for a dipole at small displacements from the centre of the beam. Indeed, when applied to our system, the refractive index difference included in the prefactor gives rise to a maximum fractional intensity of around 1.5 (i.e. Scattered intensity greater than the incident intensity). This expression is only correct for small displacements from the equilibrium position in the optical trap, but its basic form (with a correctly scaled amplitude) seems to be about right for particles in our system - see section 3.4.4 for details of the comparison between experiment and theory.

---

[4] Several studies looking at heating effects in different particle/solvent combinations. Other works [79, 80] have found increases in temperature on the order of 10K/W under 1064nm irradiation for most sample combinations. The powers used in this study would result in sample heating of no more than 1.5K in the worst case.

Axial position detection

Axial position detection also relies on interference effects, but in a more subtle fashion. There is an anomalous phase effect in focused light beams [81] whereby the change in phase along the optical axis is not a linear function of displacement, due to the effects of finite wavelength. This phenomenon is harnessed to give information about the trapped bead's axial position [13]; the light scattered by a probe particle interferes with the unscattered light further down the system, with a phase difference determined by the particle's axial displacement relative to the geometrical focus. The diameter of the aperture in the BFP of the condenser has a subtle effect on the axial resolution of the position-detection system; as the aperture is reduced, thereby restricting the numerical aperture of the system, the detection volume available is enlarged - this effect is analogous to the reduction in axial trapping stiffness by reducing the numerical aperture of the incoming beam. As the beam becomes narrower, the intensity varies more slowly on either side of the focus, stretching the 'focal region' longitudinally. This increases the effective detection volume *and* (somewhat counter-intuitively) the detection system sensitivity [75]. It should also be noted that the size of the condenser's numerical aperture affects lateral and axial sensitivities in opposite senses.

3.3.2 Larger displacements (>400nm)

There is little in the literature, either in theory or experiment, that discusses position sensing at large displacements using a QPD. According to other sources [12], the response of the photodiode detector is linear for small displacements, but departs significantly from linearity at larger displacements. This difference has been documented in other studies focusing on instrumentation [82], but most applied studies thus far have been working in the small displacement range (used in this work as a passive rheology technique). The main challenge in interpreting the system's response to large displacements is that there is a non-linearity not only in the sensitivity of the detection, but also in the force-displacement relation of the optical trap. In order to correctly calibrate the system for investigating the larger displacement regime, video microscopy can be used to provide an independent measurement of particle displacement.

3.4 Optical characterisation

In this section, the force and lengthscale calibrations are verified using video microscopy and image processing. Firstly, an independent measurement of the trap stiffness is obtained, from video microscopy and an imposed force on the probe particle (independent of the QPD). Secondly, the lengthscale calibration is verified by comparing particle displacements measured by video imaging and the QPD reading (independent of the imposed force).

3.4.1 Verification of force calibration

In order to test the instrument, a number of experiments were performed on a control system (a Melamine tracer particle in the index/density matching solvent used for preparing the colloidal samples - see chapter 4). The first part of the calibration involves confirming the force constant (stiffness, κ) obtained from the power spectrum analysis. To achieve this, a known force is applied to a trapped bead by fluid flow - the flow is laminar as the system operates at very low Reynolds' numbers, $Re \sim 1\times10^{-5}$. The displacement from equilibrium is measured with a CCD camera connected to an image grabbing card. Imaging a particle's motion under flow provides not only a measurement of the detection non-linearity (see below), but also the nonlinearity of the optical potential, which can be important for large-displacement experiments[5]. The force is applied by holding a particle in the optical trap and moving the sample fluid around it by translating the sample stage; the resulting viscous force is related to the velocity of the liquid via the familiar Stokes equation, and is balanced by the force due to the optical potential gradient:

---

[5] This nonlinearity has been exploited in reference [83] where experiments are performed using a constant-force configuration.

$$F = 6\pi\eta a v = \kappa x. \tag{3.2}$$

A range of stage speeds (from 40 to 170μm/s) allows a range of forces to be applied to the particle. The sample stage was translated over a distance of around 75μm, with a periodic triangle-wave motion. This meant that the particle was at its maximum displacement on either side of the equilibrium position for the majority of a translation cycle. The images recorded were post-processed using IDL[6] to give time-averaged particle positions, adding the pixel amplitudes in successive frames and dividing by the total number of frames. The two circular features in the resulting images (examples are shown in figure 3.6) show the average positions of maximum displacement.

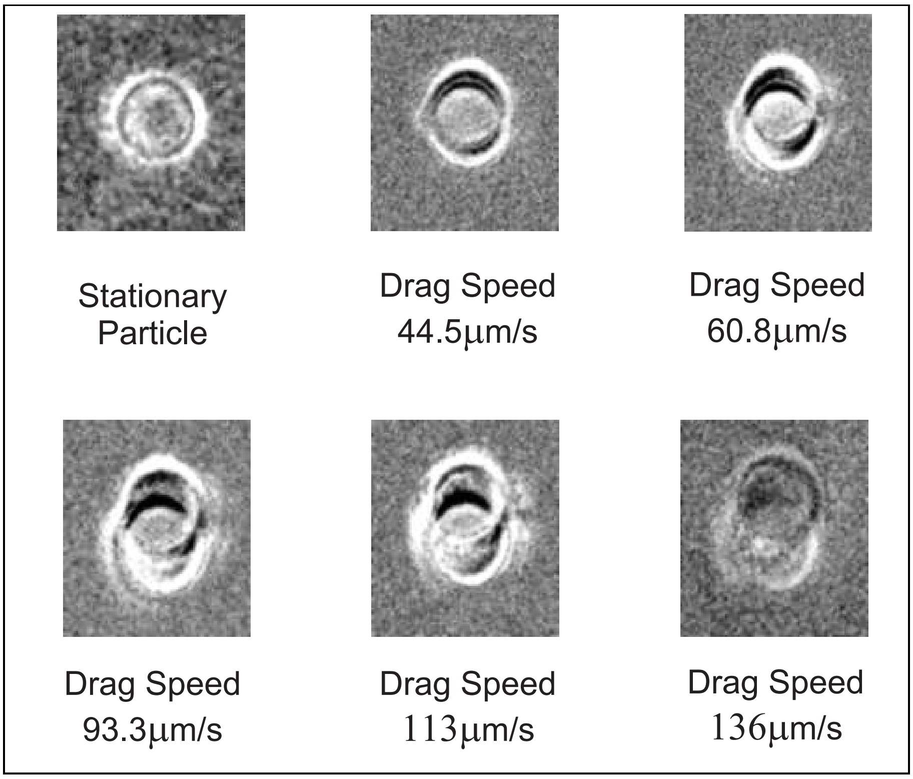

Stationary Particle

Drag Speed 44.5µm/s

Drag Speed 60.8µm/s

Drag Speed 93.3µm/s

Drag Speed 113µm/s

Drag Speed 136µm/s

Figure 3.6: Images recorded using a CCD camera attached to a computer with a frame-grabbing card.

---

[6] The IDL routines were modified from programmes written by Eric Weeks.

The number of pixels between the same edge of the upper and lower image of the particles gives the distance between the two diametrically opposite positions; half of this figure gives the displacement from equilibrium in terms of pixels. A precision ruled slide was then imaged and analysed to give the conversion factor between pixels and micrometres. A comparison of applied force to the recorded (calibrated) displacement gives a value for the trap stiffness. This experiment was repeated at several different laser powers; as the trap stiffness is directly proportional to the laser power (see equation 2.9), it is straightforward to rescale the results to lie on the same line. The results presented in figure 3.7 have been normalized in terms of the maximum power.

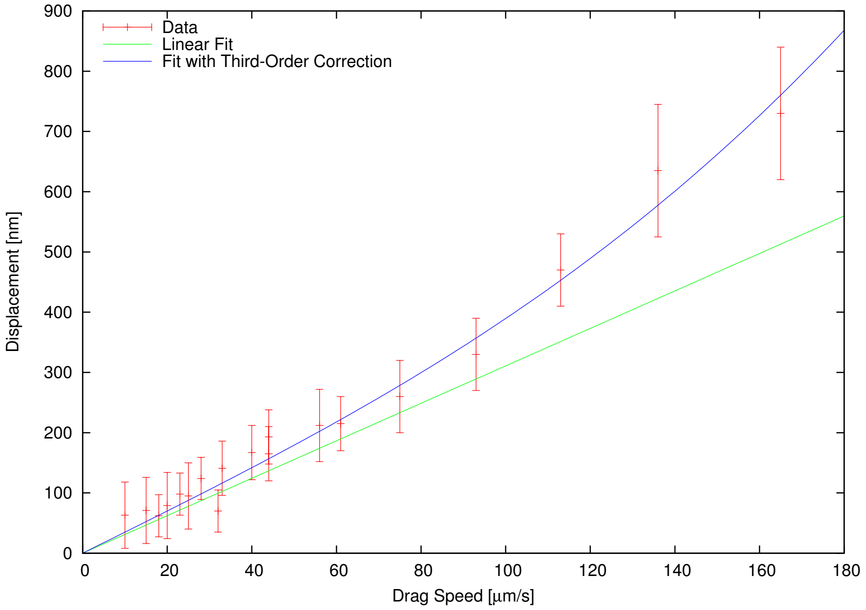

Figure 3.7: Displacements from equilibrium as a function of stage speed, as recorded by the CCD camera.

The value of stiffness extracted from the power spectrum measurements agrees with the small-displacement measurements under flow to within the error on the CCD data. At larger stage speeds, the measured displacements are almost 50% larger than a linear stiffness would suggest; the tracer is in the anharmonic region of the optical trap. In order to correctly describe the optical force at these larger displacements, a third-order term is included in the force-displacement equation,

$$F = \kappa x + \vartheta x^3, \tag{3.3}$$

where ϑ is a fitting parameter. This allows a much more accurate measurement of large forces in the colloidal experiments.

Comparison with theory

After the power-spectrum stiffness calibration had been checked, it was possible to make a direct comparison with the theory outlined in section 2.1.2. A particle was trapped at 20μm from the lower surface of the sample cell, and recordings made of its position using several different laser powers (and hence trapping stiffnesses). Equation 2.10 was used to obtain predictions of the trapping stiffness as a function of power, using the value $\epsilon = 3$ from reference [55], and the value for beam waist size ω_0 from the parameters used in reference [12] adjusted to reflect our different solvent refractive index. The results are presented in figure 3.8, where good agreement is found.

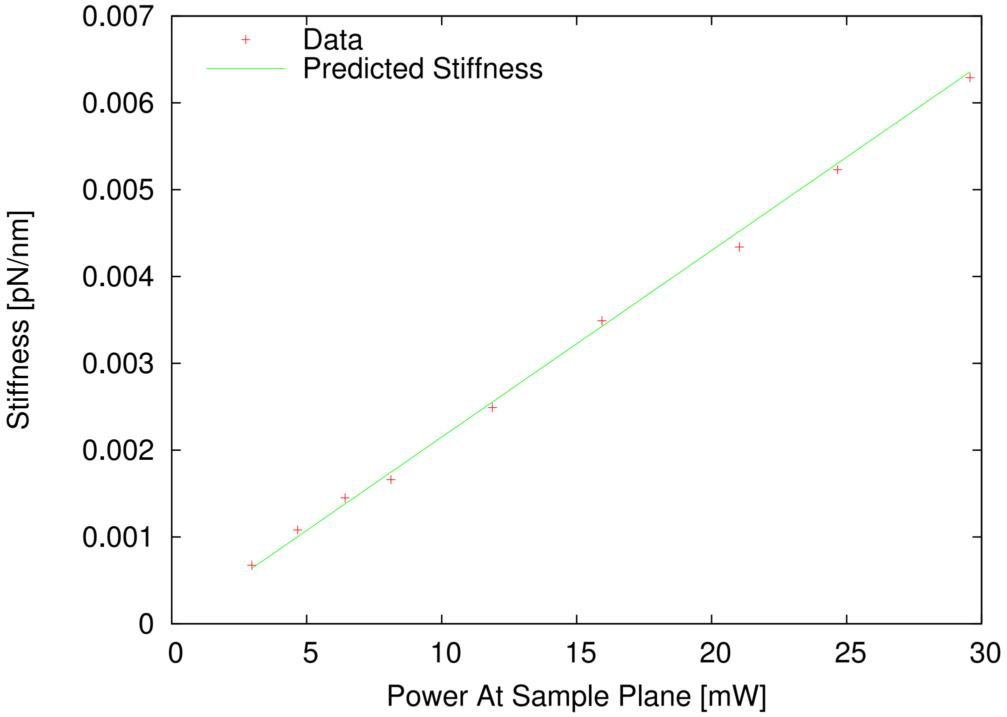

Figure 3.8: Optical trap stiffness as a function of laser power, with both data (red crosses) and theoretical prediction (green line).

3.4.2 Calibrating lengthscales

As described in chapter 2, the power spectrum of a trapped bead's motion in bare solvent is given by a Lorentzian function,

$$S_x(f) = \frac{D_0}{\pi^2} \frac{1}{(f_c^2 + f^2)}, \tag{3.4}$$

where

$$D_0 = \frac{k_B T}{6\pi\eta_0 a} = \frac{k_B T}{\xi_0}. \tag{3.5}$$

Here f_c is the corner frequency, η_0 is the bare solvent viscosity and a is the particle radius. For small bead displacements within the trap, the detector response is linear, implying that the power spectrum of the recorded voltage signal is also a Lorentzian. This recorded power spectrum may be fitted, using D_0 and f_c as fitting parameters; the measured value of D_0 (in $\text{V}^2\cdot\text{Hz}$ for the recorded signal) leads to the conversion between volts and nanometres (the equivalent quantity for the physical power spectrum is measured in $\text{m}^2\cdot\text{Hz}$). This procedure was performed using several different laser powers, and it was found that the sensitivity (in mV/nm) is directly proportional to laser power (see figure 3.9). Clearly, the z-axis sensitivity (measured on the right-hand vertical axis) is much smaller than that of the x- and y-axes. This is because the z-position signal (as described in chapter 3) is a fluctuation on the order of millivolts, on top of a signal on the order of volts (i.e. fluctuations in the total received power at the QPD); the z-position resolution is limited by the dynamic range of the data acquisition card.

Although values for the sensitivity and stiffness were actually obtained from a power spectrum analysis, a more intuitive representation of the same data is the particle mean-squared displacement. The results in figure 3.10 show the mean-squared displacements as a function of laser power (all powers are equivalent to those at the back focal plane of the microscope objective). As was discussed in chapter 2, there are two main features of interest here: The initial slope (determined by the diffusion coefficient for a tracer particle) and the long-time plateau level (which is determined by the trap stiffness).

The viscosity of the solvent at lab temperature, $\eta_0 = 2.56 \times 10^{-3}\text{Pa}\cdot\text{s}$, has already been measured (section 4.5.2), so it is straightforward to obtain a value for the diffusion constant. The value obtained, $D_0 = 8.85 \times 10^{-14}\text{m}^2/\text{s}$, can

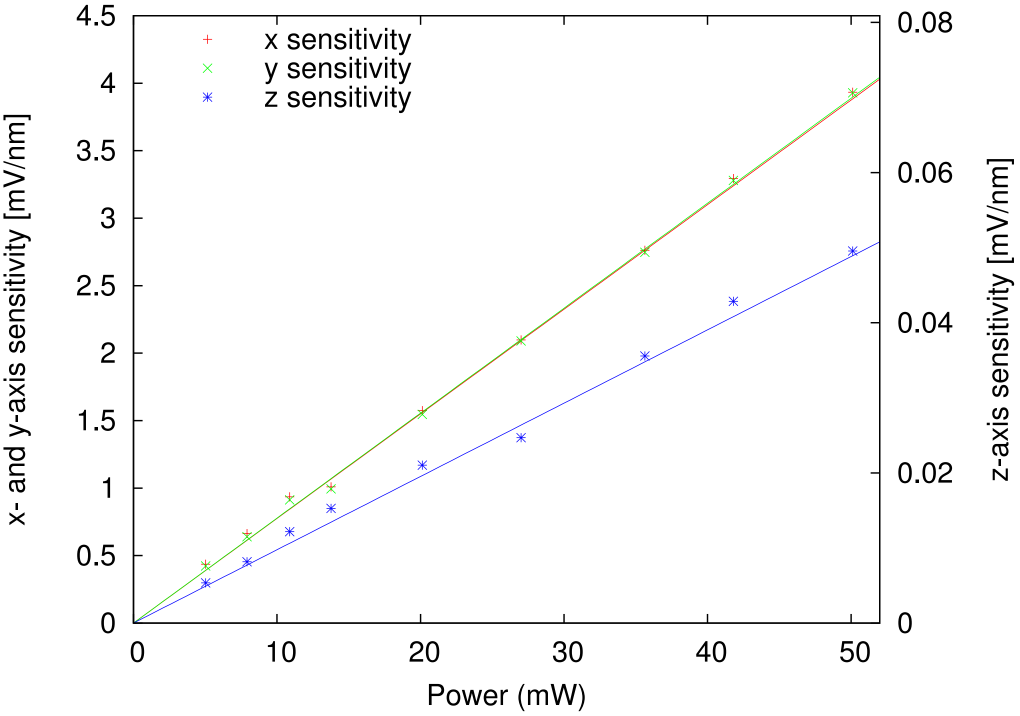

Figure 3.9: Sensitivity of the detection system as a function of laser power. x and y sensitivities are plotted on the left-hand vertical axis, and z sensitivities on the right.

be used to predict the evolution of a tracer's mean-squared displacement in the absence of an optical trap, $\langle \Delta x^2(\tau) \rangle = 2D_0\tau$. This function is plotted as a thick line in the upper graph of figure 3.10. As expected, all of the measured curves tend to this line at the shortest times, when free Brownian motion dominates.

3.4.3 Aside - power spectra of normalised data

The diffusion constant is central to the first stage of the main results chapters, examination of 'normalised' power spectra (more precisely, the power spectra of normalised data), which allow the comparison of diffusion constant between different samples, independent of trap stiffness. In all experimental runs, the raw signal from the QPD is recorded as a sequence of voltages; these voltages may be converted into positions using the sensitivity calibration outlined above. However, the detector sensitivity is proportional to laser power; different powers give different values for the raw diffusion coefficient (in $V^2 \cdot Hz$). In order to

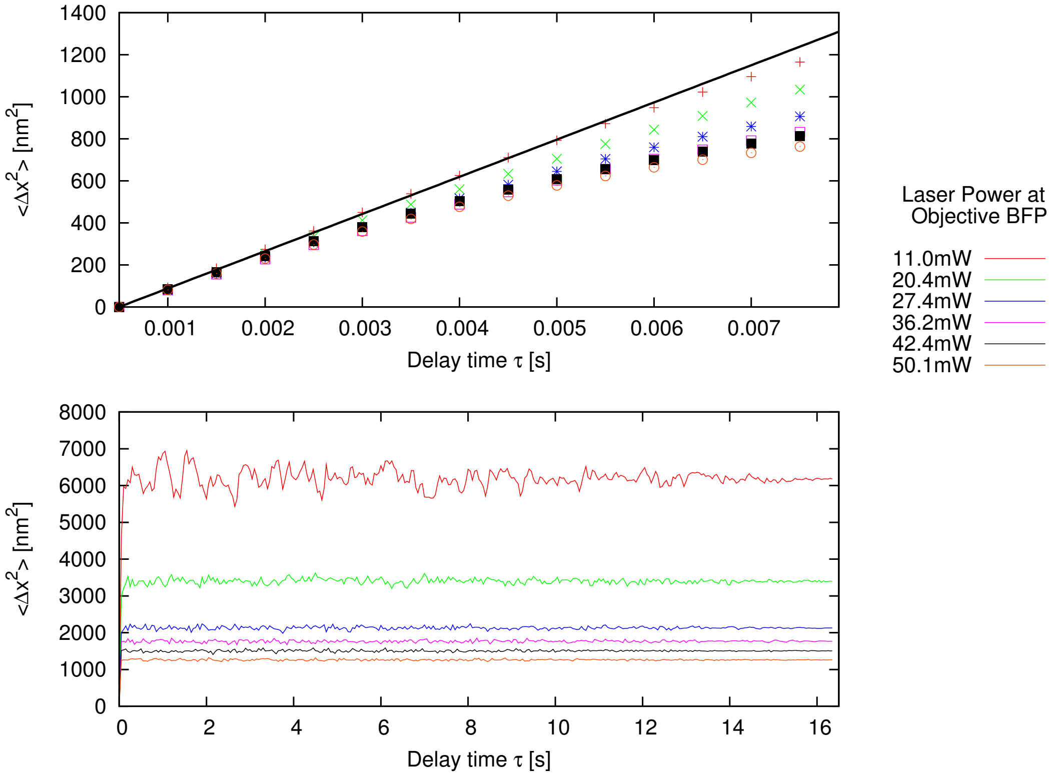

Figure 3.10: One-dimensional mean-squared displacements for particles in a bare solvent, with different laser powers (and hence trap stiffness). The amplitudes of the long-time plateaux *increase* with *decreasing* laser power; the curves are stacked in the same order as the figure key. The thick line in the upper plot represents the mean-squared displacement of a freely diffusing tracer in this solvent, calculated using the solvent viscosity measured in section 4.5.2.

compare experiments with different laser powers, the x and y voltage signals are divided by the z signal (the total power at the QPD) at each time point, so that only *relative* signal fluctuations are observed[7]. At high frequencies, the particle behaviour is not affected by the laser trap, and the normalisation (division by the z-signal) gives high frequency behaviour that is independent of trap power. The effects of this are illustrated in figure 3.11, where it can be seen that although the laser power varies by a factor of ten across the range of measurements, the high-frequency data overlaps; only the value of the corner frequency is affected. At higher frequencies ($f \gg f_c$), the freely diffusing behaviour is independent of trap strength, and (by virtue of the normalisation) free from the power-dependent

---

[7] This procedure also removes erroneous correlations between the x/y voltage signals and the z signal.

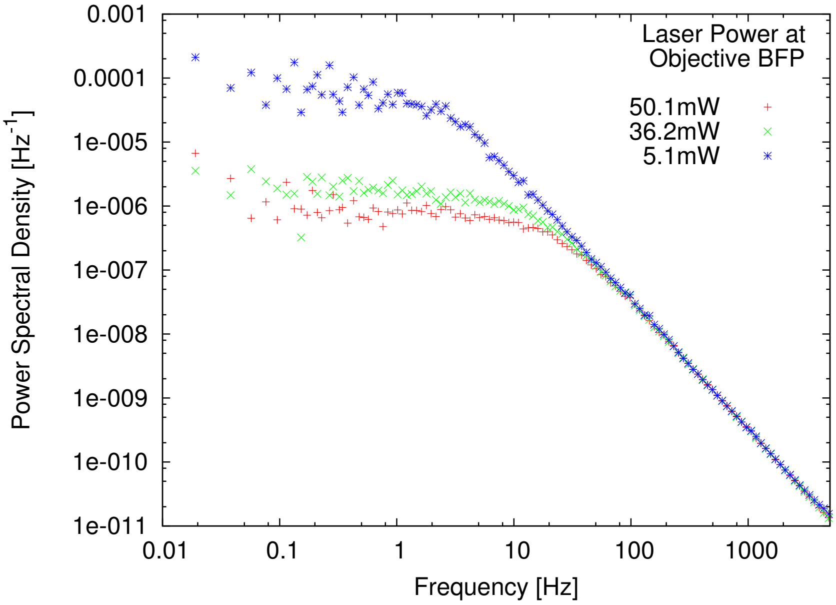

Figure 3.11: Normalised x-axis power spectra for a selection of the experiments in figure 3.10. Note that the high-frequency portions of the graphs overlap.

sensitivity, with an amplitude that is again directly proportional to the tracer's diffusion coefficient in bare solvent, D_0. With a colloidal host present, the high-frequency amplitude decreases. This is because the diffusion coefficient – strictly speaking, the short-time self-diffusion coefficient, D_s^s – is inversely proportional to the high-frequency viscosity (η_∞). Frequency-dependent viscosity is discussed in more detail in chapter 4, but broadly speaking, the increased viscosity in colloidal samples is due to hydrodynamic interactions between probe and host particles. This phenomenon offers a method of obtaining D_s^s for a suspension, by comparing the relevant portion of a colloidal power spectrum to the same range in a bare solvent measurement. Fits to the data give estimates of the standard asymptotic error in the corner frequency and spectrum amplitude; both are typically less than 1%.

3.4.4 Verification of length scale calibration

Small Displacements

To verify the small-displacement lengthscale calibration obtained from the power spectrum method, a particle was stuck to the surface of a glass slide and scanned through the focus of the laser, (the centre of the optical trap) in a direction perpendicular to the optical axis. A calibrated piezoelectric transducer (PZT) was used to translate the sample stage, in order to move and record the stage position with a high enough precision [67, 84]. There are certain difficulties to this technique, such as scattering from the slide/solvent interface, and ensuring accurate centering of the particle along the axes perpendicular to translation. The former is less of a concern in this case, because the refractive index difference between the solvent and glass is small (around 1%, corresponding to a Fresnel reflection coefficient of 3.3×10^{-3}), so little scattering is expected. The second issue (that of alignment) is more troublesome, but as long as the particle is close to being centred in these planes (i.e. the centre of the particle passes within ~200nm of the geometrical laser focus), the voltage signal recorded by the QPD will vary linearly with displacement.

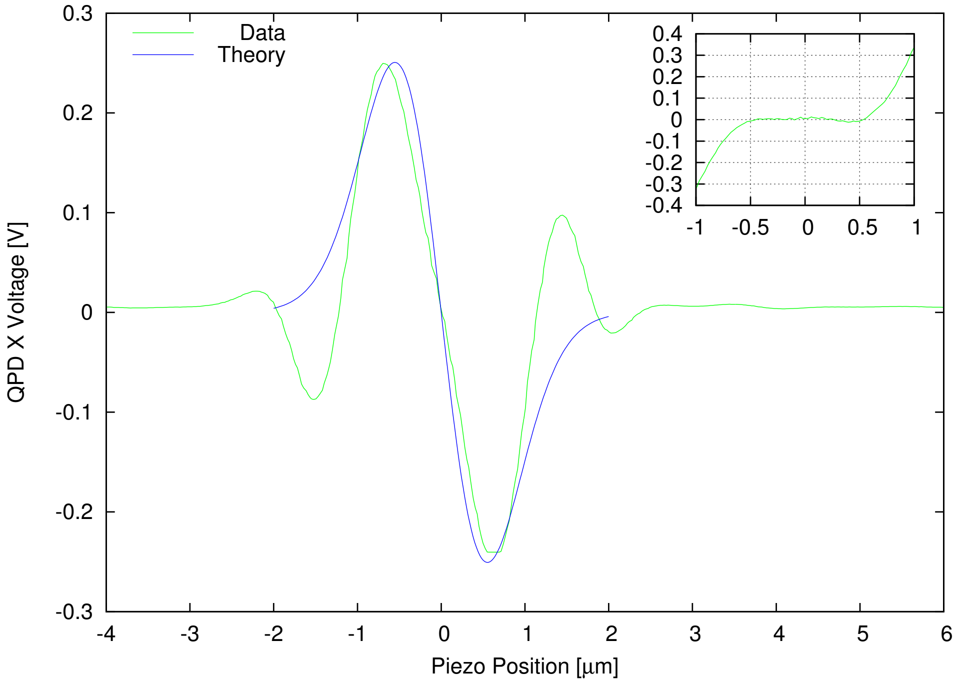

Figure 3.12: QPD response to a known bead displacement. The inset shows the deviation from a straight line fit to the portion of data between -0.35μm and 0.35μm.

The graph in figure 3.12 shows the result of this experiment performed with the stuck bead translated through the laser beam close to the region of highest intensity. The inset to the graph shows the deviation of the QPD response from a straight line fit to data between -0.35μm and 0.35μm. Although there is significant nonlinearity in the QPD response for large displacements from the trap centre, this measurement shows that the response of the system to small displacements is linear, in agreement with [82]. The value extracted for the sensitivity of the trap is 0.455±0.005mV/nm, which is within the experimental errors of 0.44±0.02mV/nm, the value extracted from the power spectrum measurements at the same laser power. The theory curve in figure 3.12 was obtained using the formulae in [12]. As discussed in chapter 2, there are some issues with the applicability of this theory to our optical tweezers system. It is worth noting, however, that the overall shape of the theory curve is not totally dissimilar to the data.

Larger Displacements

Full lengthscale calibration of the system relies on a comparison between video microscopy and the data obtained using the QPD. The position measurement system was set to record during the force calibration runs, so a set of apparent displacements was recorded. The effect of an additional flow force is that the equilibrium position of the particle is shifted relative to the non-flow condition, but as the optical potential is parabolic, the probability distribution of particle positions is still Gaussian. Histograms of particle position were made across the length of a measurement, and the modal bead positions extracted (the distribution of particle positions is of course bimodal, as the stage velocity reverses periodically - see figure 3.13). The work in [82] shows that the discrepancy between actual displacements and those measured by the QPD increases rapidly outside the linear range of the trap, and the results in figure 3.14 show a similar trend, with the reported and actual displacements diverging significantly beyond 200nm from the trap centre. The data was fitted using a cubic curve knowing that the reported displacements are approximately correct for small values. The best fit was given by:

$$y = (2.10608 \times 10^{-6})x^3 + x, \tag{3.6}$$

which is plotted in the figure 3.14, along with a line to demonstrate a 1:1 correspondence. This equation was used to map larger displacements obtained by the QPD on to actual displacements when making measurements on colloidal systems.

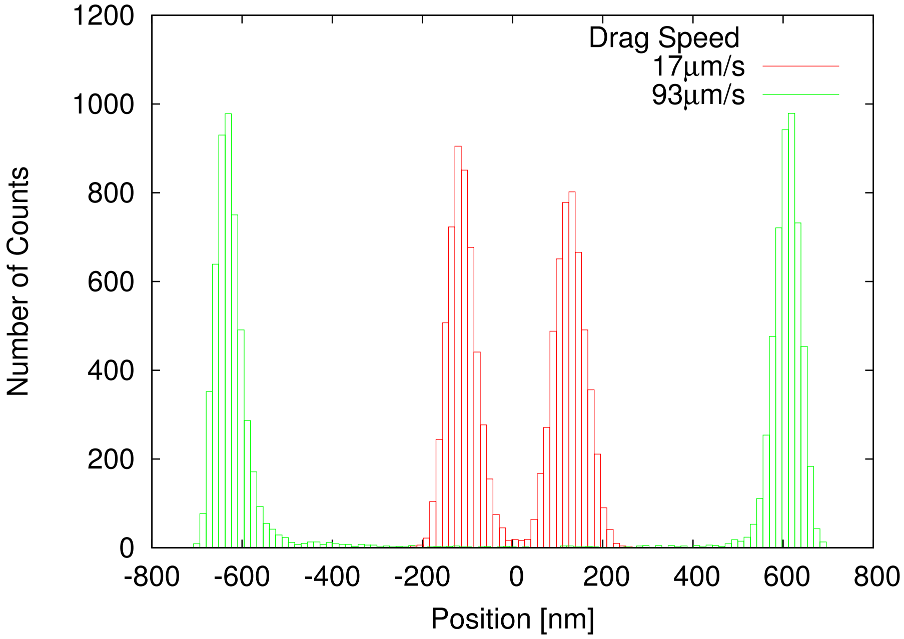

Figure 3.13: Histograms of particle position from Stokes drag measurements. The peaks in the negative and positive halves of the graph are different heights in the case of the slower drag speed because the recording does not cover a whole number of cycles of positive and negative velocity.

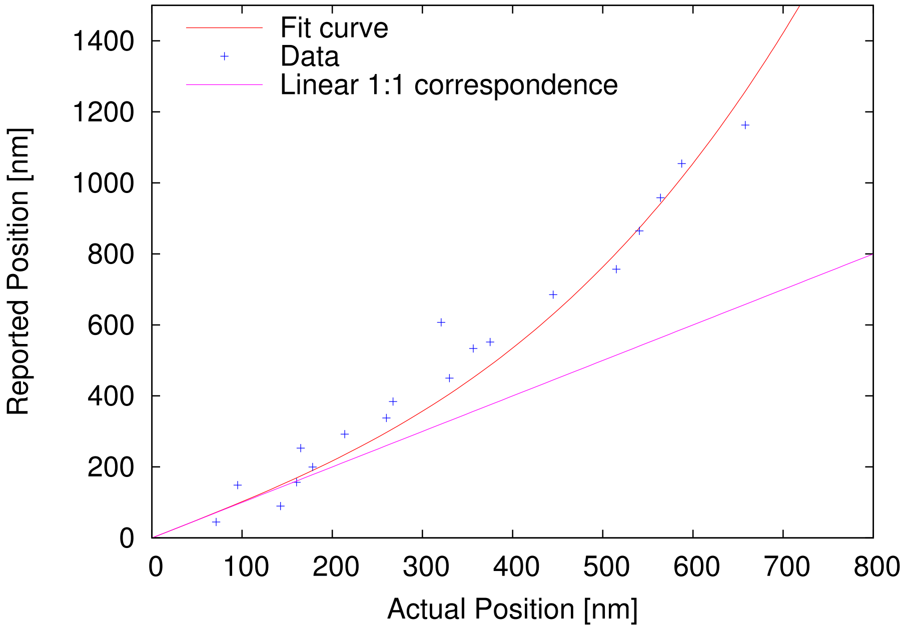

Figure 3.14: Actual displacements against displacements according to QPD.

3.5 Calibration summary

The final results in this chapter (figures 3.15 and 3.16) show the results of a typical measurement in bare solvent, with the correctly calibrated lengthscales. Figure 3.15 shows a 2D histogram of particle position over time. A one-dimensional projection of the distribution is Gaussian - projections of the X- and Y-positions are shown in figure 3.16 along with fitted curves. The variance of the histogram is given by $\sigma^2 = k_B T/\kappa$, as implied in section 2.2.3. This allows us to use the fitting procedure to extract a value for the stiffness of the trap, which gives a final confirmation of both lengthscale and force calibration methods. The values extracted from histogram fits are $\kappa_x = 6.08 \pm 0.03 \times 10^{-6}$ and $\kappa_y = 7.01 \pm 0.07 \times 10^{-6}$N/m, which agree well with the values $\kappa_x = 6.3 \pm 0.3 \times 10^{-6}$ and $\kappa_y = 7.0 \pm 0.3 \times 10^{-6}$N/m obtained by a power spectrum analysis.

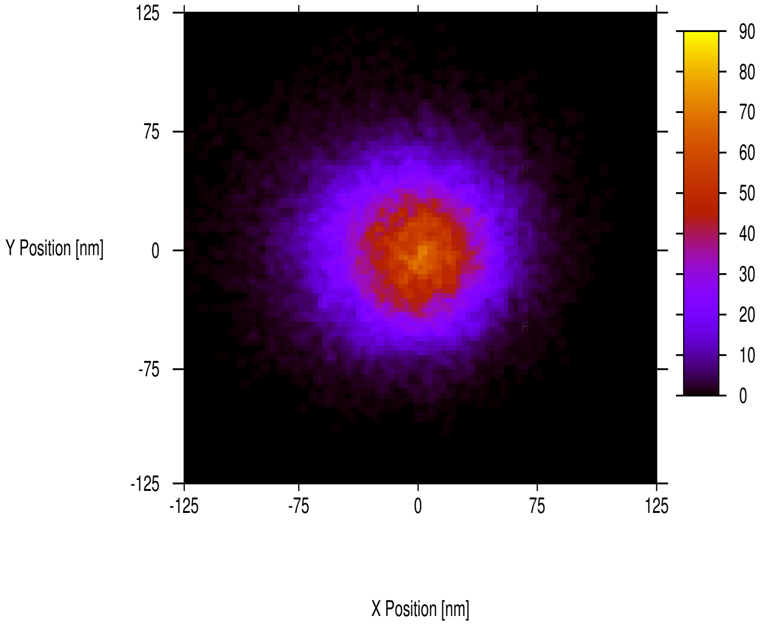

Figure 3.15: 2D histogram of tracer position in bare solvent, at a sampling rate of 2kHz, bin size 2.5nm. The colour bar indicates the number of scans falling in each bin.

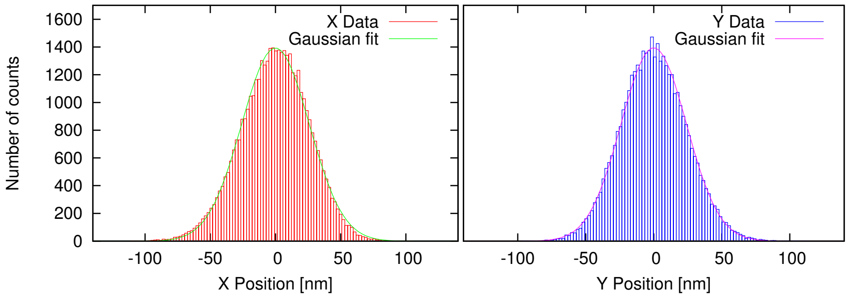

Figure 3.16: Histograms of X- and Y-coordinates. The curved lines are Gaussian fits to the data.

Chapter 4

Colloids Background and Methods

Colloid science is the study of a wide variety of substances, all characterised by a particular material nature, and a particular length scale. The material nature of these systems is that of a dispersion of finely divided particles in a chemically distinct dispersion medium; the length scales are such that the particles are small enough to be affected by Brownian motion but too large for quantum effects to prevail. The dispersion medium is generally taken to be a continuum, with bulk properties such as dielectric constant and density, simplifying both theory and experimental considerations.

There are many reasons for studying colloidal systems. For example, industrial interest in academic research findings is widespread, encompassing fields as diverse as the stabilisation of paints and foodstuffs to the dynamics of soot in industrial smokestacks. Another area in which colloidal physics has had a great influence is in the field of condensed matter science: colloids can be shown to act as a tunable model atomic system. The main body of new work in this thesis examines the material properties of one of the best characterised colloidal systems, a so-called hard-sphere system.

4.1 Observation tools

One of the advantages that colloidal lengthscales offer is that individual particles are large enough to be observable with standard optical techniques but small enough to be influenced by Brownian motion. As well as optical tweezers, two other techniques deserve a mention: Light scattering and confocal microscopy.

The former (in static form) operates in reciprocal space and offers a high-resolution, ensemble-averaged picture of colloidal shape and structure. The latter is a real-space technique for making precise quantitative measurements of particle position.

4.1.1 Light scattering

Scattering experiments have been used for many years to probe the structure of materials. Scattering of radiation in the optical range in particular has relevance to colloid science because the wavelength of light is comparable to the size of the particles. Although there are many highly rigorous descriptions of the scattering of electromagnetic waves from inhomogeneous media (see, for example, chapter 13 in reference [81]), this study uses only one aspect of the field: Static light scattering to determine the core radius of the colloidal particles[1]. It is assumed here the scattering of light is elastic (which is reasonable as the momentum imparted to a colloidal particle by a photon is many orders of magnitude smaller than the thermal agitation the particle receives from the solvent). The incident and scattered wavevectors are related by $\mathbf{Q} = \mathbf{k}_s - \mathbf{k}_i$, and the magnitude of the scattering vector $\mathbf{Q}$ is related to the scattering angle θ by

$$Q = \frac{4\pi n}{\lambda} \sin(\theta/2), \tag{4.1}$$

where λ is the vacuum wavelength and n is the refractive index of the suspension medium. This is illustrated in figure 4.1 below. Static light scattering (SLS) is used in this work to characterise the colloidal samples, to provide an accurate determination of our host particle core size. The approach to determining the particle size is that described in [23], outlined here. In the first-order Born approximation (single scattering limit), the field scattered by a single particle is obtained by summing the contributions from individual scattering volumes

---

[1] This is the smaller of the two measures which could be considered the particle ‘size’; the other is the hydrodynamic radius of the particle, which includes the coating of polymer hairs used for stabilising the particles against aggregation and the solvent dragged around as the particle moves.

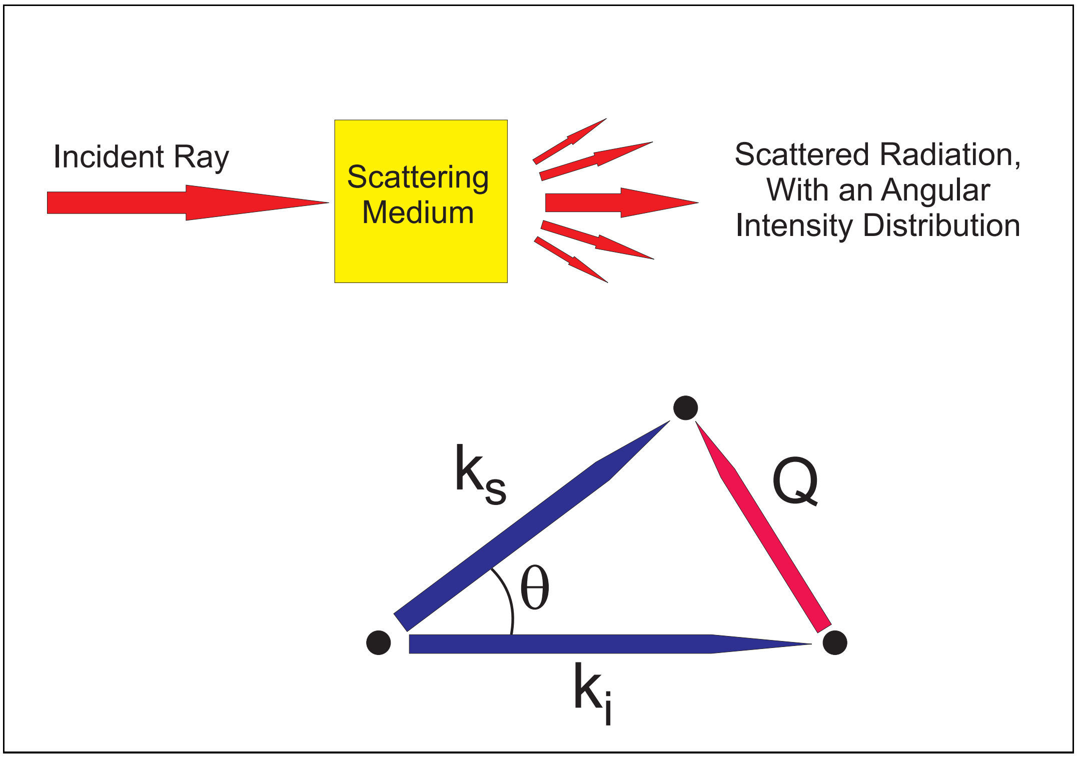
Incident Ray
Scattering Medium
Scattered Radiation, With an Angular Intensity Distribution
k_s
Q
θ
k_i

Figure 4.1: Schematic of the light-scattering process.

throughout the sphere, and is proportional to

$$b(Q) = 4\pi \int_0^R r^2 \mathrm{d}r [n_p(r) - n_m] \, \frac{\sin(Qr)}{Qr}, \tag{4.2}$$

where r is a position from the centre and R is the radius of a particle. The term $n_p(r)$ describes the refractive index profile of a particle, and n_m is the refractive index of the suspension medium. For the sake of simplicity, the particles are taken to have a constant refractive index for $r < R$. This approximation neglects the solvent penetration that occurs when particles are transferred from one medium into another (as the particles absorb slightly [85]), but the results show that this is not a bad approximation. Averaging over N particles with centres at positions $\mathbf{r}_i$, the time-dependent scattered electric field and scattered intensity are given by

$$E(Q,t) = \sum_{i=1}^{N} b_i(Q) e^{i\mathbf{Q}\cdot\mathbf{r}_i(t)} \tag{4.3}$$

$$I(Q,t) = |E(Q,t)|^2. \tag{4.4}$$

The particles used in this study are fairly monodisperse (polydispersity $\leq 8\%$ [86] - see section 4.4.1); this property, in conjunction with time-averaging reduces equation 4.4 to

$$\langle I(Q)\rangle = N[b(0)]^2 P(Q) S(Q). \tag{4.5}$$

$P(Q)$ and $S(Q)$ are the form factor and structure factor respectively, and the $N[b(0)]^2$ gives the total scattered intensity at $Q = 0$ due to contributions from all N particles in the scattering volume. In a very dilute sample, the interparticle distance will typically be large compared to the particle radius; $S(Q) \rightarrow 1$. In this limit, the scattered radiation can be used to give a highly accurate measurement of the particle core radius via a measurement of the form factor:

$$P(Q) = \left[\frac{b(Q)}{b(0)}\right]^2 \tag{4.6}$$

after removal of the background. The form factor can be used to extract the particle radius, or more accurately, the value for r at which the step change in refractive index occurs. For a sphere of radius R,

$$P(Q) = \frac{9}{(QR)^6}\,(\mathrm{sin}QR - QR\,\cos\,QR)^2. \tag{4.7}$$

This equation is independent of n, as it only describes the form of the particle (the refractive index difference between particle and surrounding affects the relative amount of scattered power). Figure 4.2 shows the theoretical form for this measure, taking R as 1 (from equation 4.6 it can be seen that the function $P(Q)$ is dimensionless). The simplest way to empirically determine particle size is to use the minima in the form factor; these are found [87] at

$$QR = \tan\,QR \qquad\qquad = 4.49, 7.73, 10.90, ... \tag{4.8}$$

The data obtained (see section 4.5.1) were fitted using the theoretical form factor, and the polydispersity of the sample was estimated using the method of Fairhurst [87].

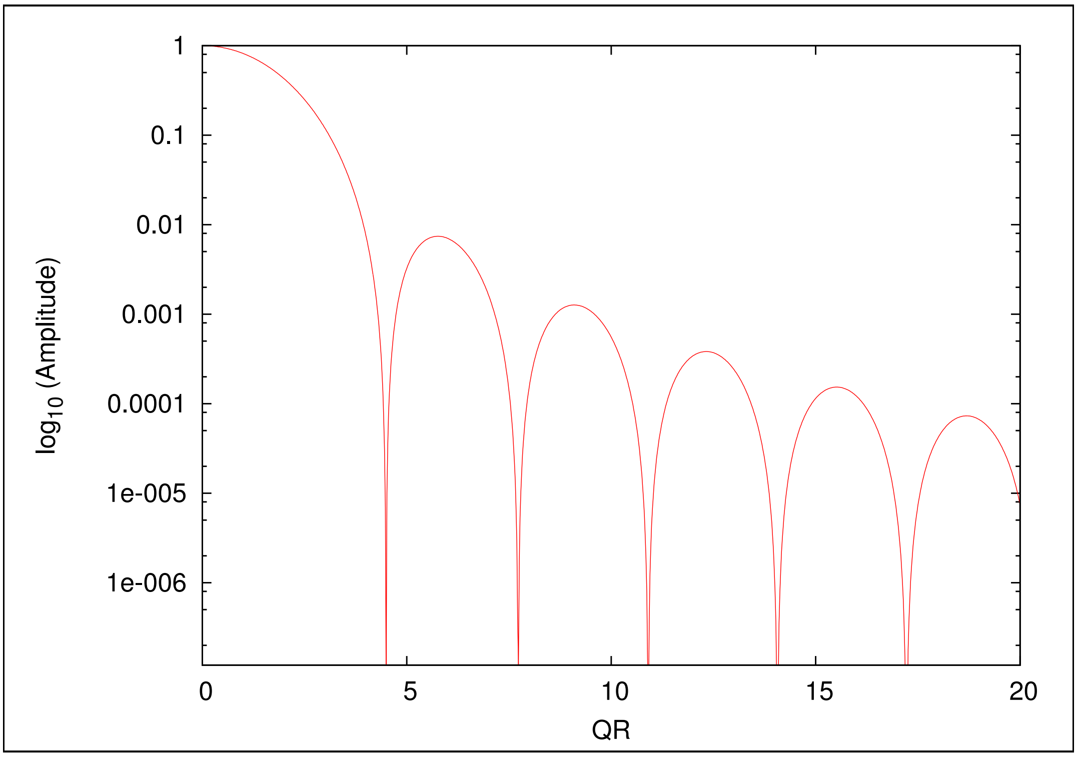

Figure 4.2: Theoretical form factor for a spherical particle.

4.1.2 Confocal microscopy

Confocal microscopy has become a ubiquitous tool in the study of colloidal structure and dynamics. Although no experiments using the technique were performed for this research, results obtained by others (e.g. [88]) lay some of the groundwork for the analysis here. The application of confocal microscopy to dense colloidal systems [89, 90] has allowed the tracking of tens of thousands of fluorescent particles with a time resolution of up to 1Hz. The real strength of confocal microscopy is that it is a real-space technique capable of quantifying the positions of individual particles to within around 40nm, in all three spatial dimensions. Although light scattering has a higher position resolution, it is inherently an ensemble average measurement, and gives little information about the evolution of locally heterogeneous structures. Confocal microscopy has allowed direct visualisation of the in-cage diffusion that occurs in dense colloidal systems [88]. Optical tweezers measurements are complementary to the microscopy in that they are capable of producing a much higher time-resolution (around four to six orders of magnitude higher sampling frequency [69]), but only for a single particle at a time.

4.2 Hard-sphere colloidal systems

4.2.1 Nature and properties

Although many exotic colloidal systems may be envisaged, the simplest to consider is a suspension of ‘hard’ spherical particles, which interact in a billiard ball-like fashion. Barring hydrodynamic interactions, the particles do not influence each other until they touch, whereupon they encounter an infinitely high repulsive barrier (also assuming that the particles do not deform when they collide). Experimentally, such a system can be realised by the combination of three distinct techniques: refractive index matching (to suppress van der Waals forces), the addition of a salt [91] to the solvent medium in order to mitigate the effect of residual charge on the colloidal particles (charge stabilisation), and the addition of polymer hairs (steric stabilisation). A layer of polymers anchored to the surface of the colloidal particles creates an exclusion zone of around 10nm from the core surface [85]. When the polymer halo of another colloidal particle approaches the exclusion zone, the hairs’ configuration space is restricted, giving a repulsive entropic force that pushes the approaching particle away. The experiments in this study use both methods to stabilise the colloidal suspension and ensure that the interparticle behaviour is as close to an ideal HS interaction as possible[2].

4.2.2 Phase behaviour and metastability

The phase behaviour of hard-sphere colloidal systems lends itself well to computer simulations, and such studies [92, 93, 94] have been shown to be in good agreement with experiment [95, 86]. A simple temperature/volume fraction phase diagram

---

[2] In experiments, this picture is not quite physically accurate, and the infinitely high repulsive barrier is not a step but a very steep slope - the colloids can be held to be ‘slightly soft’ [86].

(fig 4.3) may be constructed. The volume fractions $\phi_f = 49.4\%$ and $\phi_m = 54.5\%$ are notable as the lower and upper bounds of the fluid-crystal coexistence region (respectively the freezing and melting points). A long-lived metastable glassy state has been observed in samples with volume fractions greater than $\phi_g \approx 58\%$ but lower than the random close packing fraction of $\phi_{rcp} = 64\%$. This glassy phase is a non-ergodic state (i.e. distinct from fluid) but with no long range order (i.e. distinct from a crystal). Light scattering experiments [96] have shown that in a glass, a particle's Q-space time-autocorrelation function shows a number of specific features. At extremely short timescales, a particle undergoes ballistic motion; although this regime has been studied using optical tweezers [77], these dynamics are assumed to be far faster than anything studied here, an approximation which allowed us to drop the inertial term from the Langevin equation for particle motion in chapter 2. The solvent in which the particles are submerged behaves as a continuum, imparting Brownian motion; this gives the random driving force seen in the right-hand side of equation 2.11. In colloidal suspensions with volume fractions close to, but below the melting point ($\phi_m = 54.5\%$) the sample is ergodic, albeit with a lower diffusion constant than that in bare solvent [53] - this is equivalent to saying that the particle 'sees' a higher solvent viscosity. The position autocorrelation function for a particle in such a suspension decays with a characteristic time τ. Close to, but below the

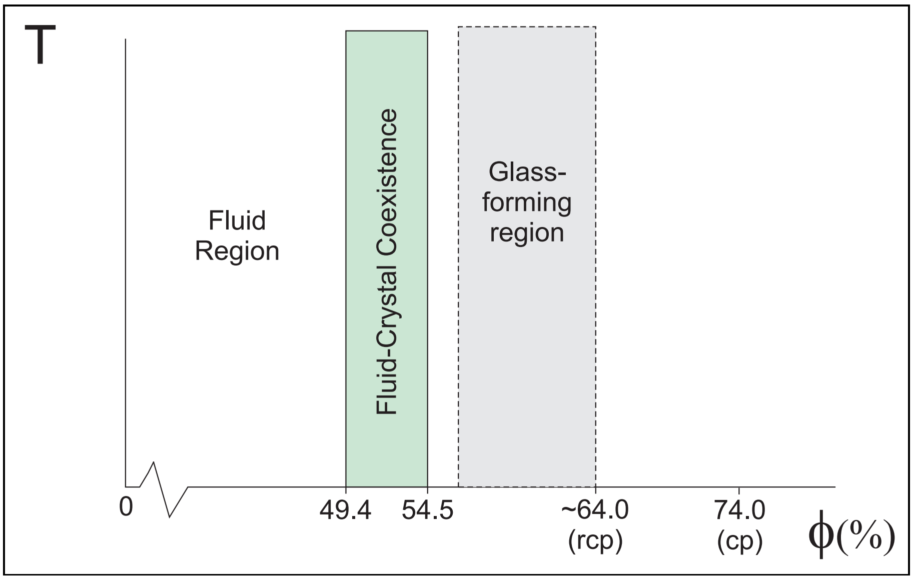

Figure 4.3: Hard-sphere system phase diagram.

glass transition ($\phi \approx 58\%$), the decay of the position autocorrelation function occurs on two distinct timescales, τ_α and τ_β (this is illustrated schematically in figure 4.4). The β timescale describes an in-cage diffusion, where the particle is coupled with its neighbours hydrodynamically, but otherwise acts as a freely diffusing particle in a medium of enhanced viscosity. This timescale is relevant for movements smaller than the average cage size, which is around 15% of the particle radius [97]. The particle's motion is then confined by the cage, causing the autocorrelation function to level off. The longer α timescale then corresponds to cage rearrangements, whereby the cage is significantly deformed or broken in an entropically-driven rearrangement process [98]; this is a longer timescale, which diverges quickly from the β timescale for volume fractions approaching the glass transition [99]. Above the glass transition, the particle's long-distance motion is arrested, and although there may be slight rearrangements, the shell of nearest neighbours around most particles does not change on experimental timescales. Furthermore, it has been shown that at extremely long times, the in-cage diffusion slows in a process known as colloidal ageing [100, 101]. This hints that there are slight cage rearrangements persisting even at these higher volume fractions.

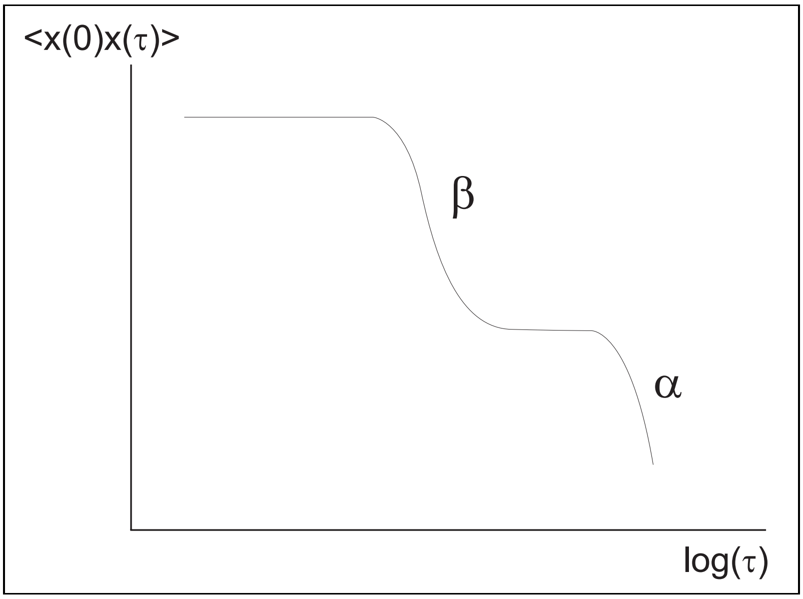

Figure 4.4: Schematic of the α and β timescales.

4.3 Rheology

Rheology is the study of deformation and flow. Rheometric studies have proved a useful tool for exploring the non-equilibrium behaviour of colloidal systems. A basic way to investigate the rheology of a system is to apply a constant shear strain (for example, a step strain function in time) and measure the stress response. In a simple (Newtonian) fluid, initial stress build-up relaxes and energy is dissipated in viscous heating of the fluid. For an ideal solid (in the linear response regime) the material deforms and stores energy, up to its elastic limit, where it deforms irreversibly. Most substances have a response which lies somewhere between these extremes, and their response is termed 'visco-elastic'. A substance's stress response, $\sigma(t)$, to a step shear strain function γ_0 (or equivalently a delta-function shear rate), is described by a time-dependent shear modulus $G(t)$

$$G(t) = \frac{\sigma(t)}{\gamma_0}, \tag{4.9}$$

in the long-time limit, $G(t)$ tends to zero for a liquid, and some finite value G_e for a solid. Similarly, the response to a step stress, σ_0, defines viscosity,

$$\eta(t) = \frac{\sigma_0}{\dot{\gamma}(t)}, \tag{4.10}$$

which becomes the more familiar steady-shear viscosity η_0 at long times in the case of a Newtonian liquid, but diverges in the case of an ideal solid. These properties are summarised in schematic form in figure 4.5. In fact, the behaviour of a real solid differs from the ideal case at large stresses. Beyond a certain stress (the 'yield stress') solids will deform irreversibly.

Another way to examine a system's response to shear is to use frequency domain methods; instead of applying a delta-function shear rate in time (a step strain), we apply a delta function shear frequency. This approach is useful from a practical point of view as it gives an accessible presentation of the shear modulus as a function of shear rate (high frequencies correspond to high shear rate). Probing a material's frequency response is relatively easy to achieve by applying a shear rate which varies sinusoidally in time,

$$\gamma(t) = Re(\gamma_0 e^{i\omega t}). \tag{4.11}$$

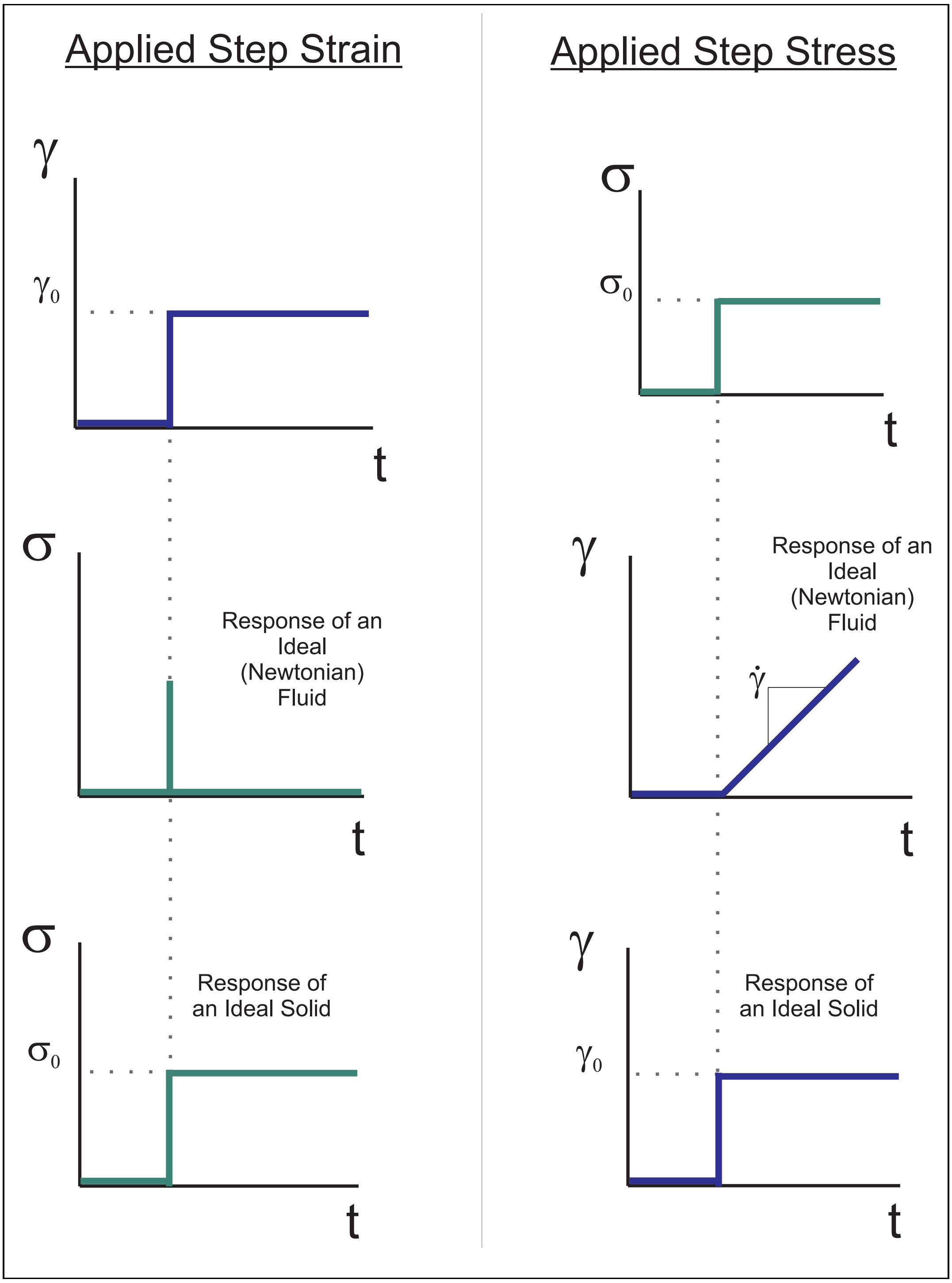
Applied Step Strain
Applied Step Stress
γ
γ₀
t
σ
σ₀
t
σ
Response of an Ideal (Newtonian) Fluid
t
γ
Response of an Ideal (Newtonian) Fluid
γ̇
t
σ
σ₀
Response of an Ideal Solid
t
γ
γ₀
Response of an Ideal Solid
t

Figure 4.5: The responses of an ideal liquid and an ideal solid to a step stress and a step strain.

The response function is then examined as a complex, frequency-dependent shear modulus, the frequency-domain equivalent of equation 4.9

$$\begin{aligned} G^*(\omega) &= i\omega \int_0^\infty G(t) e^{i\omega t} dt \\ &= G'(\omega) + iG''(\omega) \end{aligned} \tag{4.12}$$

where the real and imaginary parts represent the storage and loss parts of the response function respectively. The limiting cases of this function (an ideal Newtonian fluid and an ideal elastic solid, as before) are shown in equations 4.13 and 4.14,

Ideal fluid

$$G^*(\omega) = G''(\omega) = \omega\eta \tag{4.13}$$

Ideal solid

$$G^*(\omega) = G'(\omega) = G_{eq} \tag{4.14}$$

where G_{eq} is the equilibrium shear modulus, the energy per unit volume stored by the stressed material, the idea being that no energy is dissipated as heat in shearing an ideal solid.

4.3.1 Macrorheology

Macrorheology probes the mechanical response of a macroscopic quantity of a material. The results obtained are the 'bulk' response of a system to an external force; in the case of a colloidal system, the sample size is sufficiently large compared to the suspended particle size that it behaves as a continuous medium. Dense colloidal suspensions (with volume fractions above the melting point $\phi_m = 54.5\%$) are described as soft solids; although the equilibrium phase is a crystalline solid for a hard-sphere suspension at this volume fraction, flow can be induced with extremely small shear stresses, for example tilting the vessel in which the suspension is contained. This phenomenon is known as shear melting [102].

Hard-sphere colloidal solids below the glass transition - $49.4\% < \phi < 58\%$

At low strains and shear stresses the viscoelastic response is linear, that is to say that the storage and loss moduli are independent of applied strain, in the manner described in section 4.3. Several authors have performed macrorheological experiments in this regime, for example, references [103] and the low-strain range of measurements in reference [104]. To take the latter as an example, the authors studied a suspension of hard spheres with a radius of 0.21μm. They found that the sample's storage modulus, $G'(\omega)$ dominates the complex response function for all but the lowest volume fractions (i.e. $\phi < 52\%$), and both loss and storage moduli tend toward frequency independence for the low-frequency range at volume fractions close to the glass transition. In the opposite (high-frequency) limit, the viscosity dominates, tending to a constant value, η_∞. This is closely related to a quantity central to the analysis presented in this thesis, the short-time self-diffusion coefficient, defined as

$$D_s^s = \frac{k_B T}{6\pi\eta_\infty a}, \tag{4.15}$$

which describes the diffusion of a particle at short timescales.

At higher strains, non-linear behaviour is observed [105]. The loss modulus remains approximately constant as a function of strain, whereas the storage modulus falls away rapidly beyond a certain critical strain, γ_c. This critical value corresponds to the strain required to rearrange a cage of particles; when a cage is sheared beyond a certain limit, the identities of its constituent particles change. This means that there is an upper limit to the amount of stress that can be recovered after shear, and this is set by γ_c.

I describe shear rates here in terms of the Péclet number, which is given by $\mathrm{Pe} = \tau_B/\tau_{\dot\gamma}$, where τ_B is the time a particle takes to diffuse a distance of its own radius in the absence of host particles, and $\tau_{\dot\gamma}$ is the time taken to actively separate two particles by the same distance by mechanical shearing. Written out more fully, this quantity is given by

$$\mathrm{Pe} = \dot\gamma a^2/2D_0, \tag{4.16}$$

where $\dot\gamma$ is the shear rate, a is the particle radius and D_0 is the diffusion coefficient in bare solvent. At the lowest Péclet numbers, a Newtonian viscosity is observed, which then gives way to shear thinning behaviour (viscosity *decreases* as shear rate *increases*); this is because as shear rate is increased, $\tau_{\dot{\gamma}}$ becomes short compared to the Brownian time, so Brownian relaxations do not occur fast enough to compensate for the shearing action. This shear-thinning behaviour is limited by the increasing importance of hydrodynamic interactions which at first lead to a second Newtonian plateau in viscosity, and finally to shear thickening at the highest shear rates [106, 107].

Hard-sphere colloidal glasses - $58\% < \phi < 64\%$

Broadly speaking, the behaviour of a colloidal glass at low shear rates and stresses is like that of a solid, with a dominant, frequency-independent storage modulus (see equation 4.14) [104]. This solid-like behaviour is attributed to 'cage elasticity' in [54], where an individual particle's cage of neighbours deforms but does not break. There is a caveat to this assertion, however, as 'creeping' behaviour occurs at the very lowest shear rates [108], and step shear experiments [109]. Creep behaviour is characterised by the recovery of strain in a very slow process driven by Brownian motion. The viscosity of a glassy sample only truly diverges (implying true solid behaviour) at $\dot{\gamma} = 0$. At finite shear rates and strains, shear melting causes the suspension to act like a highly viscous fluid, with a high-frequency viscosity that diverges as the volume fraction approaches $\phi_{RCP} \approx 64\%$ [110, 111, 112]. After shear melting, crystallization may occur [113]. Finally, a clearly-defined yield stress emerges on approaching the colloidal glass transition. This occurs where the loss modulus becomes dominant over the storage modulus, and is characterised by an irreversible deformation. The strain required to achieve this is around 15% [109] (cf. the cage size reported in [97]).

4.3.2 Microrheology

Microrheology is the microscopic counterpart to conventional (macro-) rheology. Instead of examining the bulk properties of a suspension, the stress/strain response is examined on a much smaller lengthscale, using probes that are typically in the micrometre size range. Glassy colloidal laponite systems have been examined using passive microrheology [48, 49], to investigate their aging behaviour by examining the modified Brownian fluctuations of a trapped particle in a suspension, and observing how this changes over time. The transition from fluid-like behaviour to glassy behaviour is seen as a drastic reduction in the trapped particle's mean-squared displacement, and an increase in the high-frequency viscosity.

Active microrheological measurements have also been made on colloidal systems, exploring both the linear [49] and nonlinear [8, 114, 115] regimes. In the linear regime, it has been shown that active microrheology results in F-Actin solutions match both passive microrheological measurements and bulk rheology. Two different approaches are adopted in the above references for nonlinear rheology; constant velocity and constant force approaches. If a microscopic particle is trapped and pulled through a suspension, it may be moved either with constant force (and thereby variable velocity) of constant velocity (and therefore variable force).

Reference [114] is a study which used magnetic tweezers as a constant force probe of a hard-sphere colloidal suspension. Forces in the range 0.1-10pN were applied to magnetic beads (radius 2.25μm) which were embedded in a suspension of particles approximately half their radius. Average yield forces for cages of nearest neighbours were extracted, with values of around 0.5pN for volume fractions around $\phi = 52 - 56\%$. Interestingly, the yield force appears to be independent of volume fraction in this range. The second reference listed above, [8], used a constant velocity setup, much like the one in this study. Probe particles with radii 0.5μm, 1.4μm and 1.6μm were used in suspensions of particles that were significantly smaller, of order 80nm. The concentrations investigated here were all below the freezing volume fraction, the densest suspension having $\phi = 31\%$. The results obtained were broadly in line with bulk rheology of complex fluids in the Newtonian regime, except for the smallest probe size at the highest speed, which exhibits some shear thinning.

4.4 Colloidal sample preparation and characterisation

4.4.1 Stock sample preparation

The (PMMA) particles used in this study were synthesised by Dr. Andrew Schofield according to standard preparation methods, dyed with fluorescein (to allow the possibility of later confocal microscopy studies) and sterically stabilised using PHSA 'hairs'. The fact that the particles crystallise (albeit slowly, on a timescale of days) puts an upper bound of 11% on the polydispersity [23], and this is confirmed by static light scattering measurements, which also allow for a measurement of the particle core radius. The particles were initially produced in the solvent dodecane, which has an inappropriate refractive index and density for this study. Although the index of bulk PMMA is known, there are complications arising from using such small particles; firstly, there is an amount of swelling due to the particles' slight absorption of the solvent they are suspended in. This results in a variation of the refractive index of the particle across its diameter, and it is strictly this form factor that is measured in static light scattering studies. The ideal particles for this optical tweezers study are refractive index-matched with the solvent they are suspended in, and neutrally buoyant. In the general case, this is achieved by using a mixture of three solvents, but as will be discussed later, a two-component mixture was found to give satisfactory results.

The initial batch of particles was transferred from being suspended in dodecane to being suspended in a mixture of cis- and trans-decalin ('decalin' is the trade name of decahydronaphthalene). To achieve this, the particles were placed in a centrifuge (the densities both of dodecane and decalin are lower than that of the PMMA particles), and when a sediment had formed, the supernatent was discarded. The vessel containing the sample was then re-filled with decalin and the close-packed sediment re-dispersed. After each wash cycle, the supernatent fluid was examined in an Abbe refractometer and compared to a control sample of decalin; after seven washes, the refractive indices were the same to within the error of the instrument (±0.0003).

In order to make the particles neutrally buoyant, the solvent was modified by adding measured volumes of cyclohexylbromide (CHB), which is known to have a higher density than PMMA. The particles in the new solvent were re-dispersed and then spun in a temperature-controlled centrifuge; if a sediment or cream formed, the appropriate solvent was added and the centrifuge repeated until the particles remained in suspension for at least 48 hours at 5000rpm.

The refractive indices of the component solvents were measured using a white-light Abbe refractometer at 22°C and found to be $n_{CHB} = 1.504$ and $n_{deca} = 1.472$, placed either side of the literature value for bulk PMMA (at the Sodium D line) $n_{PMMA} = 1.49$. As has been previously mentioned, the concept of refractive index matching is a somewhat tenuous one because the particles are not entirely homogeneous due to solvent absorption near their surfaces as well as inherent inhomogeneities in the PMMA superstructure. Calculations by Tlusty et. al.[55] outlined in chapter 2 have shown that the trapping force is directly proportional to a constant α, defined by

$$\alpha = \frac{n_p^2}{n_s^2} - 1 \tag{4.17}$$

As the relative permeability μ_r of the particles used is close to one, the approximation $n \approx \sqrt{\varepsilon_s}$, where ε_s is the dielectric constant of the solvent may be made. The trapping (and hence sensing) volume of the optical tweezers is highly localised by use of a high numerical aperture objective (see chapter 3), with the e^{-1} intensity point being smaller than a particle diameter in all axes. This, coupled with the low refractive index difference between colloidal host and solvent medium minimises the chance of the laser influencing the movement of the host particles. Measurements of solvent refractive index were made on either side of the density matching composition (i.e. using one sample in which the particles form a sediment under centrifuge, and another where they cream) and no difference was found down to the third decimal place. Based on this, the more sensitive criterion of density matching was chosen as the critical solvent composition property.

Tracer particles made of melamine resin (which has a bulk refractive index of 1.7) were obtained[3], and were sterically stabilised by Dr. Andrew Schofield in the same manner as the PMMA. The particles were then dried in a vacuum oven, and re-dispersed in supernatent obtained from the density-matched samples. The resulting suspension is one of density- and near-index-matched particles, with sparsely distributed high-index tracer particles to be used as handles by the optical tweezers. The tracer particles were already characterised by the vendor using scanning electron microscopy, and were found to have a radius of 0.95μm and a polydispersity of 4.7%. The treatment of the tracers is also simplified by their remarkable level of chemical inertness; they are impermeable to most organic solvents (including the substances used here) and are reported to be damaged only by hot sulphuric acid ([116]).

---

[3] From Microparticles GmbH.

4.5 Characterisation of stock

A dilute suspension of PMMA particles was characterised using static light scattering, to obtain values for the average core radius (the PHSA hairs with which the PMMA was coated add approximately 10nm to this value[4]). The sample was diluted to around $\phi \approx 0.01$ for the light scattering experiments which operate in the single-scattering limit.

4.5.1 Light scattering

A Krypton-ion laser operating at the 647nm line was used to probe the small-angle Q-vectors which yield information on the form factor of the particles (see fig.4.6). A dilute suspension of PMMA particles in a 80%/20% mixture of CHB/Decalin (an early iteration of the density-matching solvent) was used as a scattering target. The solvent composition was chosen because it is close to refractive index matching, which is required for the single-scattering regime. The sample temperature was controlled using a heat bath; this provided a way of varying the refractive index contrast between the particles and medium, as the solvent refractive index depends on temperature more strongly than that of the particles. Initially, a background measurement was made on a scattering target containing only the solvent medium, to record the scattering from elsewhere in the system. Experiments were then performed at 20°C and 17°C on target containing PMMA particles, from which the background level was subtracted. The results are presented below in figure 4.6. The form factor was fitted, and a value for the particle core radius of 860nm±70nm was obtained.

---

[4] Although the PHSA does have an inherent polydispersity in polymer chain length, it is dwarfed by the uncertainty in particle size and is thus ignored herein.

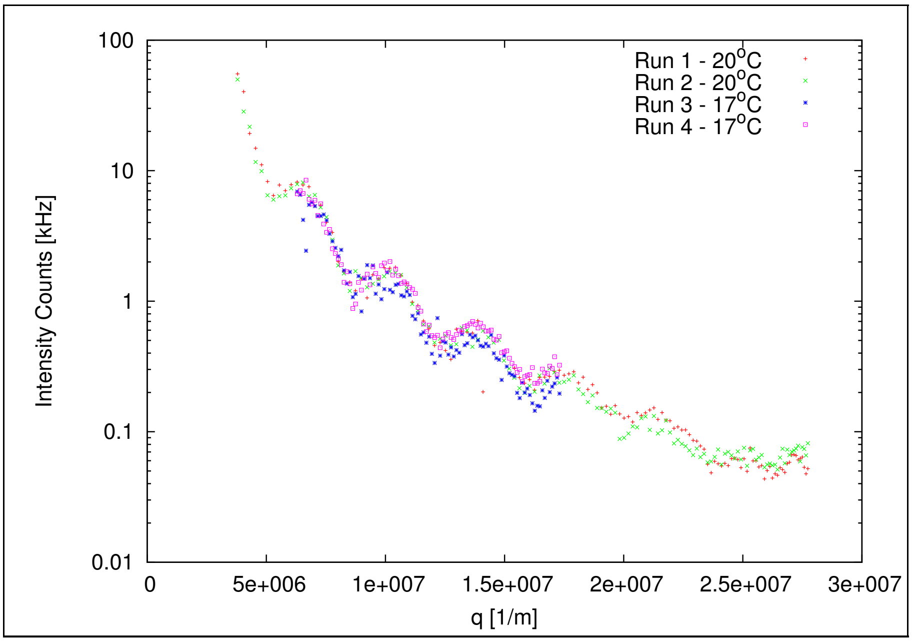

Figure 4.6: Light scattering results.

4.5.2 Characterisation of suspension medium

An accurate knowledge of the physical properties of the solvent medium is essential to this study. The key property of dynamic viscosity must be measured to a high precision in order to extract meaningful data from our experiment; this was achieved using a commercial rheometer and a conventional concentric-cylinder geometry. The rheometer was driven using a set shear rate, so the dynamic viscosity could be extracted; several runs at different temperatures were performed, and a graph of the measured viscosity is given in figure 4.7. The figure shows some noise at the lowest shear rates, this is due to the mechanical limitations of the rheometer. The viscosity was obtained by fitting a straight line of constant viscosity to the data series at shear stresses ≥ 0.06 Pa. The medium behaved as a Newtonian fluid (as expected) at all shear rates examined, and the value for solvent viscosity at lab temperature was found to be 2.56×10^{-3} Pa·s.

4.6 Preparation of individual samples

Samples of different volume fraction were produced for the main experiments. In order to do this, the stock density matched sample was subjected to centrifuge

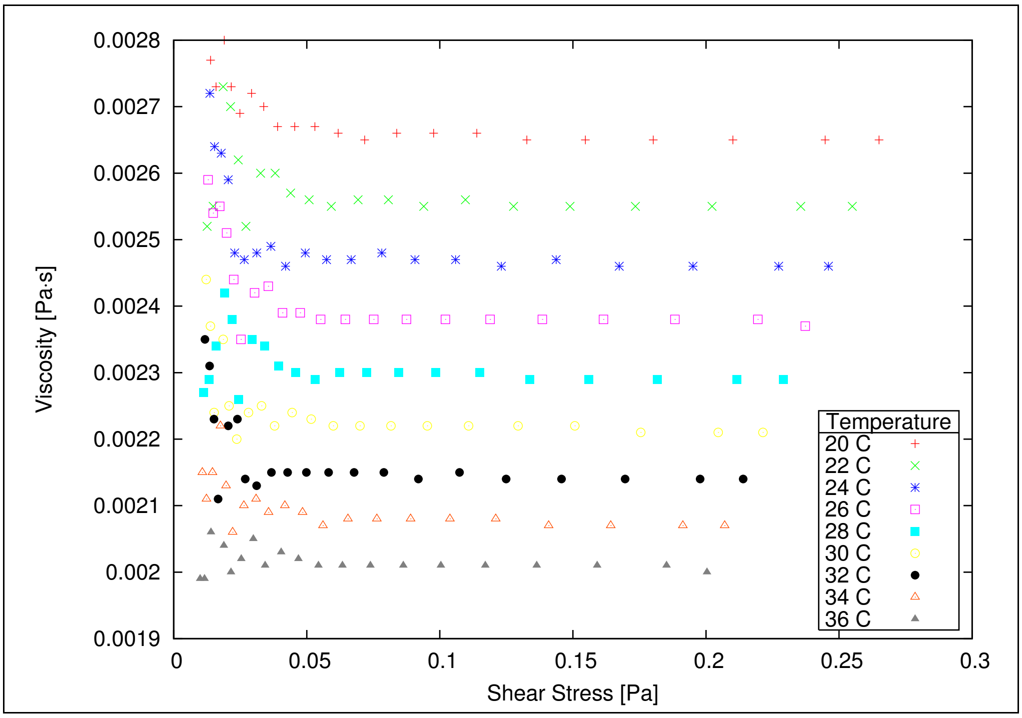

Figure 4.7: Rheological measurements of solvent viscosity as a function of temperature.

at around 30°C to obtain a close packed sediment (the sample is only density-matched at room temperature) and supernatent fluid, which was decanted. The sediment is taken to have a volume fraction of $\phi = 64\%$. The decanted supernatent fluid was filtered to remove any extraneous particles, and then added back to small amounts of the sediment in separate jars, in order to produce the various volume fractions required. The samples were all stored with one of the longest side walls of the chamber pointing downward; this way, the tracers (which are heavier than the host colloid) fall to this side, and are more easily located.

4.6.1 Sample cells

Two different types of sample cell were used, one for samples with volume fraction below the freezing point ($\phi_f = 49.4\%$), the other for higher volume fractions. This decision was motivated by the work of Mark Haw [52] who showed that jamming effects lead to unreliable transferral of high volume fraction samples: when using a syringe to transfer sample matter, particles jam easily in narrow needle openings, meaning that solvent is drawn through a jammed arrangement of particles and into the syringe, giving a lower-than-expected final volume fraction. This was avoided by using a thick sample chamber with a wide opening, composed of two microscope coverslips glued to form a bridge across the gap between two 1mm-thick sections of glass slide. One end of the sample chamber was sealed using UV-curing glue, and the other left partially open (see figure 4.8). A spatula was used to transfer the denser samples into the chamber, which was then plugged with a third piece of glass slide and sealed with epoxy resin. A range of different volume fractions were produced ($\phi = 40 - 62\%$), along with a sample cell containing only the supernatent fluid, which was used for calibration of the optical trap. Small pieces (around 1mm in length) of iron wire were placed in the higher-volume samples before sealing; these could be moved around using a strong magnet in order to break up crystallites that may have formed in the glassy samples.

The second type of cell (figure 4.9) was made for use with the sub-glassy samples. Using a standard microscope slide as a base, a coverslip cut into three sections was used to make the walls of two thin capillaries, which were glued into place. A second coverslip was glued on top of this and the ends of the cell partially sealed with UV curing glue, giving a sample chamber with a height of around 200μm. The cell chambers were filled by capillary action (the sample volume fractions here are too low to be affected by the self-filtration phenomenon) from a drop of sample on a separate slide, one chamber with the colloidal suspension, and the other with the density-matching solvent with tracer particles but no host (for calibration measurements). The ends of the cell sealed with epoxy resin. This type of sample cell was used so that the calibration and measurement procedures could both be done without having to change the sample on the stage. The incorporation of a small air bubble into these samples is useful as it may be used to break up crystallites in the way that the wire was used in the higher volume fraction samples.

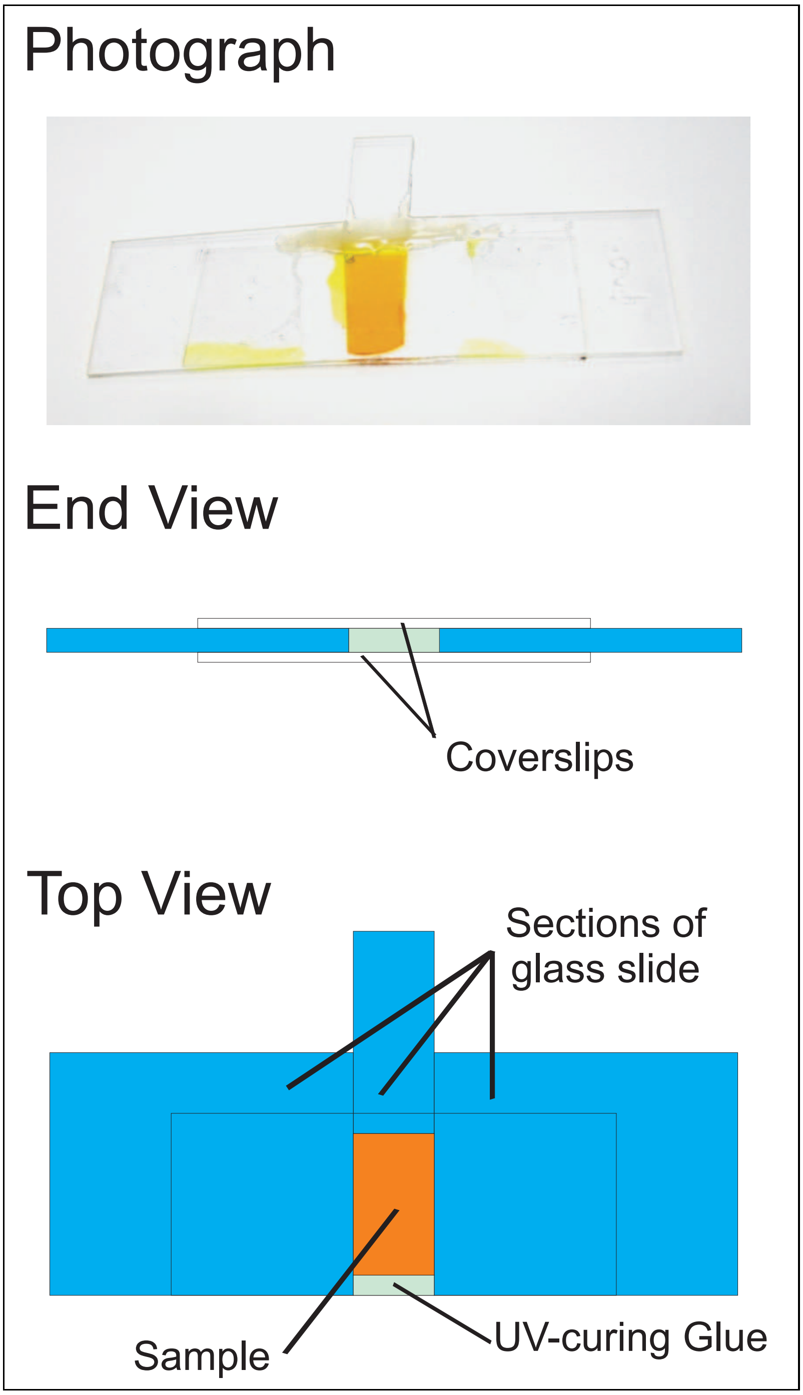
Photograph

End View

Top View

Coverslips
Sections of glass slide
Sample
UV-curing Glue

Figure 4.8: Sample holder for high volume fractions.

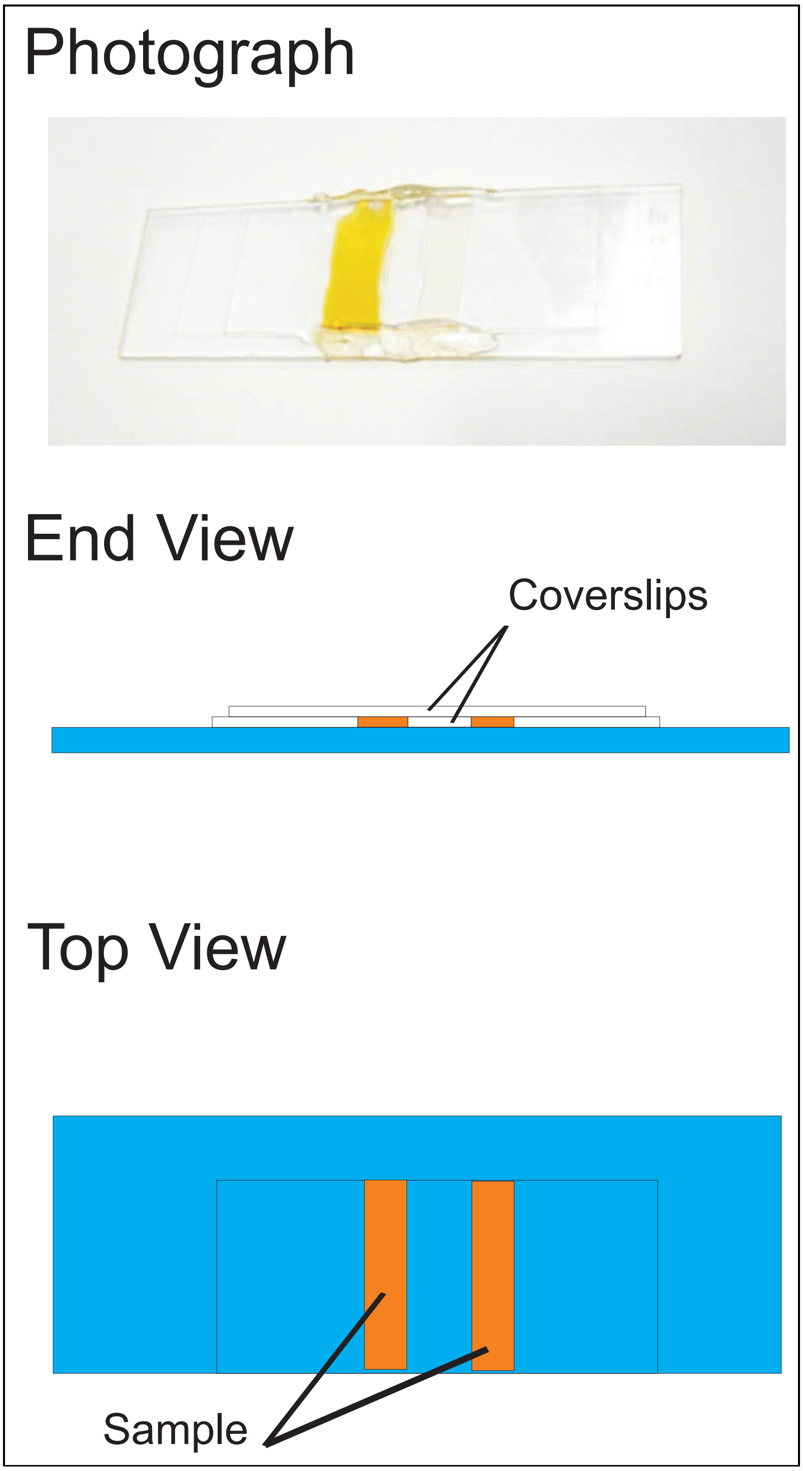

Photograph

End View

Top View

Coverslips
Sample

Figure 4.9: Sample holder for low volume fractions.

Chapter 5

Static Measurements in Dense Colloidal Suspensions

This chapter reports my measurements of the short-time self-diffusion coefficient (D_s^s) in dense suspensions, and the dynamic fluctuations in cages of particles as perceived by a caged particle. In summary, my measurements of D_s^s for $\phi \leq 58\%$ match well with existing light-scattering data from van Megen and co-workers [117]. In the glassy samples, however, D_s^s depends strongly on local history. If a tracer is moved to a different position in the sample, stresses incurred in the process take a relatively long time to relax, giving rise to a time-dependent D_s^s. This is shown by a much greater spread in the diffusion coefficient data at volume fractions above the glass transition, $\phi_g \approx 58\%$.

The second half of this chapter contains two-dimensional histograms and time series of recordings of probe particle position in samples both above and below ϕ_g. Whereas confocal microscopy studies conducted previously [88, 97] have already shown particles diffusing within their cages, these measurements are limited both by position resolution (±50nm) and time resolution (around 100Hz sampling rate). My measurements show that there are two distinct cage lengthscales emerging; a smaller 'microcage' size not resolved before, and a larger 'dynamic' cage size seen in dynamic light scattering and confocal microscopy. Measurements here also show the finite relaxation time of stresses in samples close to ϕ_g, corresponding to rearrangements in the local structure. At the highest volume fraction studied ($\phi = 62\%$), some cages persist for longer than the experimental timescale even in the presence of an optical force of up to 1pN, which indicates a finite yield stress.

5.1 Power spectrum analysis in dense colloidal samples

5.1.1 D_s^s on approach to the glass transition, $\phi = 54 \rightarrow 57\%$

Values for the short-time self-diffusion coefficient were obtained by fitting a straight line to the high-frequency portion of the power spectra on a log-log graph, and comparing the intercept on the vertical axis with that from the bare solvent case. Measurements were carried out on colloidal suspensions with volume fractions approaching the glass transition ($\phi_g \approx 58\%$). It was suspected that the density may vary slightly between different regions of the sample, especially given the manner in which it was agitated before the measurements were made[1]. As a result, the sample stage was translated between sample runs so that a few sample locations may be examined, and an average obtained for D_s^s/D_0. Initially, a probe particle was located (usually at the bottom of the sample cell, as the tracers are heavier than the solvent medium), trapped, and raised a distance of 20μm into the sample, to minimise the effects of the cell wall. The setup was allowed to equilibrate for around an hour before the first measurement, and then a recording was taken. Between subsequent runs, the particle was moved to a different location in the sample, and allowed to rest for about five minutes after being moved, to allow the surrounding suspension some time to relax. In the literature on bulk glassy rheology, this equilibration period is simply referred to as the waiting time, t_w, and this terminology is adopted herein.

The results in figures 5.1, 5.2 and 5.3 give values for the short-time self-diffusion coefficient in good agreement with existing data in reference [53], and have a similar experimental spread. The samples with $\phi_m < \phi < \phi_g$ are susceptible to crystallisation on experimentally accessible timescales[2], which would give erroneous results for D_s^s. Samples with volume fractions in this range have been left standing in order to observe crystallisation, which was found to occur on a timescale of around a month for all volume fractions below ϕ_g studied here.

---

[1] As previously mentioned in the sample preparation section, the samples were stirred using a magnet and a small piece of wire prior to loading, to break up crystallites.

[2] Reference [96] suggests crystallisation times of <10 minutes for $a = 201$nm particles with a polydispersity around 4%, significantly lower than in our system.

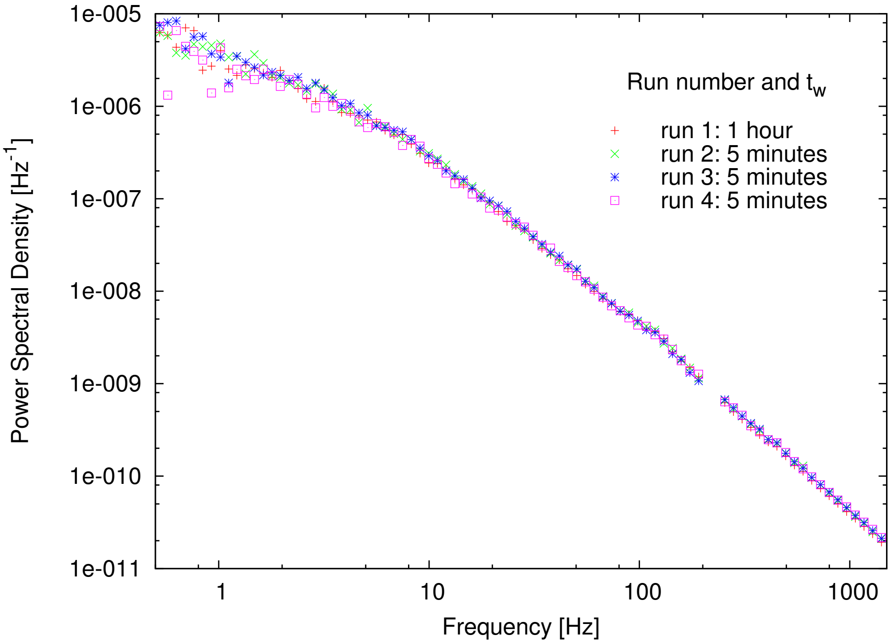

Figure 5.1: Power spectra for tracer motion in a $\phi = 54\%$ suspension, mean $D_s^s/D_0 = 0.119$, compared to the literature value mean 0.12.

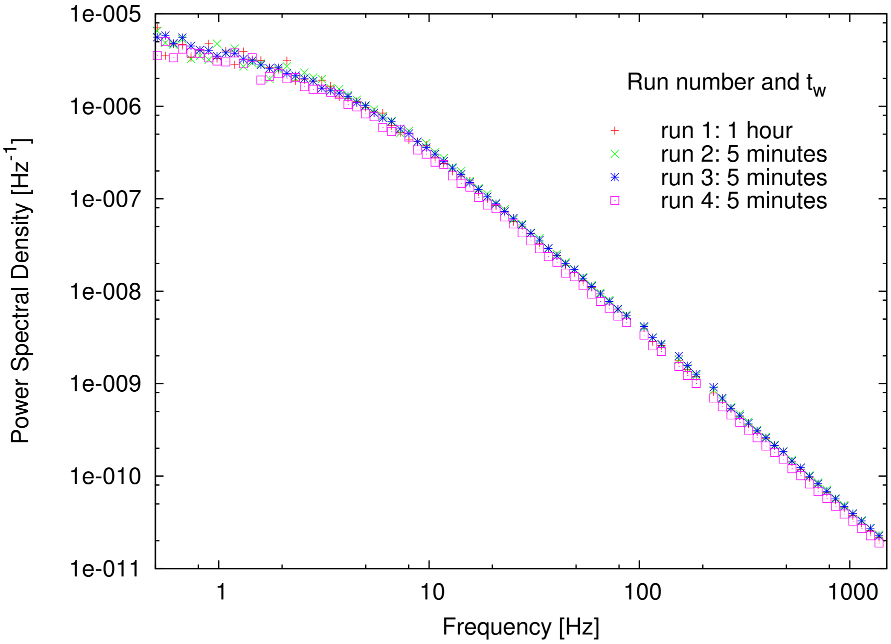

Figure 5.2: Power spectra for tracer motion in a $\phi = 56\%$ suspension, mean $D_s^s/D_0 = 0.112$, compared to the literature value mean 0.106.

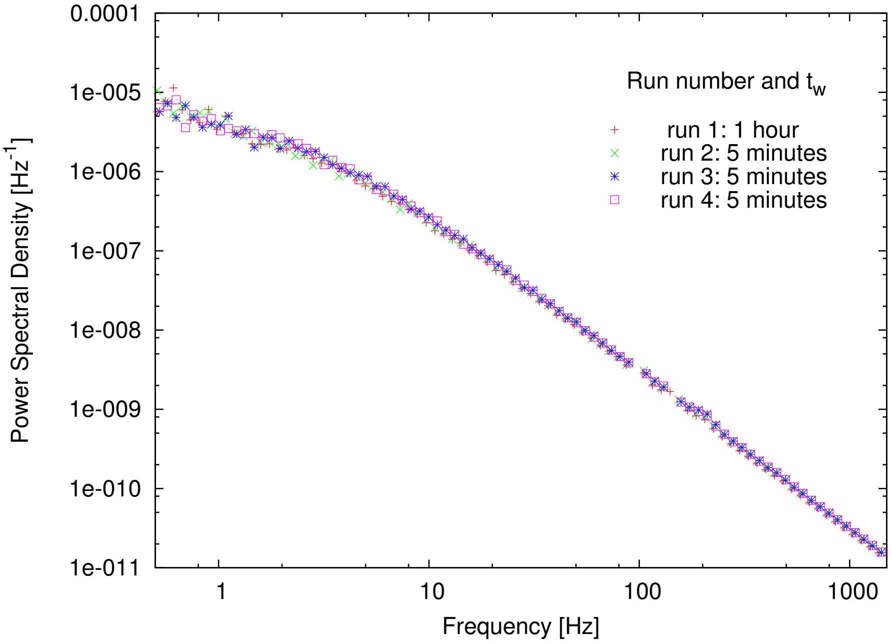

Figure 5.3: Power spectra for tracer motion in a $\phi = 57\%$ suspension, mean $D_s^s/D_0 = 0.081$ compared with the literature value mean 0.09.

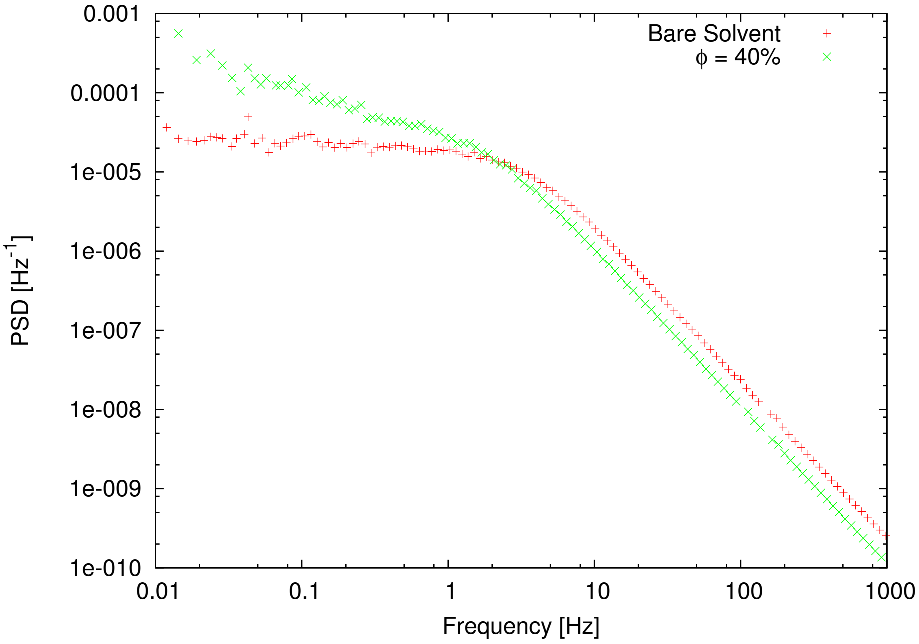

Figure 5.4: Power spectra for tracer motion in a $\phi = 40\%$ suspension compared to a power spectrum from a bare solvent measurement. $D_s^s/D_0 = 0.290$ in the sample with colloidal host, compared to the literature value 0.30.

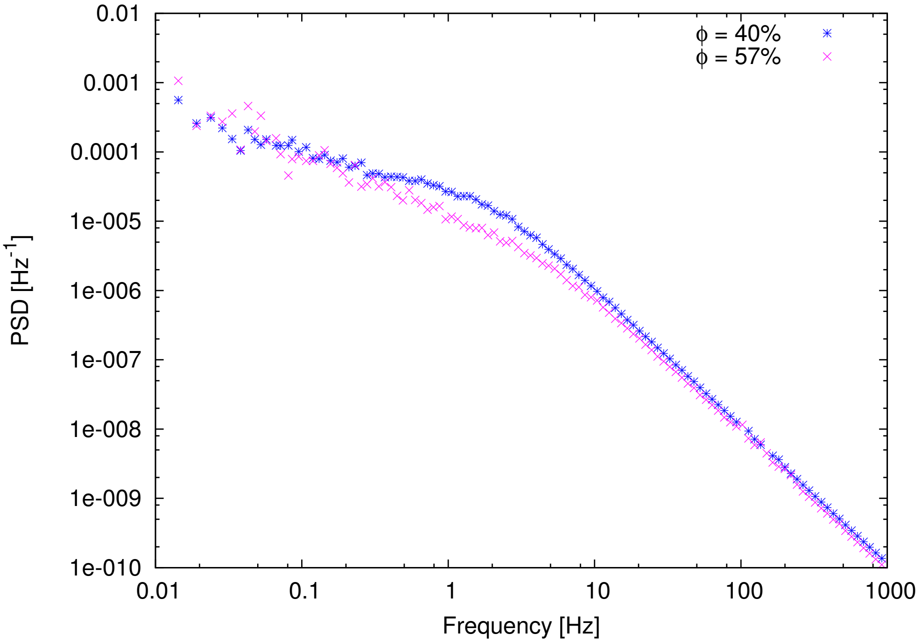

Figure 5.5: Comparison of a power spectrum obtained from a 40% suspension with one from a 57% sample. The 40% sample shows a larger amplitude at high frequencies (hence lower viscosity), and flatter low-frequency behaviour.

The fact that our results agree well with light scattering data obtained from metastable fluids also suggests that sample crystallisation has been avoided; to this end, a final measurement was made at 40% (below the freezing-point volume fraction, $\phi_f = 49.4\%$). At this volume fraction, a hard-sphere suspension behaves as a fluid, thus eliminating the risk of sample crystallisation. The results of the experiment on the $\phi = 40\%$ sample (presented in figures 5.4 and 5.5), are found to affirm this method of measuring D_s^s. The results are also compared both to a bare solvent measurement (figure 5.4) and to a $\phi = 57\%$ data set (figure 5.5). These graphs serve to illustrate the three noticeable changes apparent upon the introduction of host particles into the medium, and these features become more pronounced with increasing volume fraction: A lowering of the relative power at high frequencies, a shift in the corner frequency, and a non-uniform increase in the power at low frequencies. The first and second phenomena may be explained by an increase in the effective viscosity, due to the presence of the host particles. Over very short timescales, a particle's cage of nearest neighbours is essentially static, and the only interaction is hydrodynamic; denser samples have smaller cages and hence show stronger hydrodynamic coupling between particles.

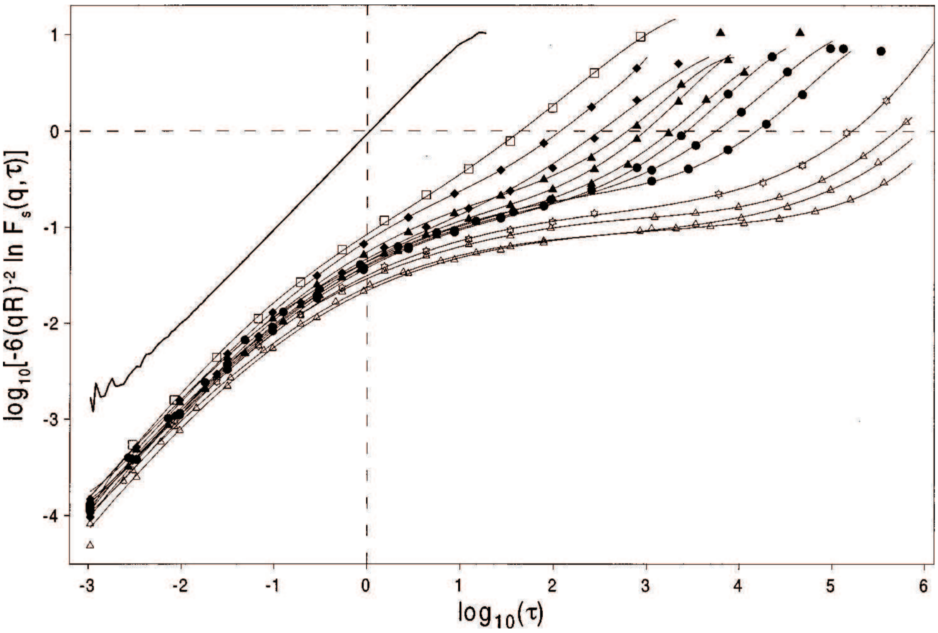

Figure 5.6: A reproduction of figure 7 from reference [53]. This graph shows the evolution of particle mean-squared displacements in samples with 13 volume fractions ranging from $\phi = 46.6\% \rightarrow 58.3\%$ from left-most to right-most data. The thick line at the left hand side describes the motion of a freely diffusing particle in bare solvent. The horizontal axis is measured in units of Brownian time (the time taken for a particle to diffuse its own radius in bare solvent) and the vertical axis shows distance (normalised by particle radius) squared.

The increase in the low-frequency part of the spectrum is due to fluctuations in the position of the probe particle's neighbours in the suspension, which occur on timescales of a few seconds. This may be thought of as a dynamic 'cage exploration time', where the exact shape of a particle's cage fluctuates and the volume available for exploration is greater than the static cage (short-time) case. Figure 5.6 shows data from light-scattering studies [53] which support this idea. The horizontal axis is measured in units of the Brownian time (the time taken to diffuse one particle radius in bare solvent). The vertical axis gives the mean-squared displacement in units of the particle radius squared, hence the graph for the bare solvent case, the thick solid line, has a gradient of unity. The mean squared displacements do not *strictly* plateau after the initial, diffusive cage exploration phase (below $\log(0)\tau_B$). Instead, they increase as the cage shape fluctuates slightly; this effect is explored in more detail in section 5.2.

The final graph in this section, figure 5.7, shows a summary of my measure-

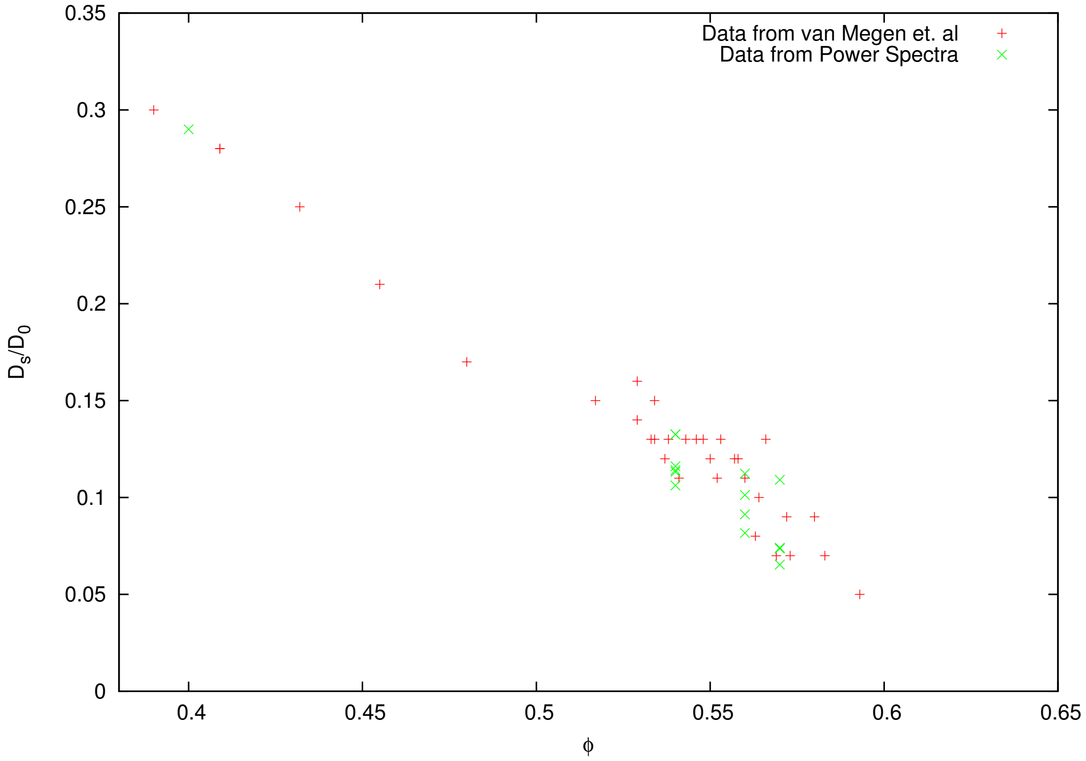

Figure 5.7: A summary of the measurements from this section. Red crosses represent light-scattering measurements performed by van Megen et al., and green crosses reflect values obtained by fitting straight lines to the high-frequency data in figures 5.1 - 5.4.

ments of D_s^s. The value of the data points in the figure is not correlated with the order in which measurements were made[3], for example, there is no evidence of a time-dependent short-time self-diffusion coefficient (which may imply aging behaviour). Similarly, by virtue of the translation of the probe particle between measurements, there appears to be no strong variation of this quantity between different places in the sample.

5.1.2 D_s^s at and above the glass transition, $\phi = 58\%, 62\%$

The power spectrum results at $\phi = 58\%$ (figure 5.8) show a departure from the previous results - the spread in D_s^s extracted from the power spectra is significantly greater than that between experimental runs in lower volume fractions. Moreover, this spread is related to the waiting time, t_w. The particle was moved within the sample and allowed to relax for an hour (as in previous experiments) before run 1. Again, like previous experiments, the particle was moved within the sample for runs 2-4. Run 5 was conducted the following day. As mentioned in chapter 4, in samples with volume fractions below ϕ_g, the sample is ergodic; the particles will diffuse around the whole sample volume, subject to a long-time diffusion constant D_l, which decreases to zero at the glass transition [118]. Specifically, the approach to the glass transition is marked by the emergence of the distinct α and β timescales which describe the long- and short-time (in-cage) diffusion respectively. Although it is not measured directly, these data suggest that there is some relaxation timescale lying between fifteen minutes (five minutes rest time plus ten minutes recording) and one hour; the data in reference [96] would seem to suggest that this is plausibly the α timescale[4]. The short-time diffusion coefficient measured from the first and last runs is in good agreement with the published value.

---

[3] The ordering of the measurements has been excluded from the figure in the interests of clarity.

Figure 5.9 shows data from a $\phi = 62\%$ suspension; as in the previous figure, the measurements in figure 5.9 were spread over two days. Runs 1-3 were conducted in succession, with a waiting time of an hour before run 1, then 5 minutes before runs 2 and 3. Runs 4-7 were conducted the following day, using a low laser power to centre the particle in the optical trap (the laser beam was used as a position sensor only, as the trapping force is so weak[5]), before the power was raised to the typical experimental level of 35mW in the BFP. The particle was *not* translated between runs 4 and 7; however, the trap stiffness was varied, which is why there is a greater spread in data at low frequencies. Runs 4-7 are in order of increasing trap stiffness. Here, whether the waiting time was one hour or five minutes seems to make little difference, although when the particle was left stationary in a sample overnight, the diffusion coefficient drops substantially. The behaviour in figure 5.9 is characteristic of a glassy sample (although a thorough investigation of whether this long-time relaxation is ageing behaviour [101, 48, 49] is beyond the scope of this study); furthermore, the short-

---

[4] This paper gives the α time at around 100 seconds for particles of radius $a = 205$nm in a $\phi = 57.4\%$ sample; this would equate to around 73 minutes if our larger particles and more viscous solvent were used.

[5] This principle has been used before, for example in reference [119], where the optical layout contains two different beams, one at low power for position sensing and one at a high power for trapping.

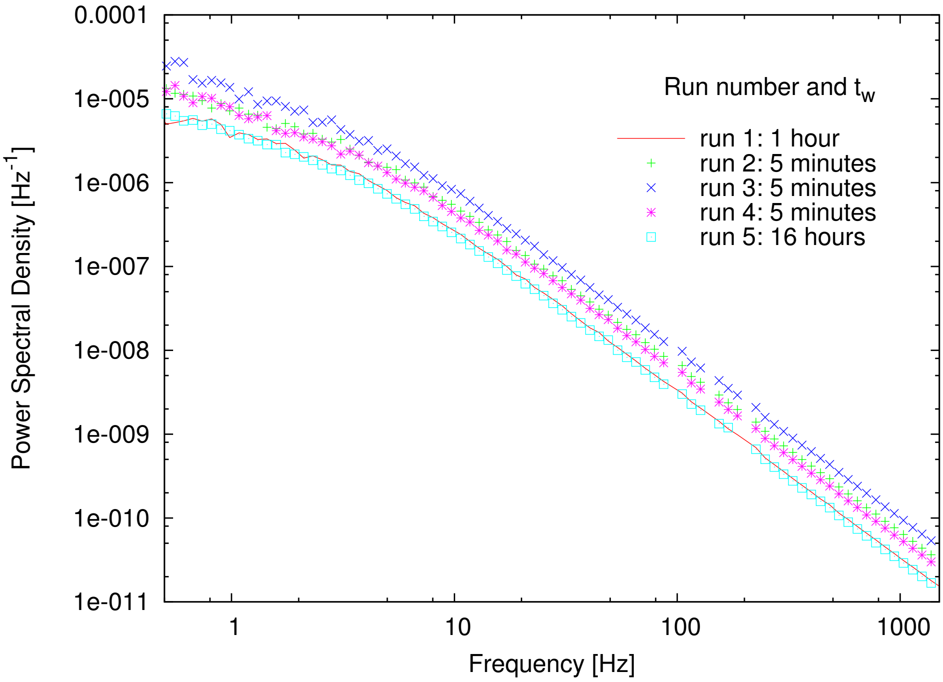

Figure 5.8: Power spectra for tracer motion in a $\phi = 58\%$ suspension, mean $D_s^s/D_0 = 0.0952$ for runs 1 and 5, compared with the literature value mean 0.094.

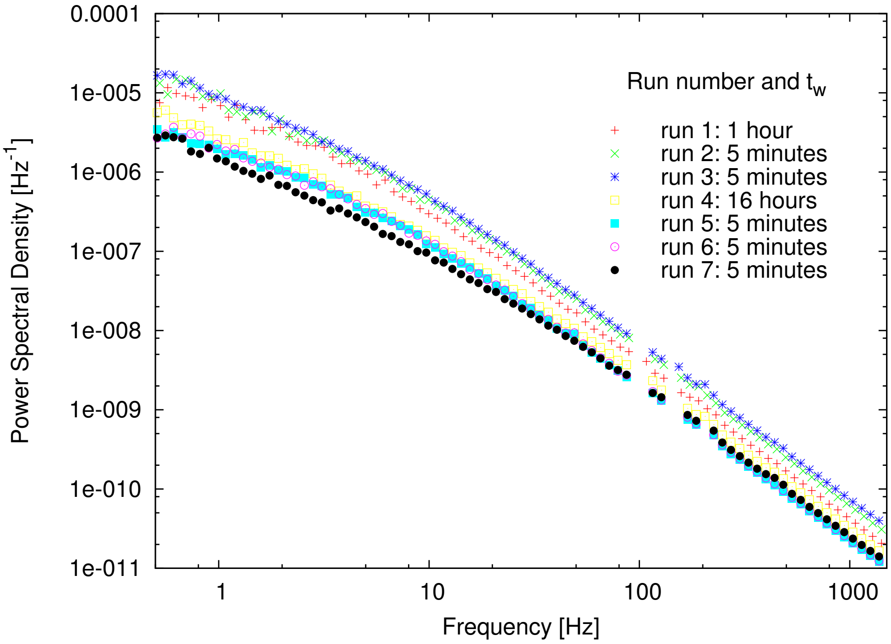

Figure 5.9: Power spectra for tracer motion in a $\phi = 62\%$ suspension, mean $D_s^s/D_0 = 0.0597$ from an average of the values obtained in runs 4-7, compared with 0.026 extrapolated from literature values.

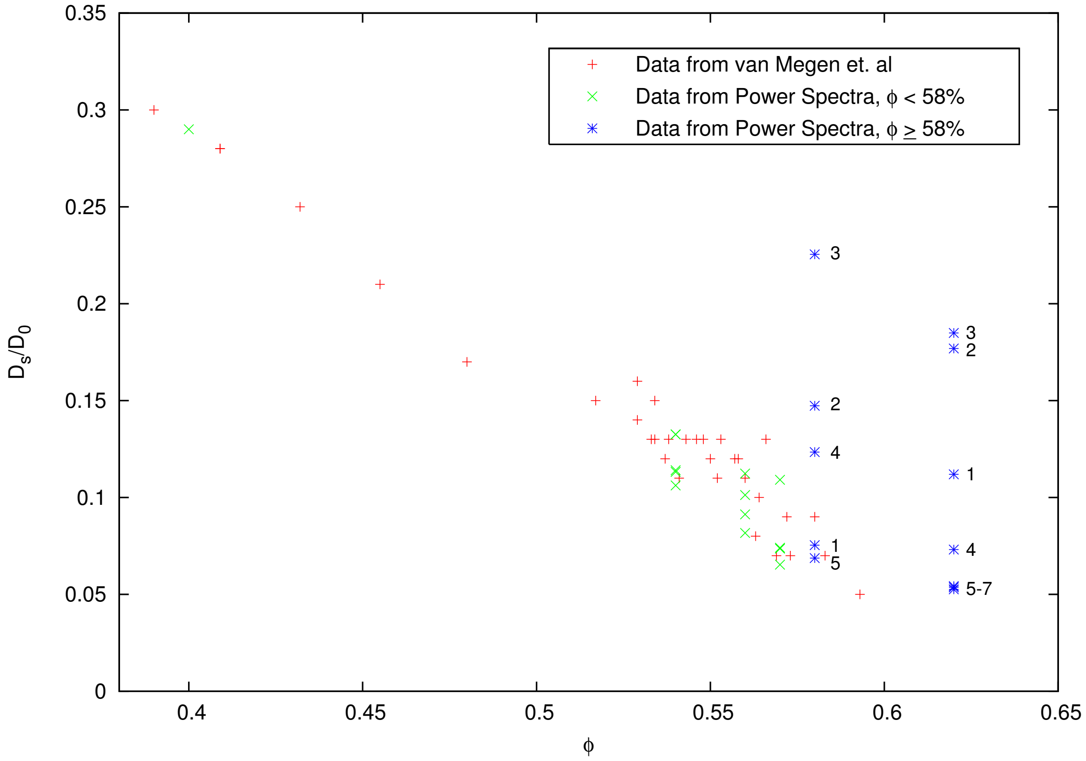

Figure 5.10: Comparison of D_s^s/D_0 measured by this optical tweezers study with previous light scattering studies. The red crosses are light scattering data from reference [117], the green crosses are power spectrum measurements from samples with volume fractions below the glass transition, and blue stars are data from above the glass transition. The order in which the measurements were made in the glassy samples has been labelled; the cage relaxation time in the $\phi = 58\%$ sample has been found to lie somewhere between 15 and 60 minutes. Relaxation times in the $\phi = 62\%$ sample are much longer, although measurements here have put a lower bound of 1 hour on the relaxation time.

time diffusion coefficient after a long waiting time (i.e. In runs 4-7) is reasonably consistent with a $\phi = 62\%$ hard-sphere glass — $D_s^s/D_0 = 0.0597$, compared to 0.026 extrapolated from the values in reference [53].

Figure 5.10 summarises the data presented thus far; all values of D_s^s/D_0 are presented together as a function of ϕ. My measured values for the short-time self-diffusion coefficient are compared to those kindly provided by W van Megen [120], based on a collection of published experimental results [117]. The spread in measured values for D_s^s/D_0 becomes much larger at the glass transition, reflecting the effect of drastically increased cage relaxation time, as detailed above.

5.2 Time-series data

This section is concerned with the size and dynamics of cage structures in dense colloidal systems. Several studies [88, 97, 100, 121] have used confocal microscopy to examine the evolution of the mean-squared displacements of particles in cages. The plateau at intermediate timescales in such data[6] allows a rough estimate of the size of a particle's cage of nearest neighbours in a dense suspension, as well as a mean lifetime for this cage.

The optical tweezers-based techniques here offer a far higher position resolution investigation of in-cage dynamics. The precision of confocal microscopy is essentially diffraction limited, although advanced fitting algorithms [122] have increased the resolution down to around ±30nm in the best case. Optical tweezers sidestep the real-space diffraction limit by using an interferometric position-detection technique, allowing refined position measurements down to the sub-nanometre scale, at sampling rates several orders of magnitude higher than confocal microscopy. This offers new insight into cage dynamics within single cages, where transient 'microcage' structures are observed. Integrated over time, these give rise to the larger cage sizes seen in previous studies. The cage lifetime is also seen to extend with increasing volume fraction, and lower bounds are placed on the yield stress of a cage in glassy suspensions.

5.2.1 Volume fractions below the glass transition

The data in the power spectra provide accurate and precise information about the short-time behaviour of a colloidal suspension, but do not provide a very detailed account of the long-time behaviour. To examine this area in more detail, position-time measurements are examined next. Figures 5.11 and 5.12 show histograms of particle position as a function of time, in a $\phi = 57\%$ suspension. As can be seen from the first figure (which gives raw data in nanometres), the particle's location is relatively stable for the first 150 seconds. The second figure shows that the distribution of particle positions is Gaussian in shape (the 60 second section shown is parabolic on this semi-log plot - a fit to the data based on a Gaussian distribution is included). After this initial period, the particle's environment shifts[7] *away* from the equilibrium trap position. By doing so, the particle gains a little potential energy from the optical field, but the second law of thermodynamics implies that the sample as a whole is (with overwhelming probability) in a more entropically favourable state.

---

[6] See figure 5.6 for examples of mean-squared displacement curves; although this is actually data from light-scattering experiments, the same information could in principle be extracted by confocal microscopy measurements.

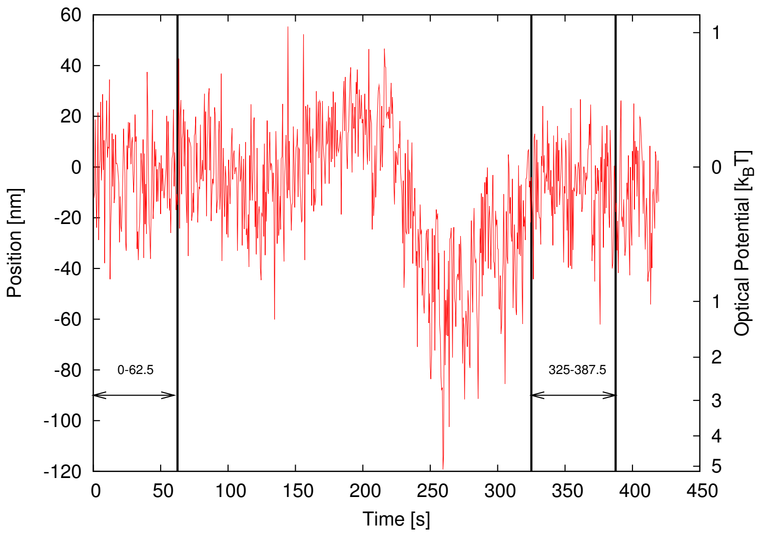

Figure 5.11: Position-time displays of a static measurement in a $\phi = 57\%$ suspension. The axis at the right-hand side shows the optical potential as a function of position. The data from which the short-time histograms in figure 5.12 were drawn are indicated.

The histogram showing particle position over the same length of time, but later in the measurement (325-387.5 seconds) is still fairly Gaussian, although it is now subject to a small optical potential, less than $0.1k_BT$. The data have actually been shifted 8nm to the right so as to provide a comparison with the earlier data, and a tendency towards the zero potential direction (to the right for unshifted data) can still be seen. The outer curve shows the position histogram for the entire measurement, and is non-Gaussian on this timescale (around seven minutes). All distributions have been normalised by maximum amplitude.

This type of rearrangement is shown schematically in figure 5.13, with considerably exaggerated scale; the actual motions observed experimentally are of the order of 8% of a particle radius. When particles numbered 4 and 5 move slightly, the other particles in the cage rearrange, including the central, shaded

---

[7] Structural rearrangements occur continuously in metastable colloidal fluids, driven by Brownian motion; this has been documented in confocal microscopy studies, for example, references [88, 97].

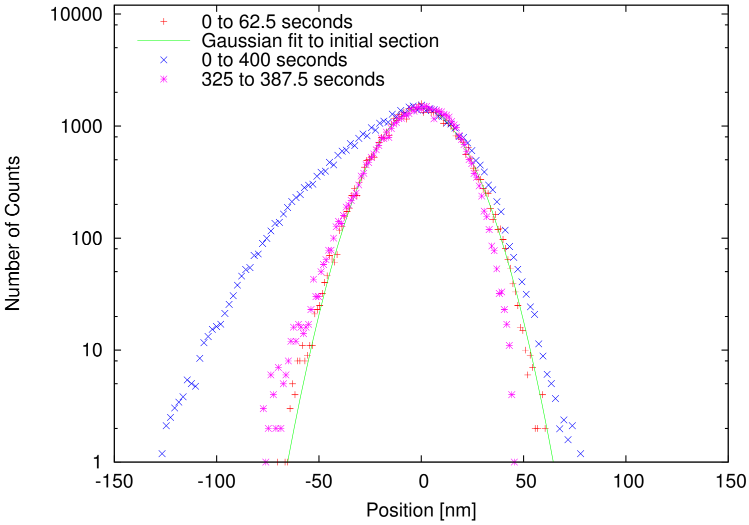

Figure 5.12: 1D histograms showing particle x-position at three different times during the course of a static-trap experiment in a $\phi = 57\%$ suspension. Histograms were made of subsections of the total data, as indicated in the key, to illustrate the short-time behaviour of the probe. The raw data corresponding to all these histograms is presented in the time series figure 5.11. The trap stiffness was $\kappa = 4.11 \times 10^{-3}$pN/nm.

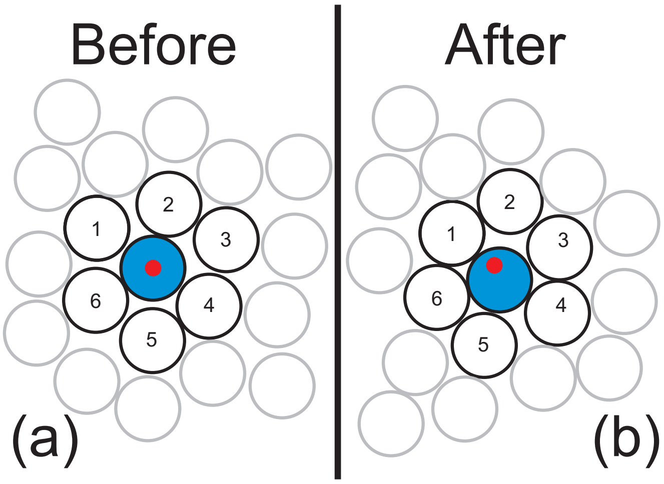

Figure 5.13: A schematic diagram showing a cage of particles (numbered 1-6) rearranging from state (a) to state (b). When the particles numbered 4 and 5 relax into positions lower down the diagram, the rest of the cage relaxes, shifting the position of the tracer relative to the optical trap (denoted by the red circle). The size of the rearrangement is exaggerated here; the actual probe displacements observed are about 15% of that pictured.

particle, which represents the probe. The laser trap (represented by the red dot) remains stationary, and lies much closer to the edge of the probe's edge.

Figures 5.14, 5.15 and 5.16 show a different measurement in the same $\phi = 57\%$ suspension, where a large but temporary cage rearrangement may be seen, which reverses during the measurement. Figure 5.14 shows the time series for a 15 minute measurement which has been down-sampled from 10kHz to 2.5Hz in order to keep the file size manageable. At around 500 seconds into the recording, the particle position jumps approximately 75nm in the positive y-direction, where it remains for about 100 seconds; it then moves back to around the original (optical equilibrium) position. Figures 5.15 and 5.16 shows 2D histograms of this measurement, which serve to illustrate the dynamic cage size and shape. Figure 5.16 shows the subsection of this recording where the probe particle has moved from the equilibrium trap position. The potential difference between the average of the original position, and average of the displacement between 500 and 600 seconds, is $2k_BT$.

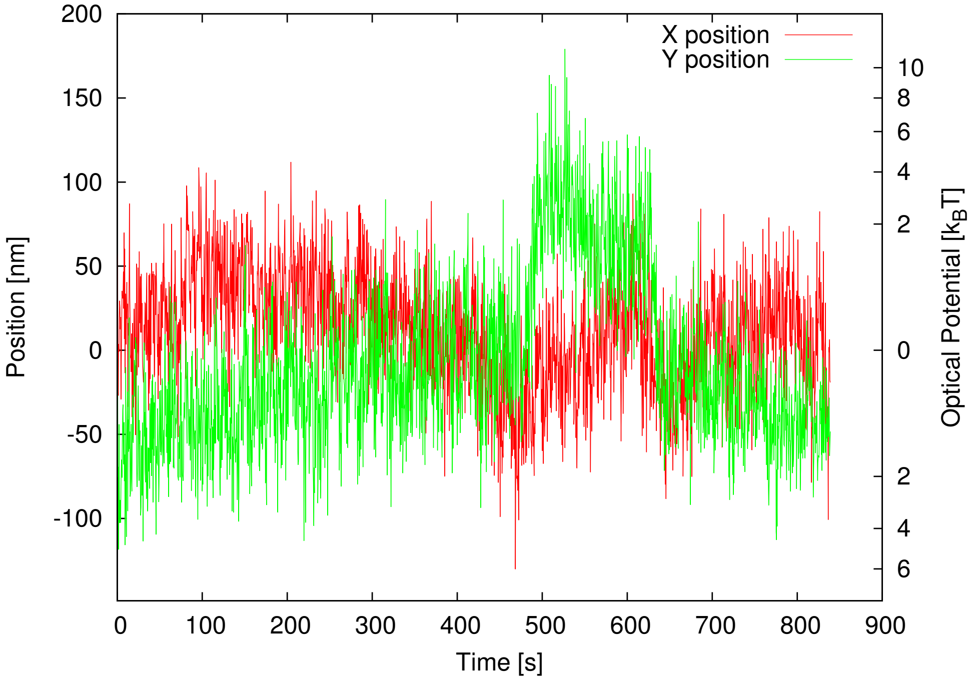

Figure 5.14: Position-time series for a probe particle in a $\phi = 57\%$ sample, note the temporary jump at around 500-600 seconds. The right-hand axis shows the optical potential energy ($U = \frac{1}{2}\kappa x^2$) due to the trap - the trap stiffness is $\kappa = 2.89 \times 10^{-3}$.

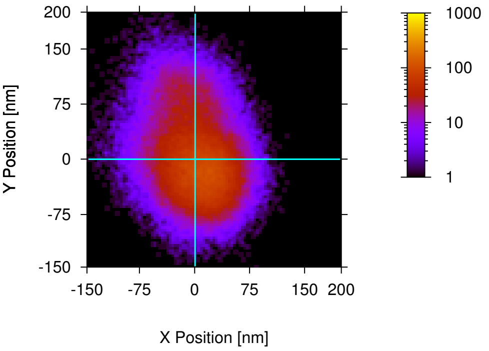

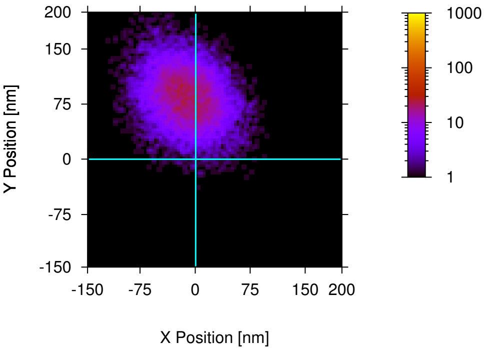

Figure 5.15: (*Left*) A 2D histogram the measurement in figure 5.14 (tracer position in a $\phi = 57\%$ suspension), resampled at 2.5Hz; again, the colour bar indicates the number of scans falling into each bin. The total length of the measurement was 15 minutes.

Figure 5.16: (*Right*) A subsection of the run in upper figure from 500-600 seconds, showing short-time behaviour in a cage structure.

The next 2D histograms (figures 5.17 and 5.18) are from a third measurement on the same sample. Again, the probe particle is able to diffuse within its cage of nearest neighbours, but does not escape from the cage. This is also seen in dynamic light-scattering studies, which show that the long-time diffusion coefficient (which is related to the average cage lifetime) decays very quickly on approach to the glass transition [53]. Figures 5.17 and 5.18 show subsections of this measurement, where the probe particle is localised by its neighbours for a time, before the whole cage shifts position. The graphs show movement on very short lengthscales - on the order of 1nm - which would be practically impossible to record using confocal microscopy. It should be noted that *cumulatively*, these movements give a 2D histogram showing a cage size of the same order as the putative cage size suggested by reference [97] for a $\phi = 56\%$ sample (around 15% of a particle radius, which in our case corresponds to 130nm). The graphs in the shorter-time sections show that for small time windows, ‘microcages’ are observed, where the distribution of particle positions is approximately Gaussian, and persists for long enough for a particle to diffusively explore its environment.

These microcages are too large to correspond to the ‘static cage’ limit, which is the free volume available to a diffusing particle if its shell of nearest neighbours were static. One could consider a thought experiment to illustrate this idea; if the particles making up a cage were prevented from diffusing using extremely stiff optical traps, the remaining space within which the caged particle may diffuse is the static cage size V_{SC}. This quantity is obtained as a fraction of the particle radius from the volume fraction of the suspension:

$$V_{SC} = 1 - \frac{\phi}{\phi_{rcp}}, \tag{5.1}$$

where $\phi_{rcp} = 64\%$ is the random close packing volume fraction. For a 57% sample, the radius of the static cage is 33nm, which is around half the width of the distributions in figure 5.18, suggesting that the microcages observed here have a size somewhere in between the static cage limit and the dynamic cage size observed by confocal microscopy and light-scattering methods. Indeed, when the evolution in their position is integrated over appropriate times (that is, longer than the β timescale, but shorter than the final lifetime of the cage), the microcages give a distribution of particle positions very similar to that observed by the other techniques.

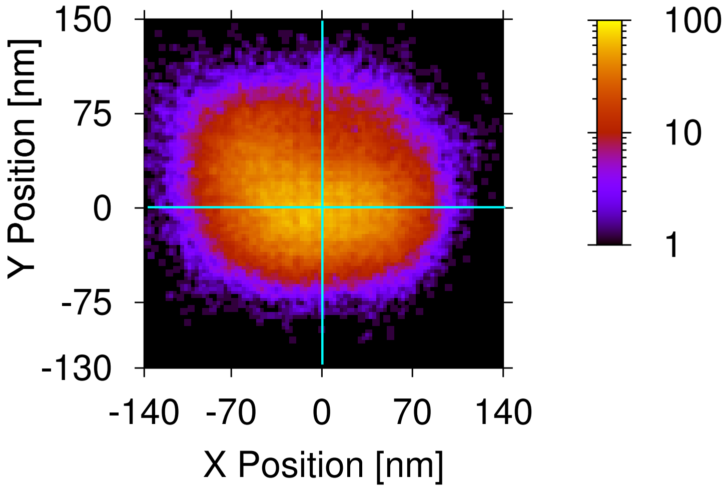

Figure 5.17: 2D histogram of tracer position over 800 seconds in a $\phi = 57\%$ suspension. The bin size here is 2.8nm, and the colour bar indicates frequency.

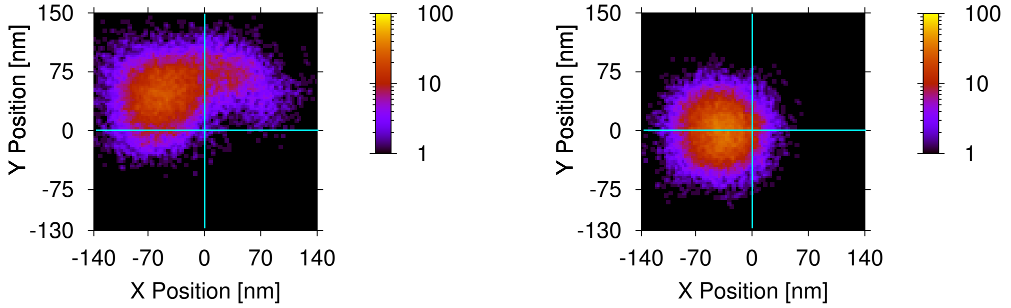

(a) 0-200 seconds.

(b) 200-400 seconds

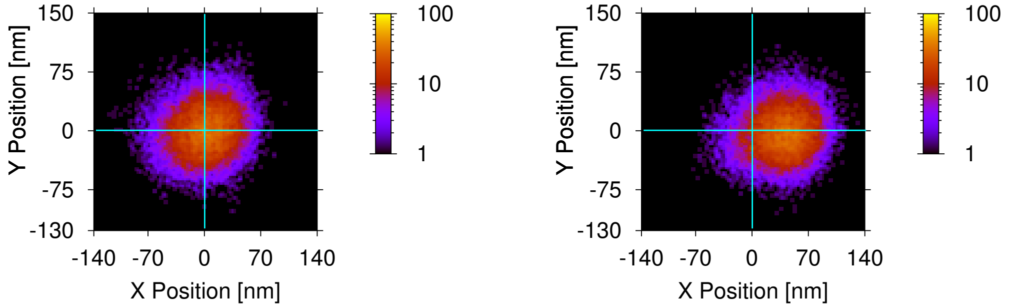

(c) 400-600 second

(d) 600-800 seconds

Figure 5.18: These graphs are subsections of the measurement in figure 5.17. Figures (a)-(d) are successive 200 second portions (with timeframes as labelled) showing relatively stable average position over their duration.

5.2.2 Volume fractions above the glass transition

In glassy samples, the dynamics slow considerably. Short-range in-cage motion still occurs, but on an even shorter length scales, as there is less free volume available in these denser samples. There are still discrete jumps in particle position, but they are much less frequent. In the following graphs (in a volume fraction of $\phi = 62\%$), the optical trap is displaced from the probe particle centre. The particles have average optical potential energies of up to $32k_BT$ (corresponding to an optical force of 1.0pN) which, although relatively large by equilibrium thermodynamic standards, is still insufficient to produce large-scale cage rearrangements at this high density. To calculate the local stress due to the optical potential, the approach adopted in chapter 6 (where the optical force is divided by the cross-sectional area of the probe, πa^2) yields a value of 0.37Pa. This value is much lower than the putative yield stress of the sample, also calculated in the chapter 6 (around 42Pa), which explains why no substantial relaxation is observed over these timescales - only a very long-time Brownian relaxation would be expected at this stress.

Figures 5.19 and 5.20 show particle motion at an optical potential energy of $32k_BT$; the time-resolved measurements show that there are occasional detours towards the zero-potential region, but the particle's trajectory is still dominated by its cage. Figures 5.21, 5.22 and 5.23 show data from a different experiment in the same $\phi = 62\%$ sample. There is a slight rearrangement approximately fifteen minutes into the experimental run, but this only lowers the probe's potential energy by around $1.5k_BT$. The overall shape of the particle's 2D histogram is also non-circular - this shows the compromise in the particle's trajectory when the optical force competes with the confining effect of the neighbouring host particles.

As has been shown previously, local stresses can persist for a long time. Figures 5.21 - 5.23 show the results of experiments conducted five minutes after translation through the sample, after which time the stresses are not expected to have relaxed substantially. Future work on glassy and near-glassy samples should include long-time experimental runs conducted after a period of steady dragging, to investigate the relaxation of accumulated stresses.

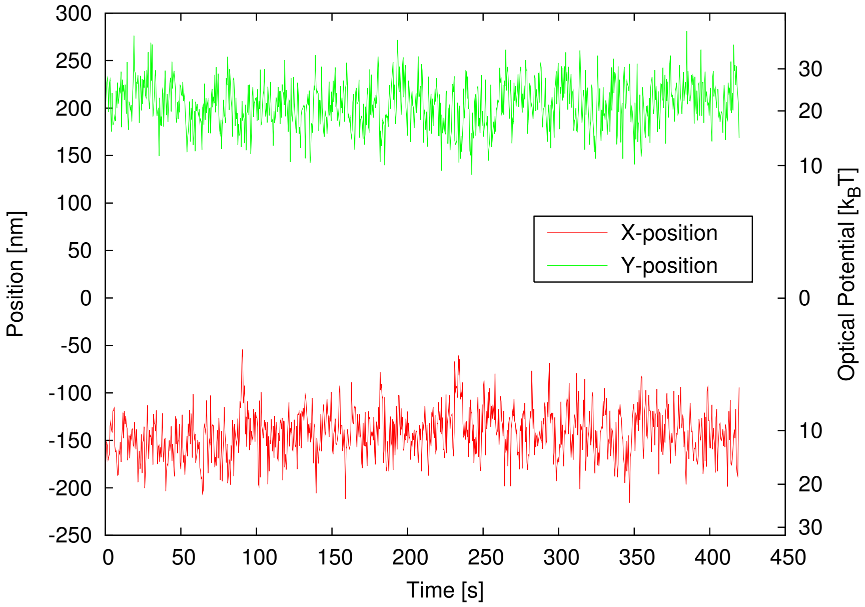

Figure 5.19: Time series of the data in figure 5.20. The data has been resampled from the original rate of 10kHz down to 3.3Hz.

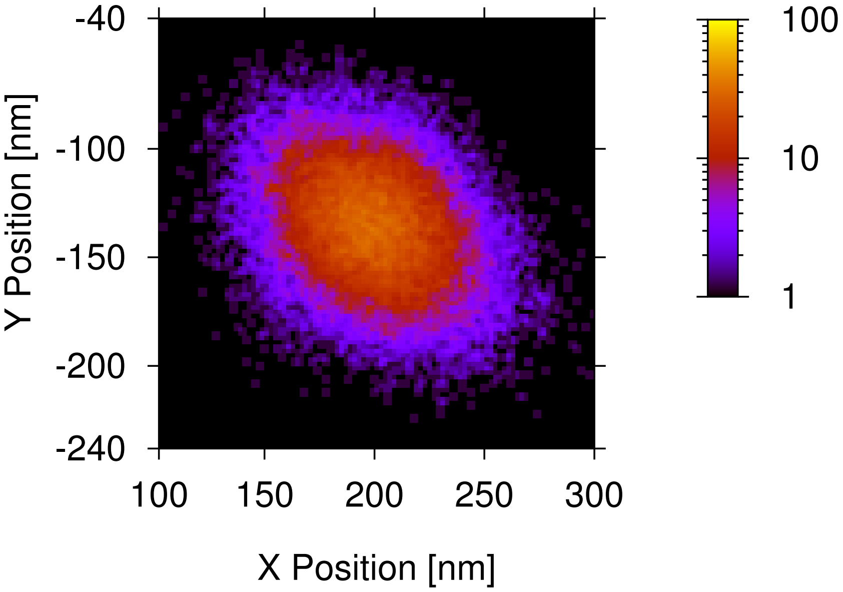

Figure 5.20: 2D histogram of displacements in a $\phi = 62\%$ glassy sample. At the average particle position, the potential energy due to the optical trap is $\sim 32 k_B T$.

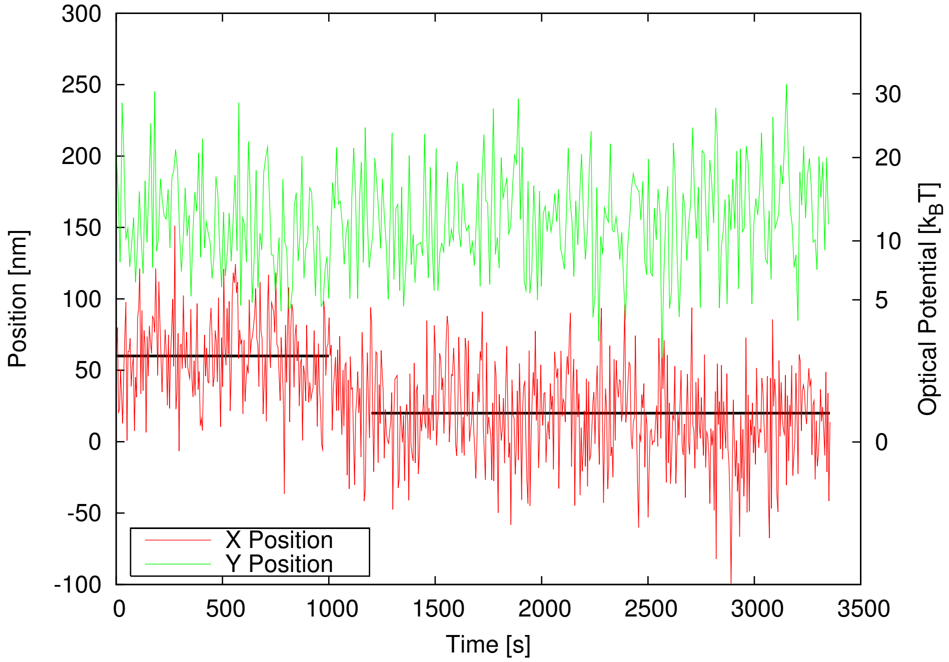

Figure 5.21: A time series of a measurement in a $\phi = 62\%$ sample, where a cage rearrangement occurs at around 1000 seconds. The horizontal black lines show the range of data used to make the histograms in figures 5.22 and 5.23, and the mean values for these ranges. The cage rearrangement accompanies a decrease in optical potential from $14.8 k_B T$ to $13.2 k_B T$.

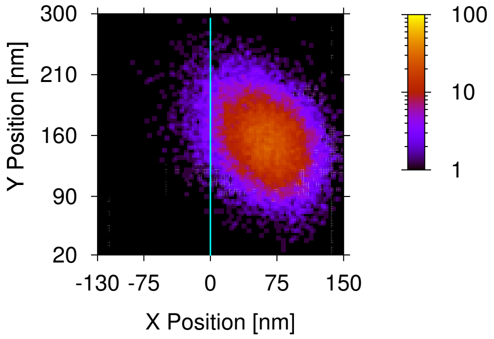

Figure 5.22: 2D histogram of data from the first 1000 seconds of the recording in figure 5.21.

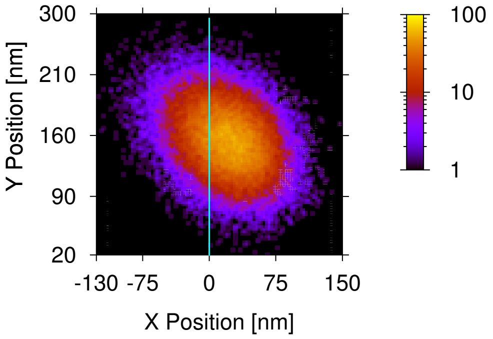

Figure 5.23: 2D histogram of data from 1200 seconds to the end of figure 5.21.

Chapter 6

Dragging measurements - Active Microrheology

In order to further investigate the properties of colloidal suspensions, optical tweezers were used to impose larger local stresses on the colloidal host via a melamine tracer. This was achieved by translating the sample stage itself while keeping the optical trap stationary; the tracer was forced past its nearest neighbours, which impeded its progress, pushing it out of the equilibrium trap position (this type of measurement is referred to as a 'drag measurement' herein). Using the force-calibration presented in chapter 3 and the cross-sectional area of a tracer, this increasing displacement was converted into a stress measure, which peaks at the local yielding stress of the suspension. Experiments were performed at several different stage speeds and volume fractions.

6.1 Average forces

6.1.1 First approximation - effective viscosity

The most straightforward analysis of the drag measurements is to examine the (nominal) average force acquired from the average displacement from equilibrium, as a function of drag speed and volume fraction. The measurements were started with the stage stationary, and the particle in the optical trap. After around thirty seconds, the stage was activated and the particle dragged through the suspension, typically for around 3000 seconds (50 minutes). The displacement from equilibrium varies significantly as a function of time, as the surrounding colloid is highly inhomogeneous. An example of force-time measurements (same stage speed, different volume fractions) is given below in figure 6.1. Qualitatively speaking, it can be seen that the average force increases as a function of volume fraction. The fluctuations about the mean also increase in higher volume fractions — the probe particle experiences a greater range of forces as it is dragged through the host suspension.

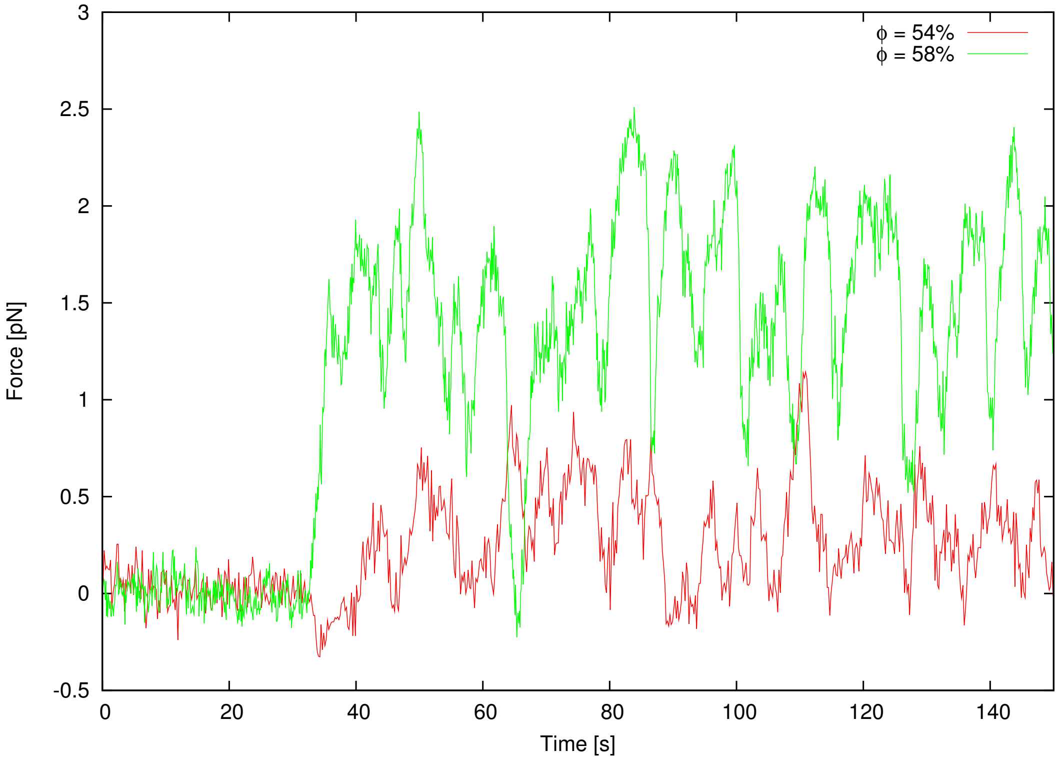

Figure 6.1: Force-time series for dragging experiments in two different volume fractions, $\phi = 54$ and 58%, at a speed of 0.4μm/s. The slight negative detour at around 34 seconds in the lower volume fraction measurement is due to mechanical backlash in the stage motor; this region is excluded from the analysis of results.

In order to obtain average forces from these measurements, the initial quiescent section of the measurement and the first 50 seconds of dragging are discarded on the assumption that what remains constitutes ‘typical’ dragging behaviour. In the case of the results in figure 6.1, the first 30 seconds constitutes the quiescent period, so a total of 80 seconds is removed from the data set before the rest of the analysis is conducted. This procedure was conducted manually on each set of data. The arithmetic mean is taken of these remaining data values, and is presented as a function of ϕ and drag speed in figure 6.2.

A striking feature of the graph is that it shows an abrupt change of behaviour as a function of volume fraction. Below the glass transition at $\phi \approx 58\%$, the behaviour appears largely consistent with that of a Newtonian fluid[1], that is to say that the measured force is directly proportional to the flow speed, albeit with large fluctuations and an enhanced viscosity (see figure - least-squares fits are included to illustrate this trend). Error bars to indicate the spread of data are omitted for the sake of clarity, as the standard deviation is approximately the same as the mean (the standard deviation of these data are examined in figure 6.8 at the end of section 6.2). Effective viscosities are obtained from the forces and

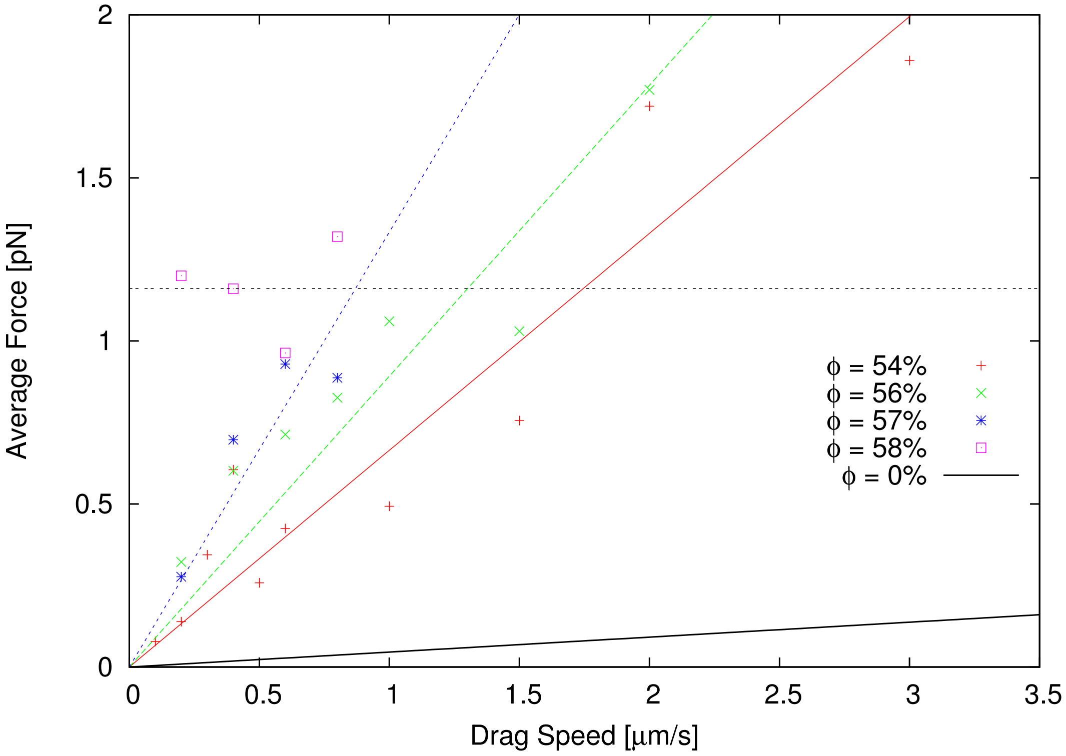

Figure 6.2: Average force as a function of stage speed and volume fraction. At volume fractions below the glass transition ($\phi \approx 58\%$), the suspension appears fluid, with force measured tending to zero at zero stage speed. Least-squares fits are included for volume fractions below the glass transition, and the dotted horizontal line is a guide to the eye, illustrating the qualitative change in behaviour in the glassy sample. The $\phi = 0\%$ is a schematic showing the forces on a tracer in bare solvent, based on the viscosity measured previously.

---

[1] The data point at $0.8\mu\text{m/s}$ in the 57% suspension is a special case — this is discussed in the next section.

drag speeds using Stokes law, $\eta_e = F_{avg}/6\pi a v$. Least-squares fits to the data were performed, yielding values of 36.3, 49.9 and 74.5mPa·s for the $\phi = 54\%, 56\%$ and 57% suspensions respectively, which are much higher than the value of 2.56mPa·s for bare solvent. The $\phi = 0$ line represents the expected average force on this size of tracer in bare solvent, based on the viscosity measured in chapter 4.

Shear measurements may be described in terms of the dimensionless Péclet number outlined in chapter 4. This number may be said to embody the relative importance of diffusion to the overall particle behaviour; it is given by Pe $= \tau_B/\tau_{\dot{\gamma}}$ where $\tau_{\dot{\gamma}}$ is the time taken to separate two identical adjacent particles by a distance equal to their radius by mechanical shearing, and τ_B is the time a particle takes to diffuse a distance of its own radius by Brownian motion. Shear dominated measurements will have Péclet numbers greater than 1, and measurements dominated by diffusion will have numbers less than 1. In the Péclet number range of our experiments (Pe = 1-40), samples with a volume fraction under ϕ_g would be expected to act as a viscous fluid [105, 106]. Naïvely, one might suggest that the viscosity observed is close to, or the same as, the high-frequency viscosity obtained during the passive microrheological measurements in chapter 5, which coincided well with the existing light scattering measurements. Figure 6.3 shows a comparison of active, passive and light scattering measurements, in terms of diffusion coefficients[2](D_s/D_0 for the passive and light scattering measurements, D_e/D_0 for the dragging measurements). Clearly, the observed viscosities are significantly *larger* than those obtained from passive measurements.

The above data would suggest that at least part of the above assumption (Stokes' law is valid, the suspension acts as a continuum) is not viable. All of the values measured in dragging experiments are approximately a factor of two larger than those measured by light scattering and passive microrheology. In many ways this is not surprising; the values from the other techniques pertain to high-frequency behaviour, and all of the work here is at relatively low shear rates. Theoretical work by Squires et al. [123] on dilute suspensions of charged colloidal particles finds that there are two distinct limiting cases for local perturbations caused by nonlinear microrheology. At the highest shear rates, the mechanical motion of the probe particle dominates the local structure. The leading half of the probe is surrounded by a dense layer of host particles, and this layer also lines

---

[2] Effective diffusion coefficients may then be defined as $D_e = k_B T/6\pi\eta_e a$.

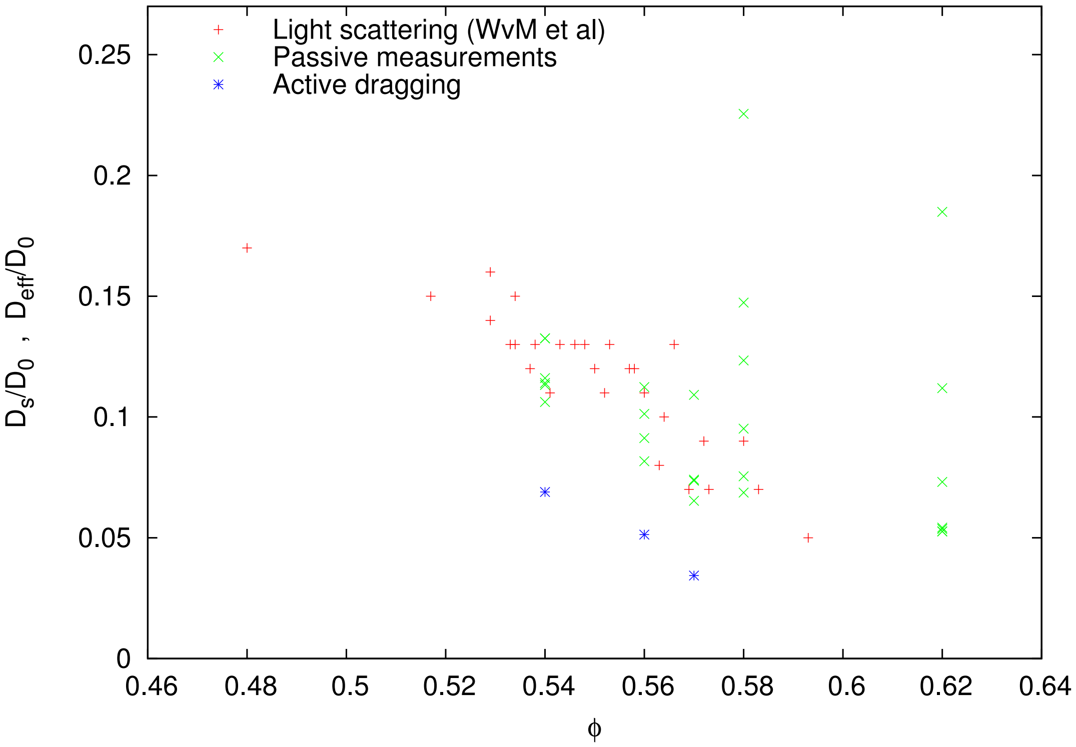

Figure 6.3: A comparison of active rheology data with that obtained from light scattering measurements. The effective diffusion coefficients from dragging experiments are significantly smaller than those obtained from passive techniques.

the probe's wake, which has been swept clear — this is the behaviour seen by Meyer et al. [8], where the probe is moved fast through small host particles. At lower shear rates, diffusive motion is dominant; the high density region extends further from the probe in the direction of motion, and the particle's wake extends symmetrically behind (the host density pattern is described as a 'diffusive dipole'). In this low-shear-rate regime, the high-density region in front of the probe extends its influence significantly. Unpublished results of dragging experiments using magnetic tweezers apparatus undertaken by Weeks and co-workers [124] have also suggested that the shear zone extends well beyond the radius of the probe.

In light of this, it could be argued that the most obvious modification to the basic Stokes description is to assign an effective radius to the dragged particle. If a host particle has a position in the plane perpendicular to the drag direction which separates its centre from the probe's by less than two particle radii, the particles will collide, otherwise they will not. This idea is illustrated in figure 6.4, where the particles whose contact angle with the probe is less than 45° are drawn in green, and those with contact angle between 45° and 90° drawn in red.

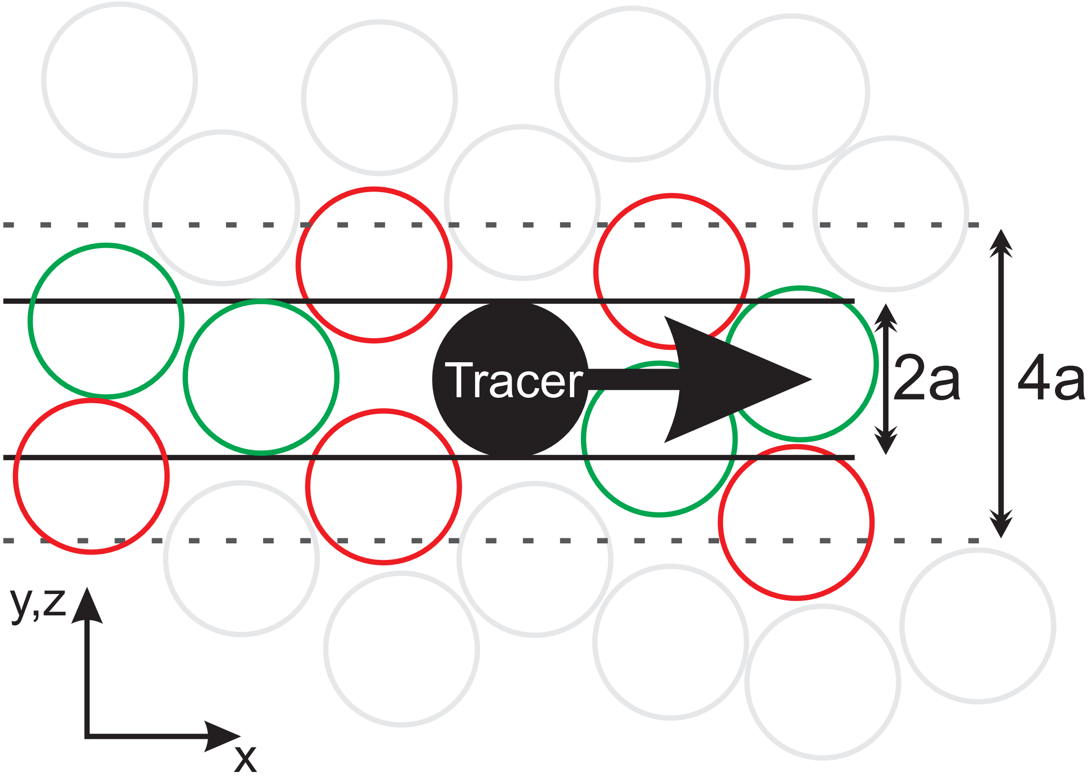

Figure 6.4: Effective radius - the distance within which host particles will directly collide with the probe. The green particles' centres are within one particle radius of the probe centre's path; the red particles' centres lie just outside this, but within the effective radius. The light grey particles' centres lie outside the effective radius.

An effective radius may be introduced, which is twice the physical radius of the probe particle; this quantity goes some way towards reconciling the physical probe dimensions with the extent of its influence. Although the exact motion of particles around the dragged tracer will be complex, and a fruitful area for further study[3], our measurements (while not giving a complete picture) at least add weight to the argument that a region greater than the cross-sectional area of the probe must be considered in any description of the shearing action.

---

[3] Initial studies, on a system where the probe is much larger than the host are presented in reference [8].

6.2 Displacement histograms

In this section, histograms of the force experienced by the probe particle are presented as functions of both dragging speed and volume fraction. These show the mean force experienced by a tracer, and the range of forces for each case. Broadly speaking, the drag speed dictates the average displacement, and the volume fraction determines the total range of forces. At volume fractions below the glass transition, the forces roughly follow a Stokes-type relationship, where force is proportional to velocity, albeit with a viscosity much greater than that in the bare solvent case. At the glass transition, both the average forces and the range of forces increase significantly, and are independent of drag speed.

6.2.1 Dragging experiments in samples with $\phi < \phi_g$

To look in more detail at the behaviour of a dragged particle, the frequency-distribution of forces at different drag speeds is examined, and presented here. As previously seen in figure 6.1, the trapped particle's motion is erratic. The force experienced by the probe as it is forced through the host colloid varies according to the configuration of its nearest neighbours; histograms are a way of examining the distribution of forces over the whole length of a measurement.

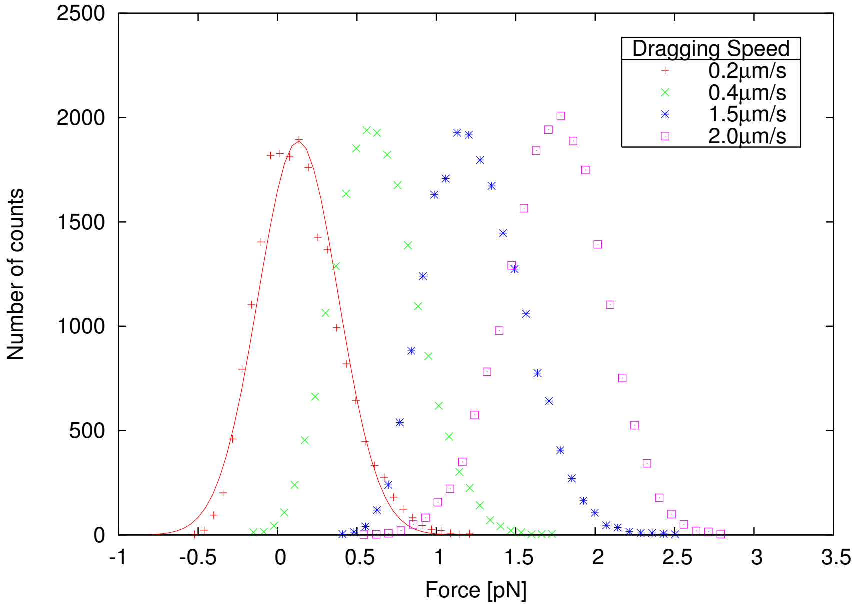

Figure 6.5: Drag histograms in $\phi = 54\%$.

Figure 6.5 shows a selection of the drag measurements in the $\phi = 54\%$ sample (the rest are omitted for the sake of clarity). Unlike dragging measurements in bare solvent (see chapter 3), the histograms of particle position are non-Gaussian, particularly at low speeds. This is illustrated by the measurement at the lowest speed (a Gaussian fit is included for comparison); the distribution is obviously skewed towards the zero-potential region. At first sight, this is at odds with the work in references [114] and [125], which examine the response of a colloidal system to a probe driven with a constant force, in experiment and simulation respectively. Habdas et al. found that if a constant force was applied to probe particles in a dense suspension, the distribution of velocities produced was Gaussian; one might suggest that if a probe is dragged at a constant *velocity*, the distribution of *forces* on the probe would also be Gaussian[4]. In fact, optical tweezers experiments are subtly different to those using magnetic tweezers; although the velocity of the *trap* is constant, the probe velocity and probe force both vary. If a probe particle is displaced from its equilibrium position by the surrounding colloidal host, upon building up sufficient force to break its cage (due to increasing optical potential), it will momentarily be travelling faster than the trap, as it is pulled towards the equilibrium trap position. This situation may lead to the biasing of the force distribution towards the equilibrium position (which does not arise in constant-force experiments).

Another factor which might contribute to the asymmetry relates to the actual value of the optical potential at a particular position - at small displacements, Brownian forces still dominate the probe motion. For example, in figure 6.5 a force of 0.2pN (equivalent to a displacement of 45nm) corresponds to an optical potential energy of $\sim 1k_BT$. Optical potentials around this value represent the crossover regime between Brownian-dominated forces and trap-dominated forces, so a purely trap-dominated Gaussian distribution is perhaps unlikely. At higher drag speeds, the distribution of positions is more Gaussian, and this would seem to add weight to the 'competing Brownian/trap force regime' hypothesis. In the experiments of Habdas et al., the probe experienced a constant force, which gave rise to a Gaussian distribution of instantaneous velocities; the same is true for our experiments at high drag speeds where the optical potential is significantly greater than k_BT. This idea is quantified at the end of the section (figure 6.9) with a comparison of the third moment of the distribution of forces.

---

[4] This is consistent with a generalised Stokes approach to viscous drag force.

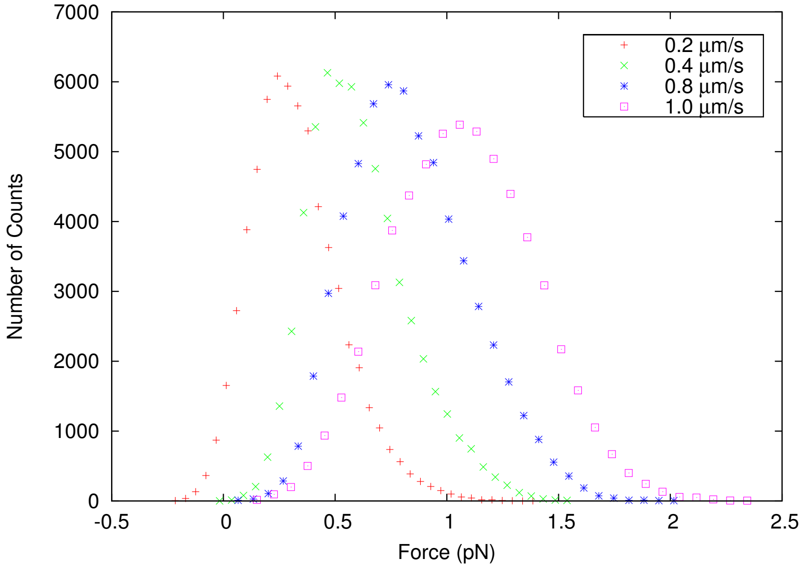

Figure 6.6: Distribution of forces in a $\phi = 56\%$ colloidal suspension during dragging experiments.

Figures 6.6 and 6.7 show a selection of the force-drag speed histograms obtained in dragging measurements in the $\phi = 56\%$ and 57% samples. As in figure 6.5, the histograms generally broaden and become more Gaussian with increasing drag speed (the clearest evidence of non-Gaussian behaviour is in the highly asymmetric wings of the distribution). The result obtained at the highest speeds in both graphs are more irregular in shape than the other measurements; this is because the particle escaped the optical trap relatively soon after the drag measurement was started, so only a limited data range was available for producing the histogram[5]. All measurements are normalised by the total number of counts.

The $\phi = 57\%$ measurement also shows the start of a trend which becomes clearer in the $\phi = 58\%$ sample; there is a narrower spread in the mean of the histograms, and they are more irregular in shape. This is due to the emergence of friction-like, stick-slip behaviour [126] — this idea is described in more detail in the next section, where the effect is more prevalent. At the lowest shear rates, surrounding particles have time to rearrange to accommodate the probe particle as it moves, but at higher speeds the probe motion is more intermittent as it

---

[5] Both samples have a useful recording time of around 200 seconds, as opposed to ~ 3000 seconds for the other measurements.

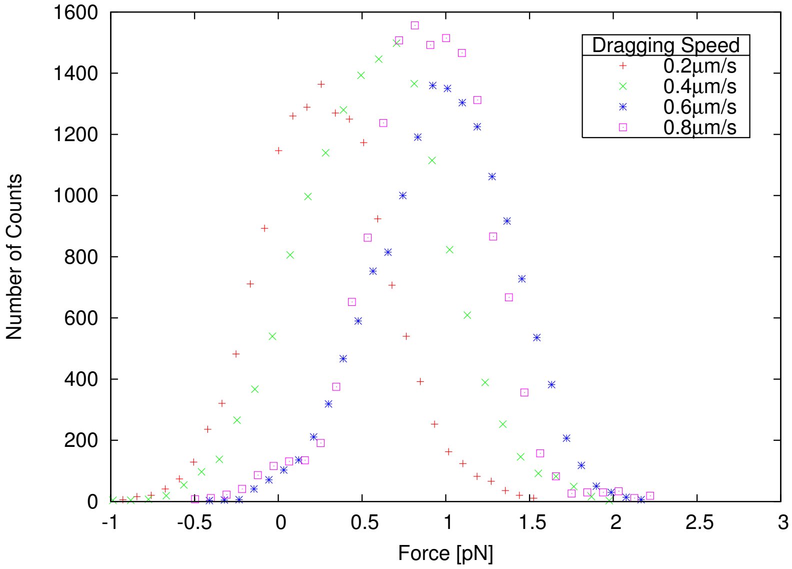

Figure 6.7: Distribution of forces in a $\phi = 57\%$ colloidal suspension during dragging experiments.

successively gets stuck, and is then released when the accumulated force exceeds the local yield force. The microrheological study of Habdas et al. supports this idea. In that work, increasing forces were applied to many magnetic beads simultaneously, and their progress observed by confocal microscopy. A certain yield force is needed in order to move the tracer particles through suspensions with volume fraction greater than the melting point ($\phi_m = 54.5\%$), and there is quite a spread in the data obtained ($\pm 30\%$ of the mean). This could be attributed to local fluctuations in the yield force due to spatial inhomogeneity; indeed, my measurements have a similar spread, which is likely due to the same phenomenon.

The standard deviations of the histograms at all drag speeds and volume fractions below ϕ_g are presented in figure 6.8. All drag measurements have a standard deviation that is significantly higher than in the static (zero speed) case, and generally speaking, the standard deviation increases with drag speed. It is worth remarking also that the standard deviation of the results in the $\phi = 57\%$ sample shows a smaller spread; again, this is taken to mark the onset of solid-like behaviour which becomes even clearer in the $\phi = 58\%$ sample.

The amount of asymmetry in each histogram may be quantified by examining the third moment of the distribution (the mean and variance of a data set are

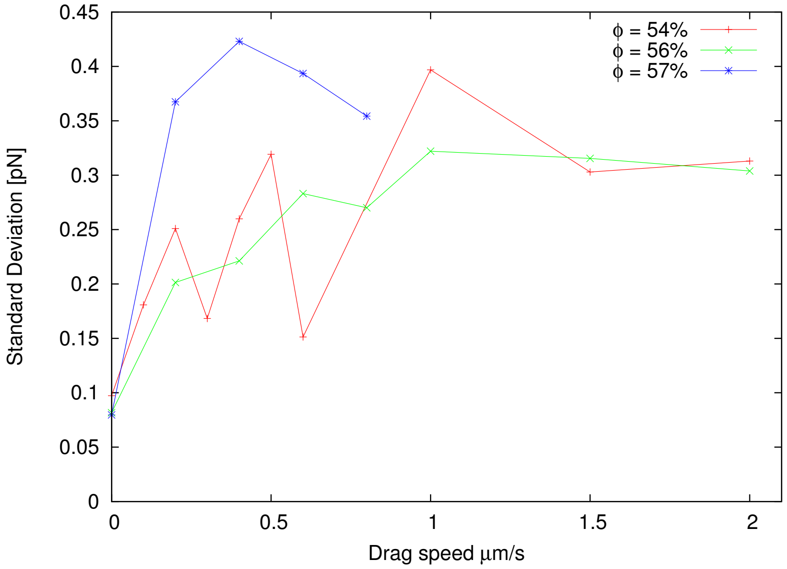

Figure 6.8: Standard Deviation of the histograms in figures 6.5 to 6.7. The standard deviation in drag measurements is always greater than that in the static case, and generally increases with faster drag speeds; in the highest volume fraction, this is not as apparent, although the mean of the histograms (see figure 6.2) does show a general increase.

the first and second), given by [127]:

$$\mathrm{Skew}(x_j) = \frac{1}{N}\sum_{j=1}^{N}\left[\frac{x_j - \bar{x}}{\sigma}\right]^3 . \tag{6.1}$$

Figure 6.9 gives the skewness of all of the histograms in drag speeds below ϕ_g. Although the spread of data precludes any speculation as to the form of the decreasing skewness, the data at drag speeds less than or equal to 1μm/s show a distinct downward trend. This means that the histograms become more symmetrical at higher drag speeds, and this reflects the decreasing importance of Brownian motion at increasing distances from the trap centre. The data point at 0.8μm/s in the $\phi = 57\%$ suspension should be treated with caution, as the graph in figure 6.7 shows the emergence of a different, solid-like behaviour in this volume fraction.

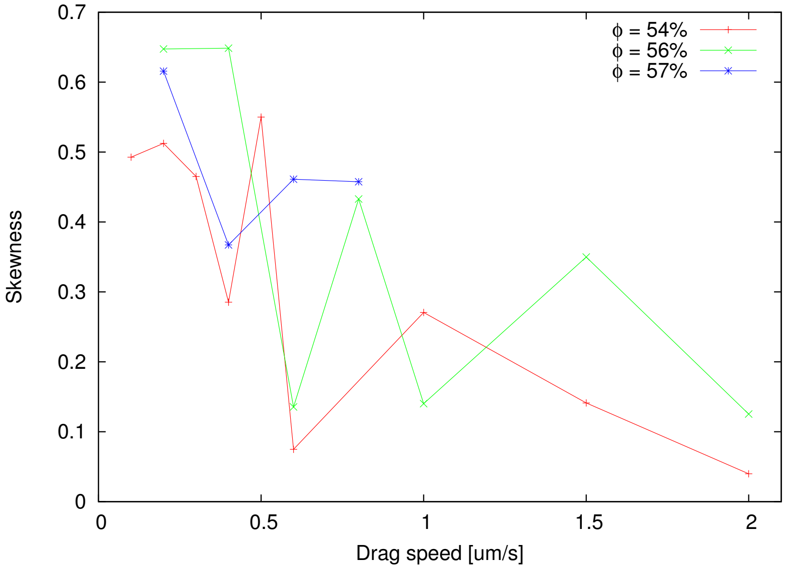

Figure 6.9: Third moment (skewness) of the histograms in figures 6.5 to 6.7. The overall trend is a decrease in skewness with increasing drag speed.

6.2.2 Dragging experiments in samples with $\phi \geq \phi_g$

As the volume fraction increases past $\phi_g \approx 58\%$, two main features become apparent. Firstly, as seen in figure 6.2, the measured average force is largely independent of drag velocity. This velocity-insensitivity is well known in solid friction experiments, like those in reference [126]. That letter details the force necessary to drag a piece of sandpaper across carpet. The evolution of force with time observed by Feder et al. is strikingly similar to that in our experiments — a system accumulates force up to a certain critical value and then relaxes, with both accumulation and relaxation processes occurring as a hierarchy of smaller steps. This hierarchy of steps is explored in greater detail in section 6.3, but a central feature, the critical yield force, is demonstrated in figure 6.10; the average force is roughly constant for all drag speeds. The work in references [109] and [54] on sheared colloidal suspensions shows the emergence of a yield stress for suspensions with volume fractions around $\phi_g \approx 58\%$; the results in these references give yield stresses of around 1.5Pa for a volume fraction of $\phi = 58.4\%$ and around 10Pa for a $\phi = 62.0\%$ suspension. Estimates of the yield stress in these measurements were made from our measurements by examining the raw data in the force-time series. In order to convert average force (as described previously) to stress, an effective area over which the force is applied must be invoked. It is not entirely

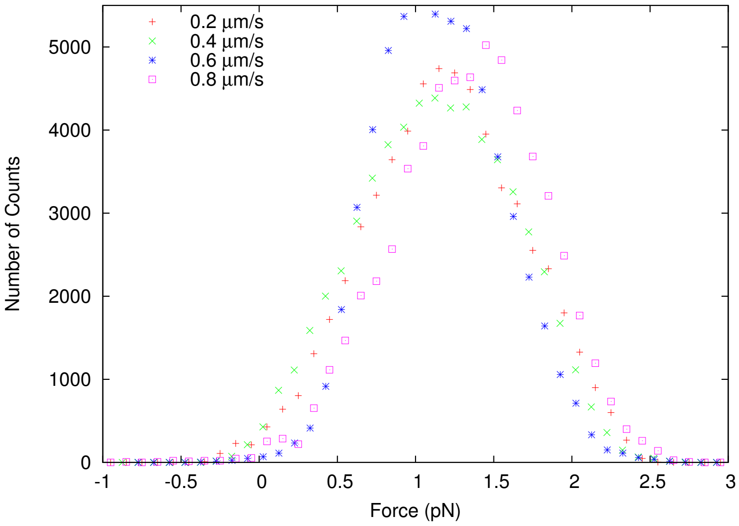

Figure 6.10: Force histograms for a $\phi = 58\%$ suspension. The average displacement is essentially constant, and only increases at the highest velocities.

clear which area should be considered in this case; in the absence of a suitable alternative the particle's cross-sectional area (πa^2) is used here. In order to make a comparison with the results of Petekidis et al., the stress must be scaled appropriately. Stress is a form of energy density, $\sigma \sim a^{-3}$, so our values of yield stress should be scaled accordingly. The resulting values – 42Pa and 63Pa for the $\phi = 58\%$ and $\phi = 62\%$ samples respectively – overestimate the yield stress by around a factor of ten. In fact, the authors in reference [109] use two different methods for extracting a yield stress, which give two quite different values - the method based on flow curves (graphs of shear stress against shear rate) is more comparable to our own method and is typically lower than, although within an order of magnitude of, the other (sample creep) method. Another factor affecting our value is the highly localised nature of the measurement; the vast majority of the rest of the colloidal suspension is not perturbed by the shearing action and thus is not shear-thinned, unlike the macroscopic case. The value of this kind of comparison between macro- and microrheology seems quite limited, certainly in the quantitative sense. In the former case, *all* particle cages in a sample are sheared, whereas in the microrheological case, the vast majority of cages are unsheared. To this end, it is interesting to note that the results obtained by Habdas et. al [114], measured on a sample with similar properties (probe size, host size, solvent viscosity) to our own, show very similar values for the yield *force* of dense suspensions, typically on the order of ~1pN. This value is broadly in agreement with the theoretical results cited in that paper [128] based on the estimates of the free energy barrier localising a particle. It would seem reasonable to suggest that there is further work, both theoretical and experimental, that is required in order to bridge the gap between micro- and macrorheology.

At the highest volume fraction ($\phi = 62\%$), a stronger trap (stiffness $\kappa = 6.5$pN/nm, around 60% stronger than previous measurements) was necessary, as the probe experiences much larger range of forces. This can be seen in the histograms of figure 6.11, where particle force distribution becomes increasingly broad and irregular. This implies that both the range and the mean value of cage yielding forces increase with volume fraction as random close packing ($\phi = 64\%$) is approached. The mean values of the histograms are apparently different, but given the poor quality of the data, this may be misleading; this graph is included only in the interests of completeness, and the average forces have been omitted

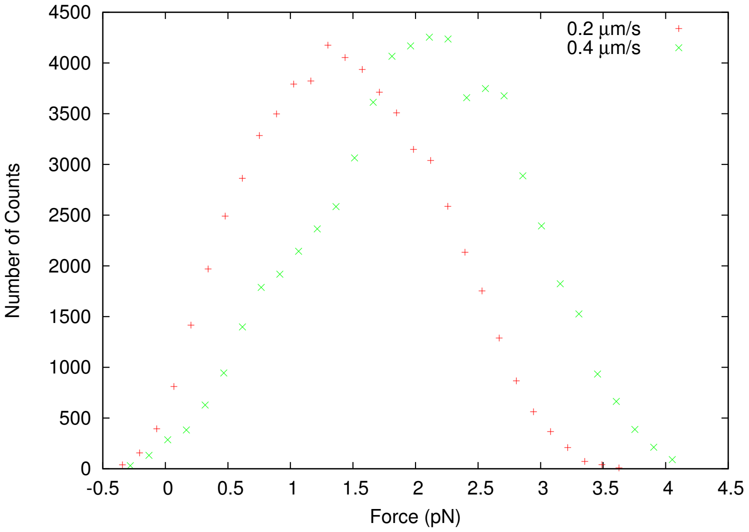

Figure 6.11: At a volume fraction of $\phi = 62\%$, the shape of the force distribution function is irregular, with a high mean value and large standard deviation. The trapping laser was turned up to its maximum value to perform these measurements, as the yield stress is large (around 1.2 Pa).

from figure 6.2. If the range of possible cage yielding forces is sufficiently large (which is hinted at by the broad observed distributions), the true distribution of forces may not have emerged, and that longer data sets are needed — this would account for the irregular histogram shape. Figure 6.12 serves to demonstrate the erratic motion of the tracer through the glassy sample; the sharp peaks in the figure are typically followed by sudden troughs, as the particle jerks onward through the host (implying that the stress relaxation happens suddenly rather than gradually). The tracer is stopped, an optical force builds up, and the particle pushes forward for a relatively large distance before becoming obstructed again.

Figure 6.13 shows another method of quantifying this motion. The probe's absolute position in the sample is obtained, by subtracting the stage velocity from the position-time series, giving a recording of the probe's position relative to the sample cell. This data is then binned in terms of position (bin size is half a particle radius), giving the dwell time in each position range. The data from the 62% sample is compared to data at the same drag speed in a 56% sample. The jerky motion is readily apparent in the spread of data at the higher volume fraction; this representation also shows that the regions of stronger obstruction are seemingly random in distribution, and do not apparently occur in clusters.

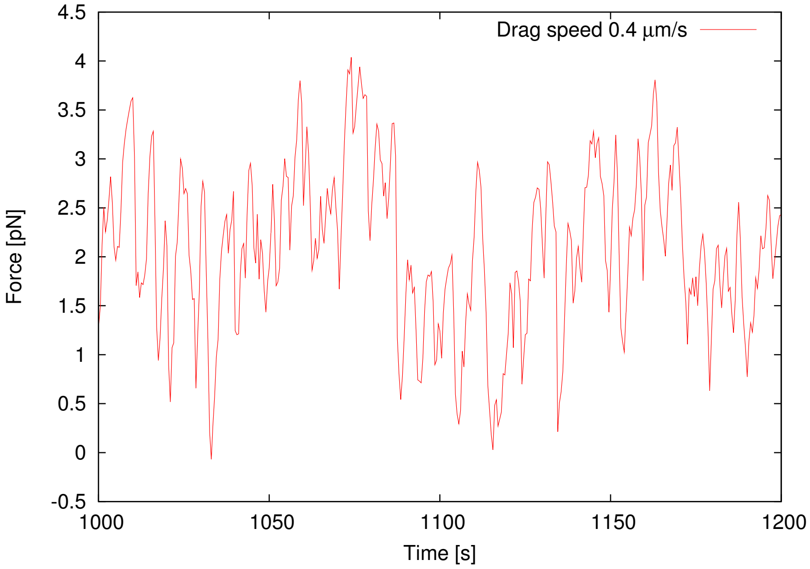

Figure 6.12: Time-force series for a dragging measurement in a $\phi = 62\%$ colloidal glass. The data have been down-sampled to 2Hz.

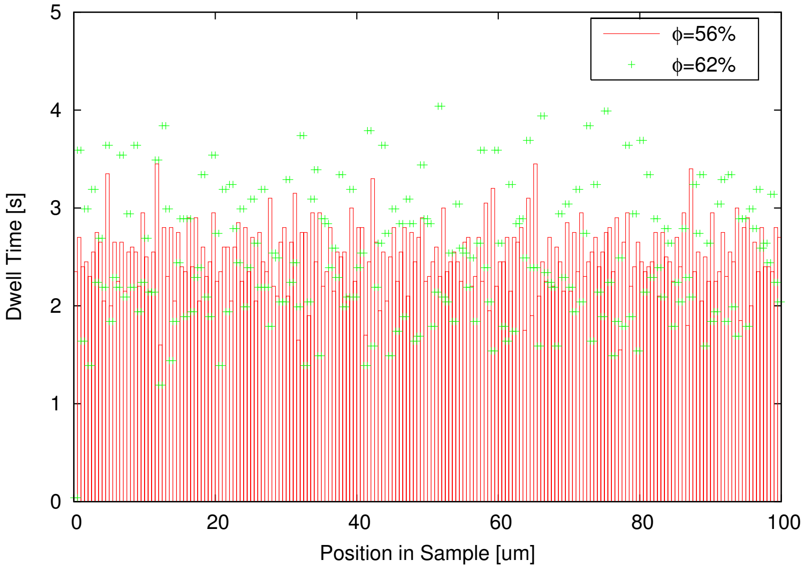

Figure 6.13: Position-time series for the lowest and highest volume fractions, at the same drag speed. The crosses mark out the corners of the histogram bar for the higher volume fraction. One histogram bin is equivalent to half a particle radius; although the average speed in both is the same, the scatter of data points is much larger in the case of the glassy sample. This is because the particle motion in the non-ergodic sample is impeded by successive, relatively stiff particle cages, which allow only erratic progress through the sample.

6.3 Size of Rearrangement events

This section is the final part of the analysis of dragging measurements on dense colloidal systems. On inspection of a typical force-time data series (for example, see figure 6.14), there appears to be a hierarchy of different sizes of cage rearrangement events; for example, two large rearrangements just after 1150 seconds, followed by two smaller ones. An enlarged subsection of this experiment showing the two smaller events is presented in figure 6.15; high-frequency Brownian noise is more significant at this timescale (the signal is generally noisier), but a hierarchy of events still seems apparent. At first glance, the two recordings look similar, hinting that there may be no single characteristic timescale upon which the system operates. This final results section examines the apparently scale-free behaviour in a quantitative fashion.

In order to count the number of events occurring on a particular timescale, a procedure based on wavelets [129] is used. Wavelet techniques can be thought of as an extension of Fourier transform methods, into the realm of transient signals. The Fourier transform has been used in this thesis to provide the spectral content of an entire signal (in this case particle position)[6]. The signal corresponding to a tracer breaking a cage of particles, however, is an inherently transient event, suggesting a time-varying frequency spectrum. The wavelet transform offers a wide choice of basis function, or 'wavelet', all of which are localised in time. The transformed function is expressed as a sum of wavelet functions with the same basic shape, but different amplitudes, temporal scaling factor (dilation) and time coordinates; the wavelet transform of a one-dimensional function is inherently a two-dimensional entity. Strictly speaking, a wavelet transform does not offer an entirely arbitrary choice of basis function[7], but for our purposes the conditions are relaxed slightly as we are not necessarily concerned with preserving the total information content of the signal. The routine I use here discards time and amplitude information, and is concerned solely with the number of peaks that occur on a particular timescale.

---

[6] The power spectrum of Brownian forces is constant at all frequencies, and does not change with time, which makes the Langevin equation ideal for solution by Fourier methods.

[7] See reference [129] for details.

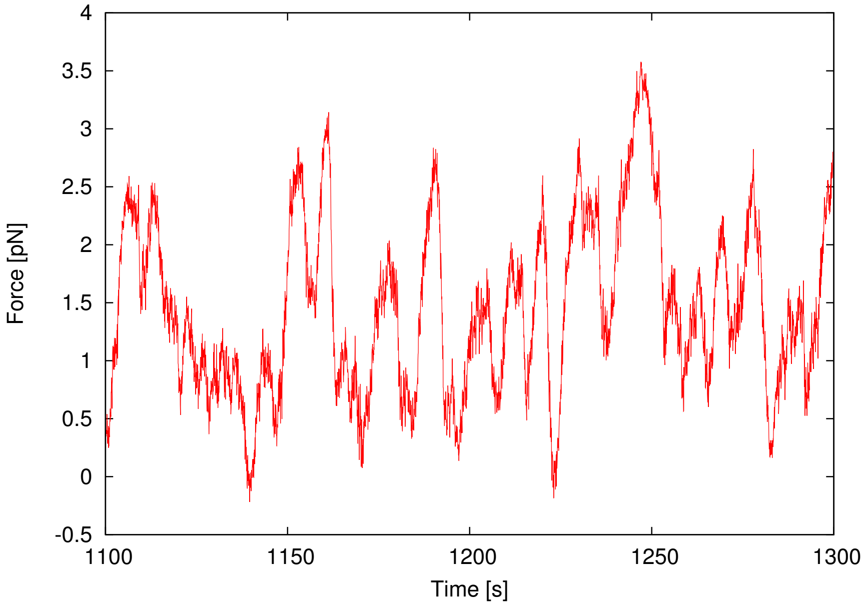

Figure 6.14: Time-force series for a dragging measurement at 0.2μm/s in a $\phi =$ 62% colloidal glass. The data have been down-sampled to 2Hz.

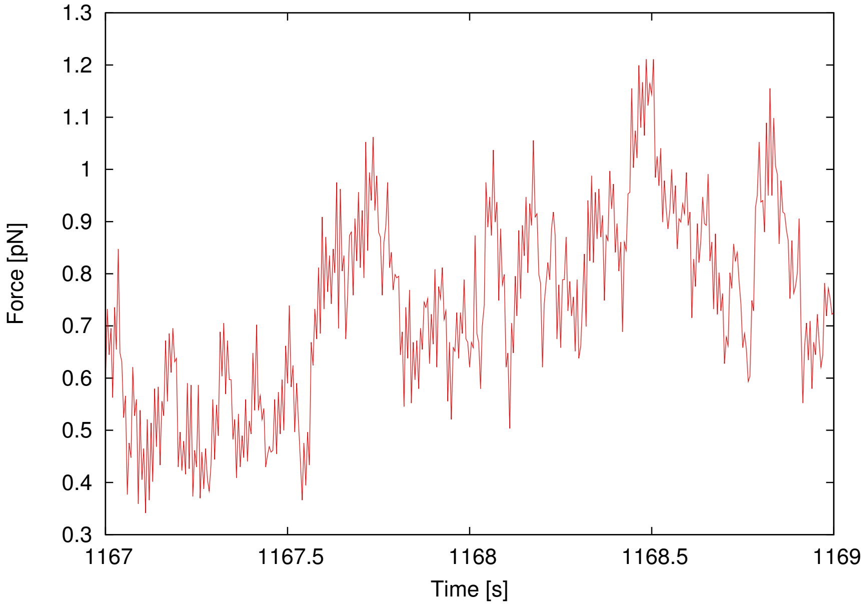

Figure 6.15: A two second subsection of the measurement in figure 6.14. The data have been down-sampled to 200Hz, so there is the same number of data points in both the longer and shorter graphs.

6.3.1 The peak extraction routine

The mathematical kernel of the peak extraction routine used[8] is based on the fitting of a quadratic function to the data, which is examined over a particular time window (or equivalently, at a particular dilation). The raw data is discretely sampled; in order to keep file sizes manageable, the original data is down-sampled, typically from 10kHz to around 5Hz. At these frequencies, the optical trap dominates the particle motion, and it is this that we are primarily interested in.

The fitting routine sifts through the data, looking at a particular time window (or equivalently, number of data points) to determine if there is a peak in that region. If the data at the start and end of a time window are lower than the data in the middle, the programme attempts to perform a quadratic fit procedure, with the amplitude, peak time and second derivative as fit parameters. If a peak is detected, the fit parameters are noted and the time window moves on. This process is illustrated in figure 6.16; clearly, the short time windows pick out more peaks, and the longer ones pick out fewer. The exact time location of the peak depends upon the window size, but this is relatively unimportant, as only the total number of peaks are considered for each window size.

The number of peaks detected is recorded for a range of window sizes, and at all drag speeds and volume fractions (except the highest, $\phi = 62\%$). Looking at figure 6.16, some peaks are clearly detected by all time windows (for example, the peak between 106 and 107 seconds). In order to correct for this, the number of peaks detected at a particular window size is subtracted from the number of peaks detected at the next *largest* window size. This leaves only the number of peaks specific to the window length in question, as smaller peaks that are not local maxima are not counted.

6.3.2 Peak size distribution

The data obtained using the fitting routine takes the form of a distribution of number of peaks as a function of window length. Such a distribution is presented in figure 6.17, where the distribution is normalised by the third data point[9].

---

[8] One of the built-in routines of National Instruments corp.'s Labview 7.1 development suite.

[9] This choice is somewhat arbitrary, but is chosen to highlight the trend in data at larger time windows.

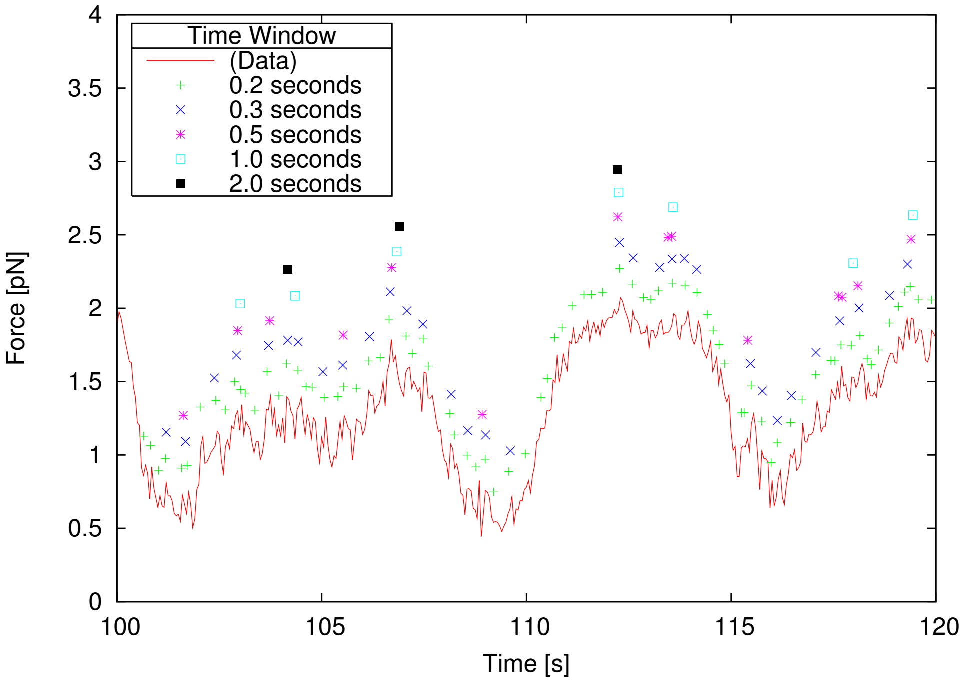

Figure 6.16: Example of peak detection routine, on a section of a measurement in $\phi = 58\%$, drag speed 0.4μm/s. The red line represents the original data, while the points are the peaks detected using different time windows. The peaks have been translated vertically for the sake of clarity.

At the shortest time windows (the first two data points), Brownian fluctuations start to interfere with the statistics by producing 'false' peaks, as the crossover between Brownian force-dominated motion and trap-dominated motion occurs at this timescale, around 5-10Hz. If too large a time window is used (greater than about 2 seconds), the signal becomes noisy, as there are insufficient events to establish a trend, and because there is a limit to the maximum event size (the probe is ultimately contained by the trap). Intermediate times seem to approximately follow a power-law behaviour,

$$N \propto \Delta t^{-\Upsilon} \tag{6.2}$$

where N is the number of events, Δt is the length of the time window, and Υ is a parameter. A fit is performed between 0.25 seconds and 1.5 seconds, to give a value for Υ, which varies between 1.4 and 2.6. This parameter is a way of characterising the size distribution of cage rearrangement events at a particular drag speed and a particular volume fraction. A larger value of Υ means that there are more events at a shorter time-scale.

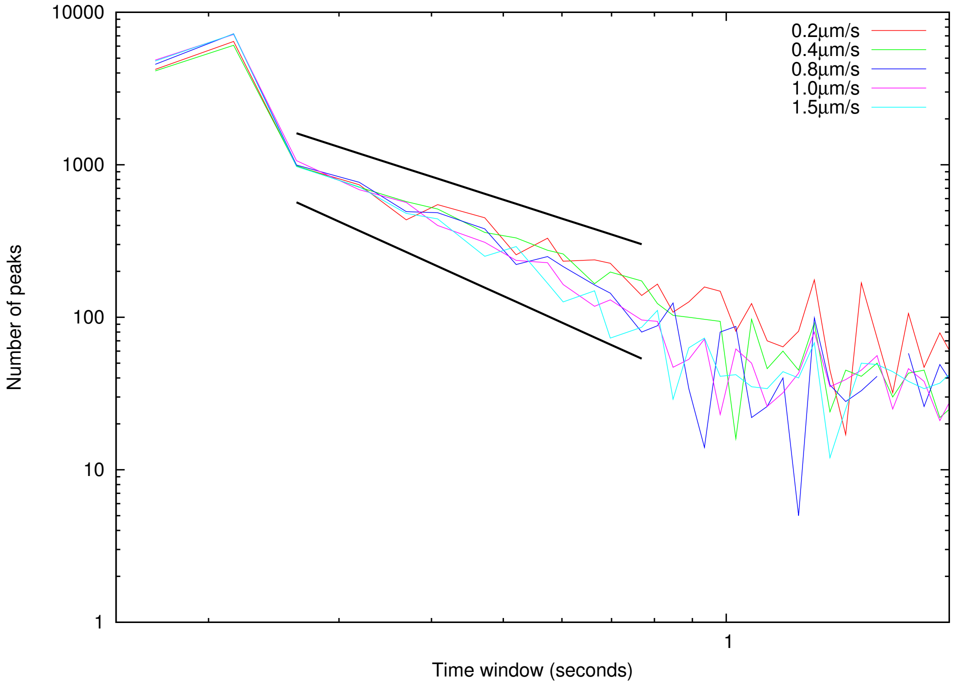

Figure 6.17: Size distribution of rearrangement events in a $\phi = 56\%$ colloidal suspension. The thick black lines show the highest and lowest values of Υ (1.56 and 2.14 respectively).

What is noticeable from looking at figure 6.17, is that Υ increases with drag speed. It might be suggested that the higher drag speeds give faster rearrangements simply because the probe is driven faster, but that would not necessarily affect the *shape* of the distribution; if this were true, the entire distribution in figure 6.17 would just be shifted to the left for faster speeds, as the particle is driven at a constant velocity. Lines fitted to the highest and lowest drag speed measurements (with exponents $\Upsilon = 2.14$ and 1.56 respectively) have been included, and offset from the data to provide a visual guide to the range of exponents.

6.3.3 Variation with ϕ and drag speed

Figure 6.18 shows a summary of this type of data for all volume fractions and all drag speeds. Broadly speaking, it would seem that the trend seen in figure

6.17 (Υ increases for greater dragging speeds) is present in all volume fractions $\phi < 58\%$, below 1.5μm/s drag speed. Qualitatively, this means that at higher drag speeds, the accumulated stresses relax in the form of many small rearrangements (cage breaking) events, as opposed to fewer large ones — the opposite is true at lower drag speeds. Although the total range of exponents is not great, this is still a systematic trend across all volume fractions. The data at 58% is less conclusive; this is perhaps not surprising, as there are many other factors, such as the mean force (figure 6.2) and standard deviation (figure 6.8) that show a qualitative change at the glass transition.

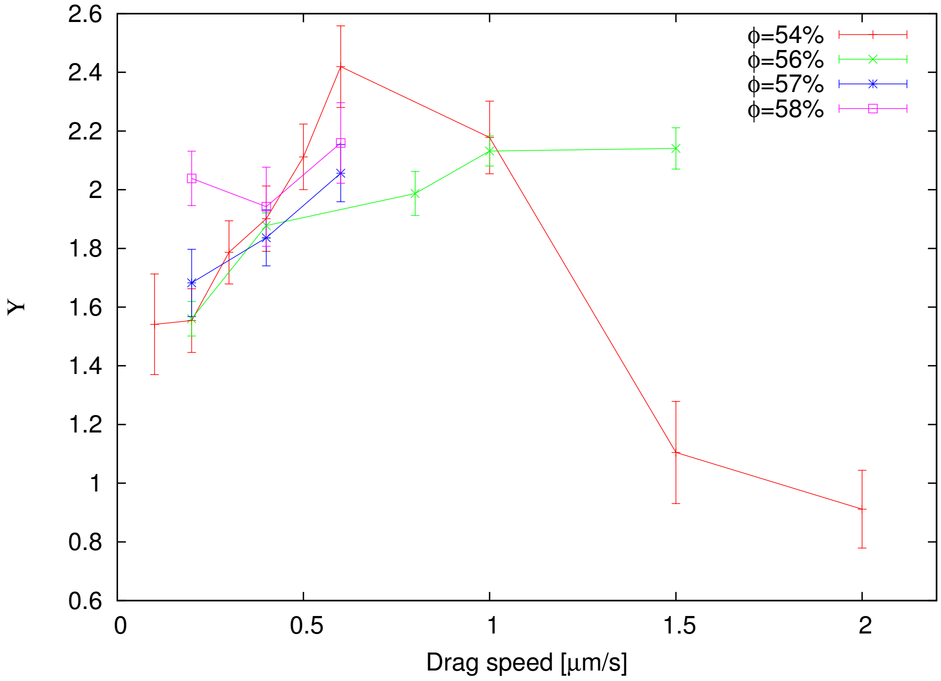

Figure 6.18: Variation of Υ with drag speed.

Chapter 7

Conclusion and Outlook

In this final chapter, I summarise the main findings of my experiments, and suggest some interesting possibilities for future work.

7.1 Optical characterisation

Usually, calibration data would not be included in a summary of results, but as I have remarked previously (in chapter 3) there appears to be little in the published literature that deals with large-displacement trap calibration. It was found that there are two distinct nonlinearities that are of importance for a well-calibrated experiment: non-linearity in position detection and anharmonicity in the optical force profile. The nonlinearity in the position detection causes an overestimation of particle displacement when judged by the QPD data alone, with an error of $\sim 100\%$ at a displacement of a particle radius. The trap profile anharmonicity leads to forces being overestimated by up to 33% at a displacement of one particle radius from the equilibrium position. Both of these details may be eliminated by making measurements using a CCD camera, applying a known force to a trapped particle by means of a fluid flow, and measuring the displacement by a basic image analysis. It was found that the deviations from the linear behaviour in both cases were well accounted for by a third-order correction, with no significant improvement in a fit to the data upon the addition of higher-order terms to the fitted equation.

7.2 Static measurements

In chapter 5 it was found that values for the short-time self-diffusion coefficient D_s^s in samples with volume fractions below the glass transition ϕ_g agree very well with values obtained from static light-scattering measurements, both in the average value and the spread of values obtained. The spread in values is attributed to local inhomogeneities inherent in the samples. In samples with volume fractions at and above $\phi_g \approx 58\%$, the measured value of D_s^s depends strongly on the sample's local history. In the $\phi = 58\%$ sample, local perturbations caused by moving the probe particle around in the sample are slow to relax, taking between 15 minutes and an hour to return to their nominal 'equilibrium' value. This effect is more profound for $\phi = 62\%$, where the relaxations take much longer to relax - an upper bound on the relaxation time of 16 hours is found.

The high sampling rate afforded by this optical-tweezers technique is exploited in the second half of chapter 5. By examining time-resolved data, it has been shown that the cage structures observed by confocal microscopy are in fact the sum of several 'microcages', due to fluctuations in cage shape and position, wherein the particle has sufficient time to diffusively explore each microcage. At the higher volume fractions, an effective 'yield force' is hinted at, as optical forces of up to 0.66pN are applied to a particle for up to 50 minutes, and only a very slight relaxation is observed.

7.3 Dynamic measurements

In the active (dragging) measurements, the difference between sub-glassy samples and glassy samples once again becomes clear. At volume fractions in the range $\phi = 54\% \rightarrow 57\%$ the behaviour is essentially fluid, with no yield stress observed. It was possible to extract values for an 'effective viscosity' based on a Stokes-type model. These effective viscosities are found to be around a factor of two higher than those measured in the static measurements; it was suggested that the introduction of an 'effective radius' for the particle, based on geometrical considerations, may go some way towards accounting for this discrepancy.

At a volume fraction of $\phi = 58\%$, the behaviour of a dragged particle is dominated by the yielding force of the sample. The displacement histograms at different speeds have a similar average displacement and spread of data. This follows a trend observed by Petekidis and co-workers [54], where a yield stress emerges upon reaching the glass transition. Although my values for the yield stress are not in good agreement with the bulk rheology data, this is unsurprising in many ways, as the shearing measurement is highly localised, in an otherwise unperturbed medium. The highest volume fraction studied, $\phi = 62\%$ shows the largest spread of data; at this volume fraction, a greater trap stiffness must be used (about 60% stronger than previous measurements). The results for yielding forces in both $\phi = 58\%$ and $\phi = 62\%$ are in good agreement with a directly comparable microrheological study by Habdas et al. [114].

Finally, the distribution of sizes in force build-up and relaxation events is examined. It was found that at dragging speeds up to 1μm/s, the distribution of event sizes is biased in favour of the smaller events, with larger events being rarer. This bias increases with drag speed, and occurs at all drag speeds, and in all volume fractions up to and including $\phi_g = 58\%$, where data is available.

7.4 Future work

This thesis is a first investigation of optical tweezers based microrheology of dense hard-sphere suspensions; there are many unanswered questions that result from it. Although a wealth of experimental data is available, a theoretical model of the microrheology is still under development. Squires et al. [123] have developed a mathematical description of the microrheology of very dilute suspensions of particles with a hard-sphere radius much larger than the hydrodynamic radius, allowing hydrodynamic interactions to be neglected. The model describes the formation of a dense boundary layer in front of the dragged particle — a phenomenon which is appealing when explaining the results of my dragging experiments. Incorporating confocal imaging into the optical tweezers setup would be able to lend experimental support to this idea, and also give empirical evidence to aid the extension of the theoretical work to denser samples.

Initial examination of the dragging data prompted the suggestion that the particle was moving forward in a series of discrete steps, remaining in one location until it had built up sufficient force to break through the neighbouring particles, and then catch up with the optical trap; the colloidal host acts as a solid barrier – a 'brick wall' – impeding particle progress. Data to support this description is seen in the constant force experiments of Weeks et al. [114], where the probe's position in the sample is constant for hundreds of seconds at a time, before the probe particle suddenly moves onward. However, there are two respects in which that situation is subtly different to the one here. Firstly, my optical tweezers experiments are *not* constant-force experiments, indeed both the force driving the probe and the probe velocity vary. Secondly, the structures blocking the probe's progress are not the static, hard barriers implied by the 'brick wall' description; instead, they are elastic objects, which deform and then finally yield. A careful investigation of the data showing the probe's position relative to the sample (from which figure 6.13 is derived), preferably in conjunction with confocal imaging, would give a valuable insight into the nature and elastic response of the relevant colloidal micro-structures.

An extension of the experimental setup to include a second optical trap would give valuable information regarding the interaction between two neighbouring particles. The idea of 'microcages', introduced in chapter 5, could be used to extend the work of Weeks et al. [97], which describes the collective rearrangements that are necessary for relaxations in dense suspensions. The correlation of particle motion between two particles at various separation distances would give insight not only into the frequency and size of these events, but also (by altering the probe particle separation) into the spatial extent. Here, the optical tweezers technique comes into its own, as it has a fifty-fold increase in spatial resolution, and a thousand-fold increase in time resolution over confocal studies.

A two trap setup would also provide useful information on drag measurements; by dragging one particle and holding a second still, the effect on the micro-sheared host could be measured, for example in terms of a decreased short-time self-diffusion coefficient that comes with an increase in local density. Similarly, by dragging two particles at once (either side-by side or along the same path), the response of a perturbed region to further action could be probed. This has particular relevance to the work by Meyer et al. [8] which describes microrheological measurements at high shear rates in suspensions where the probe is much larger than the host, which acts as a continuous medium. The trapped particle in this case collects a boundary layer of high particle density close to its surface, and this layer is sheared off to line the probe's wake. The interaction of two dense boundary layers could prove interesting, as two adjacent probes being dragged side-by-side are brought together; also, the forces acting on a probe travelling at the same speed, but a distance behind another would give information about the relaxation of the local suspension, and how it varies throughout a sample.

Appendix A

Timeline for experimental work

The prototype force measurement setup was built before I began my PhD work, in October 2003. After some preliminary measurements using a Helium-Neon laser conducted initially by Dr. Arlt, and then by myself, the apparatus was dismantled and moved into a new laboratory space in January of 2004. The experiment was reconstructed both by myself and Dr. Arlt, and the laborious process of alignment was also shared between us. The next 18 months were spent characterising and optimising parts of the optical system, as well as improving experimental protocol. Once the system had been upgraded (to incorporate new passive vibration-damping components) and the stock colloidal samples prepared, I undertook a final full realignment in September 2005 when the location of the pick-off power meter was changed to that shown in chapter 3. This configuration was used for all of the experimental work herein, with minimal modification to ensure that the optical trap is in the centre of the imaging camera's field of view.

The calibration of the detection system, including the correction of non-linearities (see chapter 3) was performed in the Autumn of 2005, allowing measurement of average particle position at nanometre resolution, and forces as small as 90fN. This information allowed the collection of the data which makes up the main body of this thesis. With the exception of the results from the $\phi = 40\%$ suspension (which were obtained in 2005), all of the experimental work included in this thesis was performed between April and August of 2006, following the departure of Dr. Arlt in March of that year. The analysis work was performed by myself between September 2006 and March 2007.

Computer programmes for raw data acquisition were written by Dr. Arlt in 2003, along with those for the analysis of power spectrum data (see chapter 3); I modified the power spectrum programmes in 2006 to allow multiple files to be processed at the same time. The programmes for the linearization of position and force data were written exclusively by myself in late 2006. The programmes for results analysis (such as the production of 2D histograms and the production of peak-size distributions) were written by myself, with support from programme libraries included with National Instruments corp.'s Labview v7.1 development suite.

Bibliography

[1] A Ashkin, J M Dziedzic, J E Bjorkholm, and S Chu. Observation of a single-beam gradient force optical trap for dielectric particles. *Opt. Lett.*, 11(5):288, 1986.

[2] M G Roca, J Arlt, C E Jeffree, and N D Read. Cell biology of conidial anastomosis tubes in *neurospora crassa*. *Eukaryotic Cell*, 4:911–9, 2005.

[3] H Misawa, K Sasaki, M Koshioka, and N Kitamura. Multibeam laser manipulation and fixation of microparticles. *Appl. Phys. Lett.*, 60:310–12, 1992.

[4] E R Dufresne and D G Grier. Optical tweezer arrays and optical substrates created with diffractive optics. *Rev. Sci. Instrum.*, 69:1974–7, 1998.

[5] W J Hossack, E Theofanidou, J Crain, K Heggarty, and M Birch. High-speed holographic optical tweezers using a ferroelectric liquid crystal microdisplay. *Opt. Express*, 11:2053–9, 2003.

[6] A Lafong, W J Hossack, J Arlt, T J Nowakowski, and N D Read. Time-multiplexed laguerre-gaussian holographic optical tweezers for biological applications. *Opt. Express*, 14:3065–72, 2006.

[7] S Henderson, S Mitchell, and P Bartlett. Position correlation microscopy: probing single particle dynamics in colloidal suspensions. *Colloids Surf., A*, 190:81–8, 2001.

[8] A Meyer, A Marshall, B G Bush, and E M Furst. Laser tweezer microrheology of a colloidal suspension. *J. Rheol.*, 50:77–92, 2006.

[9] G D Wright, J Arlt, W C K Poon, and N D Read. Experimentally manipulating fungi with optical tweezers. *Mycoscience*, 48:15–19, 2007.

[10] P J H Bronkhorst, G J Streekstra, J Grimbergen, E J Nijhof, J J Sixma, and G J Brakenhoff. A new method to study shape recovery of red blood cells using multiple optical trapping. *Biophys. J.*, 69:1666–73, 1995.

[11] S M Block, D F Blair, and H C Berg. Compliance of bacterial flagella measured with optical tweezers. *Nature*, 338:514–8, 1989.

[12] F Gittes and C F Schmidt. Interference model for back-focal-plane displacement detection in optical tweezers. *Opt. Lett.*, 23(1):7–9, 1998.

[13] A Pralle, M Prummer, E-L Florin, E H K Stelzer, and J K H Hörber. Three-dimensional high-resolution particle tracking for optical tweezers by forward scattered light. *Microsc. Res. Tech.*, 44:378–86, 1999.

[14] E A Abbondanzieri, W J Greenleaf, J W Shaevitz, R Landick, and S M Block. Direct observation of base-pair stepping by rna polymerase. *Nature*, 438:460–5, 2005.

[15] F Gittes and C F Schmidt. Signals and noise in micromechanical measurements. In Michael P. Sheetz, editor, *Methods In Cell Biology*, volume 55, chapter 8. Academic Press, 1998.

[16] K Berg-Sørensen and H Flyvbjerg. Power spectrum analysis for optical tweezers. *Rev. Sci. Instrum.*, 75(3), 2002.

[17] D H Everett. *Basic Principles of Colloid Science*. Royal Society of Chemistry, 1988.

[18] J B Perrin. Nobel lecture, December 11th, 1926.

[19] W Poon, P Pusey, and H Lekkerkerker. Colloids in suspense. *Phys. World*, page 27, April 1996.

[20] K. N. Pham, A. M. Puertas, J. Bergenholtz, S. U. Egelhaaf, A. Moussaïd, P. N. Pusey, A. B. Schofield, M. E. Cates, M. Fuchs, and W. C. K. Poon. Multiple glassy states in a simple model system. *Science*, 296:104, 2002.

[21] A Ashkin, J M Dziedzic, and T Yamane. Optical trapping and manipulation of single cells using infrared laser beams. *Nature*, 330:769–71, 1987.

[22] J C Crocker and D G Grier. Microscopic measurement of the pair interaction potential of charge-stabilized colloid. *Phys. Rev. Lett.*, 73:352–5, 1994.

[23] P N Pusey. Colloidal suspensions. In J. P. Hansen, D. Levesque, and J. Zinn-Justin, editors, *Liquides, Cristallisation et Transition Vitreuse/Liquids, Freezing and Glass Transition*, pages 763–942. Elsevier Science Publishers B. V., 1991.

[24] J C Crocker and D G Grier. When like charges attract: The effects of geometrical confinement on long-range colloidal interactions. *Phys. Rev. Lett.*, 73:1897–1900, 1996.

[25] J C Crocker. Measurement of the hydrodynamic corrections to the brownian motion of two colloidal spheres. *J. Chem. Phys.*, 106:2837–40, 1997.

[26] W B Russel, D A Saville, and W R Schowalter. *Colloidal Dispersions*. Cambridge University Press, 1989.

[27] L P Faucheux, L S Bourdieu, P D Kaplan, and A J Libchaber. Optical thermal ratchet. *Phys. Rev. Lett.*, 74:1504–7, 1995.

[28] D M Carberry, J C Reid, G M Wang, E M Sevick, D J Searles, , and D J Evans. Fluctuations and irreversibility: An experimental demonstration of a second-law-like theorem using a colloidal particle held in an optical trap. *Phys. Rev. Lett.*, 92:140601, 2004.

[29] A D Dinsmore, A G Yodh, and D J Pine. Entropic control of particle motion using passive surface microstructures. *Nature*, 383:239–42, 1996.

[30] J P Hoogenboom, D L J Vossen, C Faivre-Moskalenko, M Dogterom, and A van Blaaderen. Patterning surfaces with colloidal particles using optical tweezers. *Appl. Phys. Lett.*, 80:4828–30, 2002.

[31] K Sasaki, M Koshioka, H Misawa, N Kitamura, and H Masahura. Optical trapping of a metal particle and a water droplet by a scanning laser beam. *Appl. Phys. Lett*, 60:807, 1992.

[32] P H Jones, E Stride, and N Saffari. Trapping and manipulation of microscopic bubbles with a scanning optical tweezer. *Appl. Phys. Lett.*, 89:081113, 2006.

[33] P A Prentice, M P MacDonald, T G Frank, A Cuschieri, G C Spalding, W Sibbett, P A Campbell, and K Dholakia. Manipulation and filtration of low-index particles with holographic laguerre-gaussian optical trap arrays. *Opt. Express*, 12:593–600, 2004.

[34] H He, M E J Friese, N R Heckenberg, and H Rubinsztein-Dunlop. Direct observation of transfer of angular momentum to absorptive particles from a laser beam with a phase singularity. *Phys. Rev. Lett.*, 75:826–9, 1995.

[35] J E Molloy and M J Padgett. Lights, action: optical tweezers. *Contemp. Phys.*, 43(4):241, 2002.

[36] V Garcés-Chávez, D McGloin, H Melville, W Sibbett, and K Dholakia. Simulataneous micromanipulation in multiple planes using a self-reconstructing light beam. *Nature*, 419:145–7, 2002.

[37] E R Dufresne, G C Spalding, M T Dearing, S A Sheets, and D G Grier. Computer-generated holographic optical tweezer arrays. *Rev. Sci. Instrum.*, 72:1810–6, 2001.

[38] M P MacDonald, G C Spalding, and K. Dholakia. Creation and manipulation of three-dimensional optically trapped structures. *Science*, 426:421–4, 2003.

[39] F Gittes, B Schnurr, P D Olmsted, F C MacKintosh, and C F Schmidt. Microscopic viscoelasticity: Shear moduli of soft materials determined from thermal fluctuations. *Phys. Rev. Lett.*, 79(17):3286, 1997.

[40] L. Starrs and P. Bartlett. One- and two-point micro-rheology of viscoelastic media. *J. Phys. Condens. Matter*, 15:S251, 2003.

[41] D Mizuno, C Tardin, C F Schmidt, and F C MacKintosh. Nonequilibrium mechanics of active cytoskeletal networks. *Science*, 315:370, 2007.

[42] M Atakhorrami, J I Sulkowska, K M Addas, G H Koenderink, J X Tang, A J Levine, F C MacKintosh, and C F Schmidt. Correlated fluctuations of microparticles in viscoelastic solutions: Quantitative measurement of material properties by microrheology in the presence of optical traps. *Phys. Rev. E*, 73:061501, 2006.

[43] P L Biancaniello and J C Crocker. Line optical tweezers instrument for measuring nanoscale interactions and kinetics. *Rev. Sci. Instrum.*, 77:113702, 2006.

[44] M Atakhorrami and C F Schmidt. High-bandwidth one- and two-particle microrheology in solutions of wormlike micelles. *Rheol. Acta*, 45:449–56, 2006.

[45] T A Waigh. Microrheology of complex fluids. *Rep. Prog. Phys.*, 68:685–742, 2005.

[46] J-C Meiners and S R Quake. Direct measurement of hydrodynamic cross correlations between two particles in an external potential. *Phys. Rev. Lett.*, 82:2211–4, 1999.

[47] Stuart Henderson, Steven Mitchell, and Paul Bartlett. Propagation of hydrodynamic interactions in colloidal suspensions. *Phys. Rev. Lett.*, 88(8):088302, 2002.

[48] N Greinert, T Wood, and P Bartlett. Measurement of effective temperatures in an aging colloidal glass. *Phys. Rev. Lett.*, 97:265702, 2006.

[49] S Jabbari-Farouji, D Mizuno, M Atakhorrami, F C MacKintosh, C F Schmidt, E Eiser, G H wegdam, and D Bonn. Fluctuation-dissipation theorem in an aging colloidal glass. *Phys. Rev. Lett.*, 98:108302, 2007.

[50] M Yada, J Yamamoto, and H Yokoyama. Direct observation of anisotropic interparticle forces in nematic colloids with optical tweezers. *Phys. Rev. Lett.*, 92:185501, 2004.

[51] I I Smalyukh, A N Kuzmin, A V Kachynski, P N Prasad, and O D Lavrentovich. Optical trapping of colloidal particles and measurement of the defect line tension and colloidal forces in a thermotropic nematic liquid crystal. *Appl. Phys. Lett.*, 86:021913, 2005.

[52] M D Haw. Jamming, two-fluid behaviour, and “self-filtration” in concentrated particulate suspensions. *Phys. Rev. Lett*, 92:185506, 2004.

[53] W van Megen, T C Mortensen, S R Williams, and J Müller. Measurement of the self-intermediate scattering function of suspensions of hard spherical particles near the glass transition. *Phys. Rev. E*, 58:6073–85, 1998.

[54] G Petekidis, D Vlassopoulos, and P N Pusey. Yielding and flow of colloidal glasses. *Faraday Discuss.*, 123:287–302, 2003.

[55] T Tlusty, A Meller, and R Bar-Ziv. Optical gradient forces of strongly localized fields. *Phys. Rev. Lett.*, 81(8):1738–41, 1998.

[56] S Chu. Plenary Talk, Optical Trapping and Micromanipulation III, SPIE Optics and Photonics 2006, San Diego, US, 2006.

[57] A Ashkin. Acceleration and trapping of particles by radiation pressure. *Phys. Rev. Lett.*, 24:156–9, 1970.

[58] A Ashkin and J M Dziedzic. Optical levitation of liquid drops by radiation pressure. *Science*, 187:1073–5, 1975.

[59] A Ashkin. Forces of a single beam gradient laser trap on a dielectric sphere in the ray optics approximation. *Biophys. J.*, 61:569–82, 1992.

[60] K Svoboda and S M Block. Power spectrum analysis for optical tweezers. *Annu. Rev. Biophys. Biomol. Struct.*, 23:247–85, 1994.

[61] J D Jackson. *Classical Electrodynamics (2nd Ed.).* John Wiley and Sons Inc., 1975.

[62] A Mazolli, P A Maia Neto, and H M Nussenveig. Theory of trapping forces in optical tweezers. *Proc. R. Soc. Lond. A*, 459:3021–41, 2003.

[63] L D Landau and E M Lifshitz. *Electrodynamics of Continuous Media.* Pergamon Press, 1960.

[64] P Bartlett and S Henderson. Three-dimensional force calibration of a single-beam optical gradient trap. *J. Phys. Condens. Matter*, 14:7757, 2002.

[65] P N Pusey and W van Megen. Observation of a glass transition in suspensions of spherical colloidal particles. *Phys. Rev. Lett.*, 59:2083, 1987.

[66] F Reif. *Fundamentals of Statistical and Thermal Physics.* McGraw-Hill, 1965.

[67] L P Ghislain, N A Switz, and W W Webb. Measurement of small forces using an optical trap. *Rev. Sci. Instrum.*, 65:2762–68, 1994.

[68] S F Tolić-Nørrelykke, E Schäffer, J Howard, F S Pavone, F Jülicher, and H Flyvbjerg. Calibration of optical tweezers with positional detection in the back focal plane. *Rev. Sci. Instrum.*, 77:103101, 2006.

[69] M Atakhorrami, G H Koenderink, C F Schmidt, and F C MacKintosh. Short-time inertial response of viscoelastic fluids: Observation of vortex propagation. *Phys. Rev. Lett.*, 95:208302, 2005.

[70] E Fällman and O Axner. Design for fully steerable dual-trap optical tweezers. *Appl. Opt.*, 36(10):2107, 1997.

[71] N Malagnino, G Pesce, A Sasso, and E Arimondo. Measurements of trapping efficiency and stiffness in optical tweezers. *Opt. Comm.*, 214:15, 2002.

[72] W H Wright, G J Sonek, and M W Berns. Parametric study of the forces on microspheres held by optical tweezers. *Appl. Opt.*, 33(9):1735, 1999.

[73] P C Ke and M Gu. Characterization of trapping force in the presence of spherical aberration. *J. Mod. Opt.*, 45(10):2159, 1998.

[74] E Theofanidou, L Wilson, W J Hossack, and J Arlt. Spherical aberration correction for optical tweezers. *Opt. Comm.*, 236:145–50, 2004.

[75] A Rohrbach and E H K Stelzer. Three-dimensional position detection of optically trapped dielectric particles. *J. Appl. Phys.*, 91(8):5474, 2002.

[76] E J G Peterman, M A van Dijk, L Kapitein, and C F Schmidt. Extending the bandwidth of optical-tweezers interferometry. *Rev. Sci. Instrum.*, 74:3246–9, 2003.

[77] B Lukić, S Jeney, C Tischer, A J Kulik, L Forró, and E-L Florin. Direct observation of nondiffusive motion of a brownian particle. *Phys. Rev. Lett.*, 95:160601, 2005.

[78] S Sato and H Inaba. Optical trapping and manipulation of microscopic particles and biological cells by laser beams. *Opt. Quant. Electron.*, 28:1–16, 1996.

[79] Y Liu, D K Cheng, G J Sonek, M W Berns, C F Chapman, and B J Tromberg. Evidence for localized cell heating by infrared optical tweezers. *Biophys. J.*, 68:2137–44, 1995.

[80] Erwin J. G. Peterman, Frederick Gittes, and Christoph F. Schmidt. Laser-induced heating in optical traps. *Biophys. J.*, 84:1308, 2003.

[81] M Born and E Wolf. *Principles of Optics, 7th Ed.* Cambridge University Press, 2005.

[82] J H G Huisstede, K O van der Werf, M L Bennink, and V Subramaniam. Force detection in optical tweezers using backscattered light. *Opt. Express*, 13:1113–23, 2005.

[83] W J Greenleaf, M T Woodside, E A Abbondanzieri, and S M Block. Passive all-optical force clamp for high-resolution laser trapping. *Phys. Rev. Lett.*, 95:208102, 2005.

[84] A Buosciolo, G Pesce, and A Sasso. New calibration method for position detector for simultaneous measurements of force constants and local viscosity in optical tweezers. *Opt. Comm.*, 230:357, 2004.

[85] V Martelozzo. *Crystallisation and Phase Separation in Colloidal Systems.* PhD Thesis - Edinburgh University, 2001.

[86] P N Pusey and W van Megen. Properties of concentrated suspensions of slightly soft colloidal spheres. In Samuel A. Safran and Noel A. Clark, editors, *Physics of Complex and Supermolecular Fluids*, pages 673–98. Wiley-Interscience, 1987.

[87] D J Fairhurst. *Polydispersity in Colloidal Phase Transitions.* PhD Thesis - Edinburgh University, 1999.

[88] E R Weeks, J C Crocker, A C Levitt, A B Schofield, and D A Weitz. Three-dimensional direct imaging of structural relaxation near the colloidal glass transition. *Science*, 287:627, 2000.

[89] A van Blaaderen and P Wiltzius. Real-space structure of colloidal hard-sphere glasses. *Science*, 270:1177–9, 1990.

[90] A D Dinsmore, E R Weeks, V Prasad, A C Levitt, and D A Weitz. Three-dimensional confocal microscopy of colloids. *Appl. Opt.*, 40(24):4152, 2001.

[91] Anand Yethiraj and Alfons van Blaaderen. A colloidal model system with an interaction tunable from hard sphere to soft and dipolar. *Nature*, 421:513, 2003.

[92] W G Hoover and F H Ree. Melting transition and communal entropy for hard spheres. *J. Chem. Phys*, 49(8):3609–3617, 1968.

[93] B Doliwa and A Heuer. Cage effect, local anisotropies, and dynamic heterogeneities at the glass transition: A computer study of hard spheres. *Phys. Rev. Lett.*, 80:4915–8, 1998.

[94] P Allegrini, J F Douglas, and S C Glotzer. Dynamic entropy as a measure of caging and persistent particle motion in supercooled liquids. *Phys. Rev. E*, 60:5714–24, 1999.

[95] P N Pusey and W van Megen. Phase behaviour of concentrated suspensions of nearly hard colloidal spheres. *Nature*, 320:340–2, 1986.

[96] W van Megen and S M Underwood. Glass transition in colloidal hard spheres: Measurement and mode-coupling-theory analysis of the coherent intermediate scattering function. *Phys. Rev. E*, 49:4206–20, 1994.

[97] E R Weeks and D A Weitz. Properties of cage rearrangements observed near the colloidal glass transition. *Phys. Rev. Lett.*, 89:095704, 2002.

[98] M D Ediger, C A Angell, and S R Nagel. Supercooled liquids and glasses. *J. Phys. Chem.*, 100:13200–12, 1996.

[99] W van Megen and S M Underwood. Glass transition in colloidal hard spheres: Mode-coupling theory analysis. *Phys. Rev. Lett.*, 70:2766–69, 1993.

[100] R E Courtland and E R Weeks. Direct visualization of ageing in colloidal glasses. *J. Phys. Condens. Matter*, 15:S359–65, 2003.

[101] D Bonn, S Tanase, B Abou, H Tanaka, and J Meunier. Laponite: Aging and shear rejuvenation of a colloidal glass. *Phys. Rev. Lett.*, 89:015701, 2002.

[102] M J Stevens, M O Robbins, and J F Belak. Shear melting of colloids: A non-equilibrium phase diagram. *Phys. Rev. Lett.*, 66:3004–7, 1991.

[103] J C van der Werff, C G de Kruif, C Blom, and J Mellema. Linear viscoelastic behaviour of dense hard-sphere dispersions. *Phys. Rev. A*, 39:795–807, 1989.

[104] T G Mason and D A Weitz. Linear viscoelasticity of colloidal hard sphere suspensions near the glass transition. *Phys. Rev. Lett.*, 74(14):2770–3, 1995.

[105] H Watanabe, M-L Yao, K Osaki, T Shitata, H Niwa, Y Morishima, N P Balsara, and H Wang. Nonlinear rheology and flow-induced structure in a concentrated spherical silica suspension. *Rheol. Acta*, 37:1–6, 1998.

[106] J F Brady. Model hard-sphere dispersions: statistical mechanical theory, simulations, and experiments. *Curr. Opin. Colloid Interface Sci.*, 1:472–80, 1996.

[107] B J Maranzano and N J Wagner. The effects of particle size on reversible shear thickening of concentrated colloidal dispersions. *J. Chem. Phys.*, 114:10514–27, 2001.

[108] C B Holmes, M Fuchs, and M E Cates. Jamming transitions in a schematic model of suspension rheology. *Europhys. Lett.*, 63:240–6, 2003.

[109] G. Petekidis, D Vlassopolous, and P. N. Pusey. Yielding and flow of sheared colloidal glasses. *J. Phys.: Condens. Matter*, 16:S3955, 2004.

[110] H Watanabe, M-L Yao, A Yamagishi, K Osaki, T Shitata, H Niwa, and Y Morishima. Nonlinear rheological behaviour of a concentrated spherical silica suspension. *Rheol. Acta*, 35:433–45, 1996.

[111] J F Brady. The rheological behaviour of concentrated colloidal dispersions. *J. Chem. Phys.*, 99:567–581, 1993.

[112] M Fuchs and M E Cates. Theory of nonlinear rheology and yielding of dense colloidal suspensions. *Phys. Rev. Lett.*, 89:28304, 2002.

[113] M. D. Haw, W. C. K. Poon, P. N. Pusey, P. Hebraud, and F. Lequeux. Colloidal glassas under shear strain. *Phys. Rev. E*, 58(4):4673, 1998.

[114] P Habdas, D Schaar, A C Levitt, and E R Weeks. Forced motion of a probe particle near the colloidal glass transition. *Europhys. Lett.*, 67(3):477, 2004.

[115] I C Carpen and J F Brady. Microrheology of colloidal dispersions by brownian dynamics simulations. *J. Rheol.*, 49:1483–502, 2005.

[116] Microparticles GmbH Harald Fiedler. private communication, 2005.

[117] W van Megen. Random-walk analysis of displacement statistics of particles in concentrated suspensions of hard spheres. *Phys. Rev. E*, 73:011401, 2006.

[118] P N Pusey and W van Megen. Observation of a glass transition in suspensions of spherical colloidal particles. *Phys. Rev. Lett.*, 59:2083–6, 1987.

[119] E Fällman, S Schedin, J Jass, M Andersson, B E Uhlin, and O Axner. Optical tweezers based force measurement system for quantitating binding interactions: system design and application for the study of bacterial adhesion. *Biosens. Bioelectron.*, 19:1429–37, 2004.

[120] W van Megen. private communication, 2007.

[121] E R Weeks and D A Weitz. Subdiffusion and the cage effect studied near the colloidal glass transition. *Chem. Phys.*, 284:361, 2002.

[122] V Prasad, D Semwogerere, and E R Weeks. Confocal microscopy of colloids. *J. Phys.: Condens. Matter*, 19:113102, 2007.

[123] T M Squires and J F Brady. A simple paradigm for active and nonlinear microrheology. *Phys. Fluids*, 17:073101, 2005.

[124] E Weeks. private communication, 2005.

[125] C Reichhardt and C J Olsen Reichhardt. Crossover from intermittent to continuum dynamics for locally driven colloids. *Phys. Rev. Lett.*, 96:028301, 2006.

[126] H J S Feder and J Feder. Self-organized criticality in a stick-slip process. *Phys. Rev. Lett.*, 66:2669–72, 1991.

[127] W H Press, S A Teukolsky, W T Vetterling, and B P Flannery. *Numerical recipes in C.* Cambridge University Press, 1992.

[128] K S Schweizer and E J Saltzman. Entropic barriers, activated hopping and the glass transition in colloidal suspensions. *J. Chem. Phys.*, 119:1181, 2003.

[129] R L Allen and D W Mills. *Signal Analysis: Time, Frequency, Scale, and Structure.* John Wiley & Sons, Inc., 2004.